Dynamics of Hybrid-Actuated Soft Robots with Stiffness Adaptation for Robot-Assisted Interventions

Majid Roshanfar

A Thesis

in

The Department

of

Mechanical, Industrial, and Aerospace Engineering

Presented in Partial Fulfillment of the Requirements

for the Degree of

Doctor of Philosophy (Mechanical Engineering) at

Concordia University

Montréal, Québec, Canada

August 2023

CONCORDIA UNIVERSITY

School of Graduate Studies

This is to certify that the thesis prepared

By: **Majid Roshanfar**

Entitled: **Dynamics of Hybrid-Actuated Soft Robots with Stiffness Adaptation for Robot-Assisted Interventions**

and submitted in partial fulfillment of the requirements for the degree of

Doctor of Philosophy (Mechanical Engineering)

complies with the regulations of this University and meets the accepted standards with respect to originality and quality. Signed by the Final Examining Committee:

_____ Chair
Dr. Carol Fung

_____ External Examiner
Dr. Sheila Russo

_____ Examiner
Dr. Mojtaba Kahrizi

_____ Examiner
Dr. Sivakumar Narayanswamy

_____ Examiner
Dr. Mojtaba Kheiri

_____ Supervisor
Dr. Javad Dargahi

Approved by _____
Dr. Martin Pugh, Chair
Department of Mechanical, Industrial, and Aerospace Engineering

August 2023 _____
Dr. Mourad Debbabi, Dean
Faculty of Engineering and Computer Science

Abstract

Dynamics of Hybrid-Actuated Soft Robots with Stiffness Adaptation for Robot-Assisted Interventions

Majid Roshanfar, Ph.D.

Concordia University, 2023

The lack of adaptability in surgical instruments has limited the widespread adoption of robot-assisted interventions. The objective of this doctoral research was to address the inherent trade-off between the deformability and force transmission capacity of minimally invasive surgery (MIS) instruments. Current instruments, such as catheters, tend to exhibit either excessive flexibility, rendering them unsuitable for load-bearing tasks, or excessive stiffness, limiting maneuverability in anatomical regions with complex geometry. The hypothesis underlying this research proposed that by controlling the stiffness of a soft robot, which serves as an MIS instrument, it is possible to increase its deformability during the steering phase while increasing stiffness during load-bearing tasks to ensure effective force transmission. The approach put forth in this study utilized a hybrid air-tendon actuation system, which has not yet been explored in existing literature for stiffness adaptation. To justify this hypothesis, a continuum mechanics model based on the nonlinear Cosserat rod method, incorporating hyperelastic material properties and accommodating large deformation kinematics, was developed and experimentally validated. This model demonstrated the feasibility of stiffness control through hybrid actuation. Initially, a static Cosserat rod model was developed and validated in a 2D context. Furthermore, the model was refined to incorporate the hyperelastic properties of the soft material, and its validity was established in 3D scenarios. Next, a dynamic model for the Cosserat rod was developed and validated using experimental data. Lastly, a parametric finite element method was used to optimize the geometry of the soft robot based on a defined goal function to reduce unnecessary radial expansion during inflation and enhance axial force transmission.

Acknowledgments

I would like to express my deepest gratitude for the opportunity to conduct my doctoral research at Concordia University, which is situated on unceded Indigenous lands. I want to begin by acknowledging the Kanyen'kehà:ka Nation as the custodians of Tiohtià:ke/Montréal, the lands, and waters upon which we gather today. This thesis represents a significant milestone in my academic journey, which has been filled with moments of joy and memorable experiences. I am deeply thankful for the abundance of happy days that I have experienced during my doctoral study. Among these, two particular days stand out in my memory: January 3rd, 2020, the day I got married, and June 2nd, 2022, when I received the Fonds de recherche du Québec – Nature et Technologies (FRQNT) award. These moments have brought great happiness and have been pivotal in shaping my personal and academic growth. However, it is essential to acknowledge that my journey has not been without moments of sadness. January 8th, 2020, remains etched in my memory as a day of profound grief when the tragic incident of flight PS752 claimed the lives of some of my friends from Concordia University and the University of Alberta. Their loss has had a lasting impact on me, and I carry their memory with me as a reminder of the preciousness and fragility of life.

I owe an immeasurable debt of gratitude to my beloved wife, Sahar Khademioore. Her love, support, inspiration, companionship, and sacrifices have made all my life's achievements possible. Sahar, you have been an exceptional partner, standing by my side, fulfilling life's responsibilities, and supporting me even when I was not at my best. I consider myself incredibly fortunate, blessed, and deeply grateful to have you in my life. I would like to extend my sincere appreciation to my supervisor, Dr. Javad Dargahi, for providing me with invaluable learning opportunities. His constant support, paternal guidance, and visionary approach to research have been instrumental in propelling

me forward. I am also grateful to the members of my examination committee, namely, Dr. Sheila Russo, Dr. Mojtaba Kahrizi, Dr. Sivakumar Narayanswamy, and Dr. Mojtaba Kheiri, for their dedicated time, diligent advice, and guidance throughout my doctoral study. Additionally, I would like to express my heartfelt gratitude to my mentor, Dr. Amir Hooshair, whose commitment and support have been invaluable throughout my journey.

I am thankful to Dr. Jake Barralet from McGill University Health Center for the collaborative experience during my term as a Surgical Innovation Fellow. Additionally, I would like to acknowledge Dr. Julien Clin, Dr. Bahe Hachem, Dr. Cyril Sender, Mr. Louis-Philippe Caron, and my colleagues at Spinologics, Montreal, for their support during my industrial internship. Furthermore, I extend my gratitude to Ms. Negin Ashouri, Ms. Inara Lalani, Mr. Erfan Fatehi, and Dr. Mihnea Gangal for granting me the opportunity to embark on the remarkable journey with FemTherapeutics. My journey has been enriched by the presence of exceptional friends like Dr. Soheil Samadi, Mr. Hesam Noferesti, Mr. Pooya Salehi, Mr. Farid Ehsani, Mr. Mohammadreza Eskandari, Mr. Hesam Jalalian, and colleagues. I am indebted to each one of them for the valuable lessons I have learned. Specifically, I extend my gratitude to my colleagues at the Surgical Robotics Lab (SRL), including Dr. Amir Molaei, Dr. Sevin Samadi, Dr. Naghme Bandari, Dr. Masoud Razabn, Mr. Amir Sayadi, Mr. Mohammad Jolaei, Mr. Pedram Fekri, Mr. Saman Namvar, Mr. Alireza Payami, Mr. Salar Taki, Mr. Nima Foomany, Mr. Hamidreza Nourani, Mr. Hamidreza Khodashenas, Ms. Tannaz Torkaman, Ms. Pegah Yaftiyan, Mr. Reza Khoshbakht, and Mr. Farzad Famouri.

I am grateful for the financial support provided by the Natural Sciences and Engineering Research Council (NSERC) of Canada through the CREATE Doctoral Fellowship for Surgical Innovation at McGill University. Furthermore, I acknowledge the support of FRQNT, Concordia University, the School of Graduate Studies, and Gina Cody School of Engineering, which generously awarded me a Doctoral Fellowship. Special thanks go to the staff of the Engineering Department, especially Ms. Leslie Hossein, Ms. Arlene Zimmerman, and Ms. Maureen Thuringer, for their kind support. Lastly, I would like to thank the tireless efforts of my parents, Dr. Aziz Roshanfar and Parvaneh, who devoted themselves to supporting me, my brother Ahmad, and my sister Najme. Their prayers and blessings have always been with me, and I am forever grateful for their unconditional love and support.

Contents

List of Figures

List of Tables

Nomenclature

$2D$	Two Dimensional
$2MR$	Two-terms Mooney–Rivlin
$3D$	Three Dimensional
$AFib$	Atrial Fibrillation
BC	Boundary Condition
BDF	Backward Differentiation Formulas
BVP	Boundary Value Problem
CC	Constant Curvature
CPU	Central Processing Unit
DC	Direct Current
DOF	Degree of Freedom
EAP	Electroactive Polymer
$EIAs$	Elastic Inflatable Actuators
FEA	Finite Element Analysis
FEM	Finite Element Modeling
FOV	Field of View

GA Genetic Algorithm

ISO International Organization for Standardization

IVP Initial Value Problem

MAE Mean-Absolute-Error

MIS Minimally Invasive Surgery

MRI Magnetic Resonance Imaging

NiTi Nitinol

ODE Ordinary Differential Equation

PCC Piecewise Constant Curvature

PCI Percutaneous Coronary Intervention

PDE Partial Differential Equation

PDMS Polydimethylsiloxane

PE Polyethylene

PET Polyethylene Terephthalate

PP Polypropylene

PPI Peripheral Interventions

PV Pulmonary Vein

RAM Random-Access Memory

RCI Robot-assisted Catheter Intervention

RFA Radio Frequency Ablation

RMIS Robotic-Assisted Minimally Invasive Surgery

RMSE Root-mean-square Error

RSO Response Surface Optimization

SMA Shape Memory Alloy

UTM Universal Testing Machine

VC Variable Curvature

Chapter 1

Introduction

1.1 Background

Minimally invasive surgery (MIS) has revolutionized the field of medical procedures by providing a safer and less invasive alternative to traditional open surgery. It employs image-guided techniques in a dynamically changing and unstructured environment to perform complicated tasks inside the human body. By utilizing long, rigid, or flexible instruments inserted through small incisions or natural orifices [1], MIS enables surgeons to address specific conditions with precision and efficiency while minimizing patient discomfort. Compared to open surgery, which typically involves large incisions and extended hospital stays, MIS offers numerous advantages [2]. One of the primary benefits is enhanced patient safety. The use of smaller incisions reduces the risk of complications such as infections and excessive bleeding. Moreover, the minimally invasive approach minimizes trauma to surrounding tissues, organs, and blood vessels, leading to reduced postoperative pain and inconvenience.

Another significant advantage of MIS is the shorter recovery time it affords. The smaller incisions promote faster healing, allowing patients to resume their daily activities sooner. The reduced trauma to the body also facilitates a faster recovery process by minimizing disruption to the natural healing mechanisms. This accelerated recuperation not only benefits patients but also alleviates the pressure on healthcare systems by freeing up hospital beds for other critical cases. Many procedures that previously required extended hospital stays can now be performed on an outpatient basis

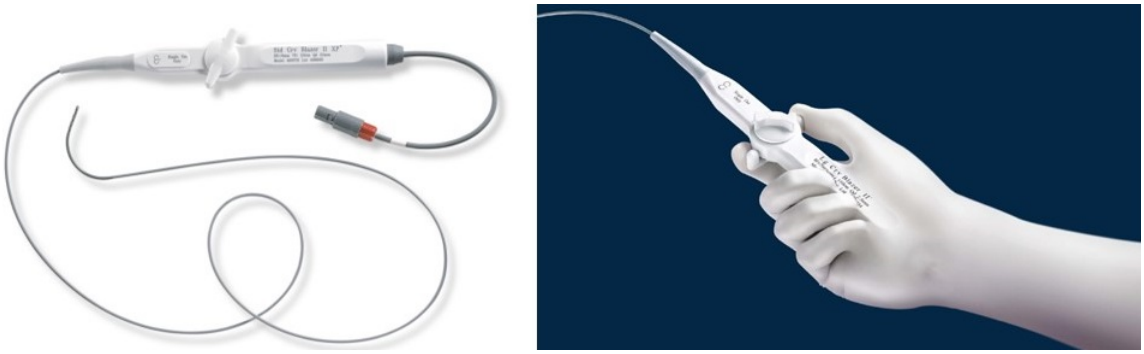

Figure 1.1: Steerable catheter, Blazer II XP, Model 4770THK2, Boston Scientific.

or with shorter hospital stays. This not only reduces costs but also minimizes the risk of hospital-acquired infections, which are a major concern in healthcare settings. The advancements in MIS have enabled surgeons to tackle a wide range of conditions through minimally invasive approaches. Procedures that previously necessitated large incisions can now be performed with precision using specialized instruments and under real-time imaging guidance.

MIS procedures necessitate a diverse range of instruments, including handheld and auxiliary tools, such as cutters, electrosurgical instruments, and inflation systems. Among these instruments, the catheter holds the utmost importance in the context of MIS. A catheter is an elongated, slender, and elastic tube or wire, typically measuring up to 2 meters [3]. Figure 1.1 shows a steerable catheter from Boston Scientific. The utilization of catheter-based interventions has experienced a substantial upsurge owing to the numerous advantages offered by minimally invasive procedures. Presently, a broad spectrum of surgical disciplines, including neurosurgery [4], cosmetic surgery [5], urology [6], obstetrics and gynecology [7], ophthalmology [8], cardiovascular [9], orthopedic surgery [10], and laparoscopy [11], rely on catheters for accomplishing their respective procedures. Nevertheless, the majority of these surgeries still rely on manual manipulation using conventional catheters. These conventional catheters exhibit limited flexibility and a restricted range of motion, thereby necessitating the surgeon's expertise to navigate and interact with the target tissue. The complex nature of the anatomical pathway, combined with the catheter's inherent stiffness and the absence of contact force information, give rise to challenges in terms of dexterity, safety, and stability during catheter-based operations.

To overcome the limitations of conventional catheters, steerable catheters have been developed.

These catheters are navigated using a mechanism that can be driven by the surgeon or by a robot [12]. Steerable catheters offer several advantages, including improved stability during operation and enhanced accessibility to tortuous anatomy. Steerable catheters can be classified based on their actuation principles. There are four main categories:

(1) **Tendon-driven**: In tendon-driven catheters, a set of tendons is used to control the orientation of the catheter's distal tip. The backbone of these catheters is typically made of a super-elastic material called nitinol (NiTi) alloy. Tendon-driven catheters are widely used in the field because they are relatively easy to use and provide accurate control [13].

(2) **Magnetic navigation**: Catheters using magnetic navigation rely on magnetic fields to guide their movement within the body. These catheters are controlled externally by manipulating the magnetic field, allowing precise navigation through complex anatomical structures.

(3) **Soft material-driven**: This category includes catheters that utilize various soft materials to achieve flexibility and steerability. Examples include catheters employing shape memory effects, concentric tubes, conducting polymers, as well as hydraulic and pneumatic pressure-driven mechanisms. These catheters can adapt their shape or respond to external stimuli to navigate through challenging anatomical pathways.

(4) **Hybrid actuation**: Hybrid actuated catheters combine multiple actuation principles to enhance their steering capabilities. They may integrate features from tendon-driven, magnetic navigation, or soft material-driven catheters to achieve improved performance and versatility.

While tendon-driven catheters are currently the mainstream choice due to their ease of use and accuracy, other types of steerable catheters offer unique advantages depending on the specific application or anatomical challenges. The development of steerable catheters has significantly advanced the field of minimally invasive procedures, enabling safer and more precise interventions in complex anatomies. In the magnetic-driven navigation approach, a catheter equipped with a distal magnetic tip is guided through the patient's body using strategically placed large magnets on each side of the patient [14]. However, this technique faces a significant limitation due to the nonlinear behavior of the magnets, particularly hysteresis, which poses challenges for precise control. An alternative

approach involves the use of soft material-driven catheters that can achieve continuous bending through their own structures, eliminating the need for external mechanisms. One example of such a material is shape memory alloy (SMA), which can be manufactured in extremely small diameters (less than 1 mm) [15]. Nevertheless, navigating the catheter using this method presents a different challenge - the precise control of temperature within the patient's body.

1.1.1 State-of-the-art for Robot-Assisted Interventions

Surgical robots have transformed the field of MIS and gained global acceptance among surgeons. These robotic systems have significantly enhanced accuracy, stability, and motion scaling. However, their inability to navigate complex pathways, inflexibility, constant stiffness, and sometimes large size limit their access to certain target anatomies. To address these limitations, several robotic systems were developed to mitigate the risks associated with minimally invasive interventions.

In 2004, Hansen Medical (Sensei Robotics, Mountain View, CA, USA) introduced an endovascular robotic catheter system designed for electrophysiological mapping and radiofrequency ablation. This system, known as the electromechanical master-slave system, enables remote control of a steerable guide catheter's positioning within the heart. Subsequently, in 2013, the Magellan robotic system (Hansen Medical, Mountain View, CA, USA) was launched for peripheral interventions (PPI) and worked in conjunction with compatible steerable catheters. The distal tip of Magellan catheters can be actively steered, allowing bending along two perpendicular axes through a cable-driven mechanism [16].

The first generation of remote-control robots for percutaneous coronary intervention (PCI) was developed by Beyar et al. [17]. This system comprised an operator module equipped with a touch screen monitor, a joystick, and a patient module that served as a three degrees-of-freedom (DOF) robot. The patient module enabled the insertion, retraction, and rotation of a guidewire, as well as the insertion and retraction of endoluminal devices such as balloons, stents, or injection catheters [17]. This system, known as CorPath, was launched by Corindus Inc., Waltham, MA, USA, in 2012. Subsequently, a newer generation, CorPath GRX, received clearance for use in robotic PPI procedures. Additionally, there are other products available for robotic-assisted interventions, such

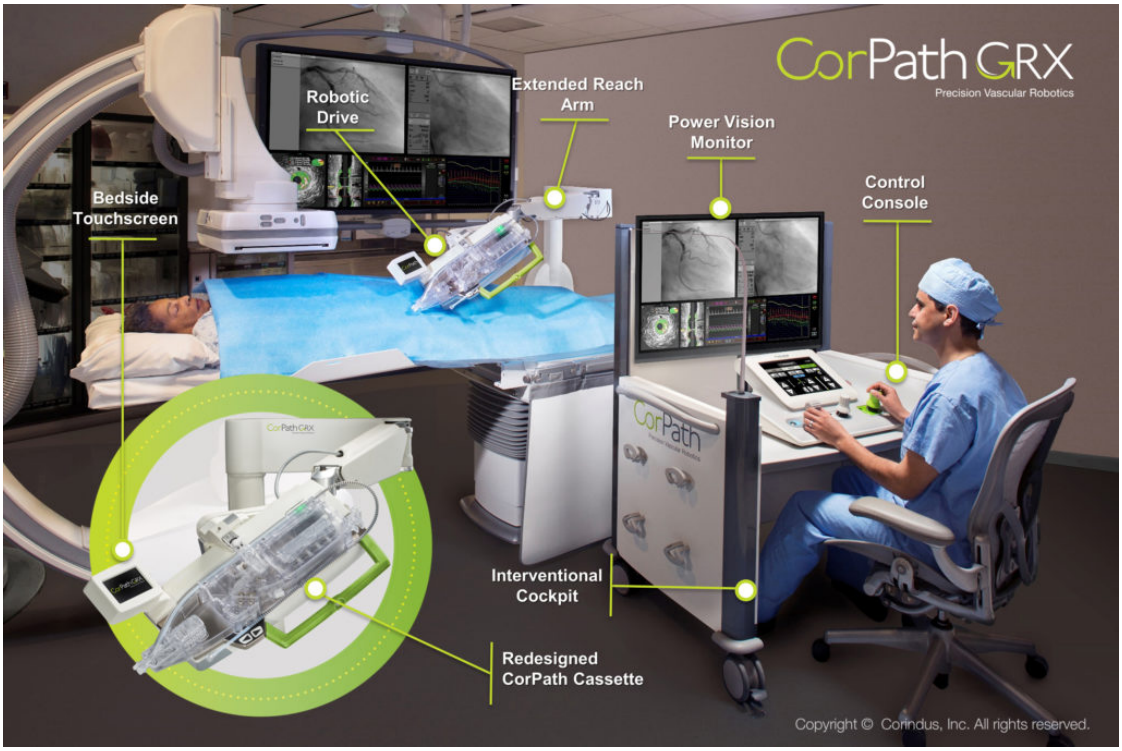

Figure 1.2: System components of a robot-assisted intervention procedure, CorPath GRX

as the MONARCH Platform (Auris Health, Inc.) [18] for endoscopy in lung cancer treatment and the Flex Robotic System (Medrobotics, MA, USA) [19] for visualization and surgical site access to the oropharynx. Furthermore, the Niobe and Genesis magnetic navigation systems (Stereotaxis Inc., St. Louis, USA) are examples of systems consisting of two robotically controlled magnets adjacent to the patient's table. These systems allow physicians to precisely direct and steer a catheter embedded with a magnet at its tip.

Encouraging clinical outcomes have been reported for robotic minimally invasive interventions in human subjects [17]. Weisz et al. [20] documented a notable achievement, demonstrating a 95% decrease in X-ray exposure for the surgeon, coupled with observed surgical advantages. Figure 1.2 illustrated the system components of a robot-assisted intervention procedure from CorPath GRX, serving as a representative case in this context.

The significant challenge encountered in past robotic intervention systems was the constant stiffness of the instruments [21]. The necessity for adaptivity in robotic systems had been well-established in the literature, as the absence of adaptivity resulted in oversteering and vessel rupture

[9]. Studies have indicated a substantial risk of embolization, perforation, thrombosis, and dissection associated with excessive contact force between the catheter or guidewire and the vascular wall [22]. As an alternative, flexible instruments were utilized when rigid instruments proved ineffective or could not reach the surgical site. In cases where flexible devices also proved ineffective, open surgery remained the sole option. Ongoing research aimed to enhance the usability of soft robots in minimally invasive interventions by combining the precise controllability of rigid robots, the accessibility provided by flexible instruments, and the safety offered by soft materials to overcome existing limitations. The challenges faced by current MIS instruments necessitated the development of compliant, variable stiffness, and safe new instruments [23]. By harnessing these capabilities and addressing the force-flexibility dilemma, the development of next-generation robotic instruments for robot-assisted interventions would be facilitated.

1.2 Soft Robotics in MIS

A bibliometric analysis was conducted, revealing a growing interest in soft robots [24]. Furthermore, a literature review [3] demonstrated an increase in the utilization of soft robots in the field of MIS applications since 2013, primarily driven by the STIFF-FLOP project [25]. The inherent compliance of the structural materials employed in the construction of soft robots, such as elastomers, makes them highly suitable for interacting with unstructured environments [26] and medical applications [27].

Invasive surgical applications for elastic inflatable actuators (EIAs) have garnered significant attention following the proposal by Lazeroms et al. [28] to employ bending EIAs as minimally invasive hydraulic forceps with force-feedback. Subsequently, Konishi et al. [29] introduced an actuator featuring electrically conductive paths, thereby prototyping an actuator capable of enveloping nerves. Additionally, Ikuta et al. [30, 31, 32] developed an intervention tool with local DOF, incorporating two single-chamber bending actuators in series that can be selectively actuated. By refining the design, they succeeded in creating the world's smallest active catheter at the time, measuring 0.4 mm in diameter [33].

1.2.1 Soft Robotics: Working Principles

Soft robots typically operate based on three primary principles: continuum robots, peristaltic robots, and serial robots. Continuum robots, characterized by their absence of rigid links or joints, possess the ability to continuously bend. These robots require only a single point of entry and can achieve significant bending angles, enabling exploration of internal body structures that would otherwise be inaccessible using rigid instruments. However, a major drawback of continuum robots is their diminishing force exertion capability along their length [3].

Peristaltic robots, inspired by creatures such as earthworms, inchworms, and snakes, are self-propelled robots. Although these three models differ in specific design, they all rely on anisotropic friction to achieve locomotion [34]. For example, soft peristaltic robots employed in colonoscopy procedures allow access to the colon without causing stretching, injury, or discomfort to the patient [35].

Another category of soft robots is soft serial robots, which comprise multiple prismatic or rotational joints connected by flexible links [36]. However, soft serial robots suffer from comparatively low force transmission capacity due to the high deformability of their links and joints [2]. Typically, these robots are utilized as grippers at the distal end of an endoscope [37, 38].

1.2.2 Soft Robotics: Materials

A device constructed from materials with significantly smaller elastic moduli than human tissues, such as skin and muscle tissue (which have a modulus on the order of 10^2-10^6 Pa [39]), can still be classified as a soft robot when the materials' cross-sectional areas are small [40]. Elastomers, such as polydimethylsiloxane (PDMS) and polyurethane, as well as thin layers of plastics like polyethylene (PE), polyethylene terephthalate (PET), or polypropylene (PP), are among the materials commonly used for soft robots. Furthermore, medical devices made of soft materials are likely to be compatible with magnetic resonance imaging (MRI). It is important to note that a robot's stiffness, force exertion, and deformations are highly influenced by the properties of the elastomer utilized.

1.2.3 Soft Robotics: Actuation Methods

Various methods for actuating soft robots have been proposed in studies. These methods include pneumatic [41], hydraulic [42], cable-driven [43], electroactive polymers (EAPs) [44], magnetic [45], and SMA [42]. The choice of actuation depends on factors such as the range of motion in bending and elongation, contribution to stiffness, and force transmission capacity.

Pneumatic and hydraulic soft robots incorporate internal pressure chambers, which function as small reservoirs. The internal pressure within these chambers causes longitudinal and lateral deformation in the body of the soft robot. These deformations also affect the apparent stiffness of the robot by altering the strain of the nonlinear material on its constitutive curve (material stiffness) and modifying the robot's geometry (geometric stiffness) [46, 47]. Fluidic actuation typically results in significant stiffness changes; however, it offers a limited range of motion compared to cable-driven soft robots.

Cable-driven robots employ two or more cables, also known as tendons, anchored to the robot's tip or specific points on its body. Pulling and releasing these cables enables high precision and repeatable deformation [48]. Since changes in the cable length only affect the shape of the soft robot, the stiffness change in this mode of actuation is solely related to geometric factors. Therefore, the stiffness change is considerably less compared to pneumatic actuation. Cable driving allows for high-force transmission capacities by increasing the cable diameter and making the robot's body bulkier. However, such an increase in size is generally undesirable for MIS applications, where miniaturization is advantageous.

On the other hand, SMAs induce buckling of the structure through changes in the electrical current applied to an electro-active metal, such as Ni-Ti alloys. SMA-driven robots offer advantages in terms of a large workspace and high force exertion capacity. Nevertheless, the prime limitations of SMA actuation for soft robots are the speed of actuation and the risk of current leakage to the body and heat generation [49]. A recent proposal in [50] suggests the combination of two or more actuation systems for soft robots. However, rigorous modeling and control of such combined systems still require further study.

1.2.4 Soft Robotics: Mechanical Models

Euler-Bernoulli's beam theory was widely adopted in literature as the most commonly used model for describing the overall deformation of bending actuators. According to this theory, a soft robot is represented as a beam subjected to a moment at its boundaries, arising from the axial component of the applied pressure. While Euler-Bernoulli's beam theory is unsuitable for large bending deformations where the cross-sectional planes change relative to the actuator axis, it has proven to be a valuable method for the fundamental analysis of bending EIAs [51].

Simulations involving these actuators pose a particular challenge due to the alteration of the cross-section during inflation. Consequently, the unpressurized cross-section only provides a reasonable approximation at low pressures. To address this limitation, researchers have proposed enhancements by updating the actuator's cross-section as it inflates [46]. Experimental findings have demonstrated that the relationship between curvature and bending moment becomes highly nonlinear, rendering Euler-Bernoulli's beam theory invalid [52]. As an alternative, the constant curvature (CC), piecewise constant curvature (PCC) [53], and variable curvature (VC) [54] models have been predominantly employed in the literature to characterize the kinematic behavior of soft robots.

Although the CC approximation has proven successful in various soft robots, it is not effective for dynamic modeling, primarily due to the nonlinear response of elastomeric materials to strain. Furthermore, the CC model simplifies the kinematics significantly, resulting in reduced accuracy and the potential for local singularities, especially when substantial body and external loads are present. Therefore, the CC approach is most effective when inertia effects can be neglected [55].

To account for general loading conditions, researchers have proposed treating the soft robot as a one-dimensional slender object using the Cosserat rod model [56, 57, 58]. This modeling approach, capable of incorporating the effects of gravity, torsion, and external loading, offers benefits and has shown promising results in the dynamic modeling of soft robots. It has been demonstrated that this approach provides greater accuracy compared to the CC model, particularly when shear and gravitational loading are considered [59].

1.2.5 Soft Robotics: Manufacturing Methods

Molding [60], extrusion [61], 3D printing [62], shape deposition [63], soft lithography [64], micro stereolithography [65], and spin-coating [66] were identified as the most commonly utilized methods for manufacturing soft robots. Among these, molding emerged as the predominant modality. The literature emphasizes various factors to be considered when selecting a manufacturing method, including repeatability, final quality, size limitations, time requirements, and material biocompatibility.

1.3 Research Motivations

Through a comprehensive review of the existing literature, significant knowledge gaps were identified in accurately modeling soft medical instruments for use in robot-assisted surgical interventions. Specifically, two major areas requiring attention emerged: the adaptivity of these instruments' stiffness during interventions and task performance, and the optimization of their geometry to mitigate undesired expansion, commonly referred to as the "ballooning effect". Consequently, the primary objective of this doctoral research was to comprehensively address these limitations by introducing a continuum-based model of a soft robot, considering a hybrid-actuation modality involving air pressure and tendon tension. This section provides a summary of the rationale and motivation behind this research.

(1) Robot-assisted interventions have demonstrated superior surgical accuracy and improved radiation safety for both patients and surgeons. However, clinical studies have revealed a significant technical limitation in the lack of adaptivity of the end effectors of these instruments, hindering the widespread adoption of this system. Previous studies, including the one conducted by Cianchetti et al. [67], have highlighted the necessity for stiffness adaptation in surgical instruments. Currently, there are no commercially available catheters that possess the capability to adjust their stiffness according to specific clinical requirements.

(2) This study aimed to introduce a new technological requirement into the surgical workflow,

specifically by integrating custom-designed catheters with adjustable stiffness tailored to individual clinical needs. With the rapid advancements in robot-assisted systems, there is an urgent clinical demand for a modular end effector that is compatible with existing systems while offering new capabilities. Therefore, it is crucial to ensure that the proposed instrument can effectively utilize the available hard and soft resources within the interventional workflow. Considering that X-ray imaging, commonly known as fluoroscopy, is the standard-of-care in this field, any new instrument must take into account its utilization and compatibility.

(3) Currently, commercial catheters are flexible but their stiffness remains constant during the operation. This means that the maneuverability of the catheter remains constant during the insertion phase, and once it reaches the target, there is no option to adjust the stiffness. The primary motivation behind the current design is not only to increase the maneuverability of the catheter in different trajectories but also to enhance safety throughout the procedure.

(4) Although most of the currently proposed mechanical models are capable of measuring the deformation and tip force of the catheter, knowledge of the contact force between the entire length of the catheter and the environment is clinically necessary and affects the catheter's stiffness.

By addressing these research gaps and incorporating adaptivity and optimized geometry into soft medical instruments, this doctoral research aims to advance the field of robot-assisted interventions. The findings from this study have the potential to improve surgical outcomes, enhance patient safety, and contribute to the broader adoption of robot-assisted systems in clinical practice.

1.4 Research Objectives

In order to address the knowledge gaps outlined, this research aims to achieve the following specific objectives:

(1) To identify the design requirements relevant to stiffness adaptation in robot-assisted intervention procedures. This includes determining the appropriate instrument diameter for each task, operational range, required accuracy and resolution.

(2) To conceptualize, design, and validate an alternative configuration for catheters used in robot-assisted intervention systems that can effectively accommodate the identified design requirements.

(3) To develop, implement, and validate a three-dimensional (3D) method for estimating the stiffness of the catheter while adjusting the actuation inputs. This method should demonstrate an accuracy level of less than 10% error of full-scale within the operational range of insertion forces.

(4) To develop a precise model capable of capturing the dynamic effects and quasi-static deformation of the soft catheter. This model will take into account the material nonlinearity and consider both modes of actuation.

(5) To optimize the geometry of the soft catheter, including its outer diameter, length, and the positioning of tendon and air pressure channels. The aim is to enhance the performance of the catheter and reduce the required actuation efforts.

1.5 Research Scope

The doctoral study focused on the design, modeling, and experimental validation of hybrid-actuated soft robots with controllable stiffness. The aim was to develop soft robots capable of being driven by both compressed air (pressure) and tendon drivers (tension), thereby enabling variable stiffness through different combinations of mechanical stimuli. This variability in stiffness would allow the soft robot to exhibit deformability and force transmission capabilities, which could be dynamically controlled during various phases of minimally invasive robot-assisted interventional procedures. To accomplish this objective, several criteria had to be met:

(1) The derivation of continuum mechanics-based balance equations for the endovascular devices, considering large deformations.

(2) The development of a continuum mechanics-based model to accurately capture the material nonlinearity of the soft robot.

(3) The design of the soft robot with an outer diameter not exceeding 20 mm.

(4) The soft robot needed to possess sufficient flexibility to perform retroflexion, which involves a 180-degree bending motion.

(5) The mechanistic model, which establishes the relationship between the actuation stimuli and the stiffness of the soft robot, had to achieve an accuracy of at least 90%.

(6) The resolution of stiffness control through hybrid actuation should not exceed 10% of the full-scale stiffness range of the soft robot.

(7) The verification of the developed solution scheme by comparing it with commercial finite-element software to optimize the geometry of the soft robot.

1.6 Thesis Contributions

To the best of the author's knowledge, this study represented a pioneering effort to address the limitation of stiffness adaptation within the context of robot-assisted surgical interventions, utilizing a continuum-based mechanic model. The initial phase of this study involved the identification of key technological gaps that had impeded the progress of stiffness adaptation. Subsequently, a novel continuum mechanics model was formulated, drawing upon the nonlinear Cosserat rod model featuring a hyperelastic material model and accommodating large deformation kinematics. The validity of this model was verified through a combination of simulations and experimental investigations. This model not only establishes the viability of the proposed hybrid actuation and stiffness control concept but also outlines the planned experimental setup, encompassing the soft robot, pneumatic controller, tendon driver, and integration plan spanning system mechanics, electronics, and pneumatic components. With regards to addressing the existing gaps in knowledge within the literature, this research makes several significant contributions and introduces novel aspects:

(1) The derivation of the kinematics of the soft robot with consideration for large deformations, enabling a unified definition encompassing both small and large deformations.

(2) The development and validation of an identifier for estimating the stiffness of the soft robot, based on the Cosserat rod model.

(3) The incorporation of hyperelastic silicone material into the developed model, enhancing its realism and applicability.

(4) Parametric FEM simulations of the soft robot, aimed at optimizing its geometry for improved performance.

(5) Introducing hybrid actuation as a versatile approach to effectively modify and adjust the stiffness of soft robots.

(6) Presenting a novel mechanistic model for the adaptation of stiffness in pneumatic-tendon-based systems.

(7) Introducing a novel stiffness indicator and providing a precise mathematical definition, serving as a reliable surrogate for assessing flexural rigidity.

(8) Proposing a task-agnostic hybrid-actuation framework, suitable for diverse interventional procedures.

1.7 Publications

Outlined below are the notable contributions made by the author throughout the doctoral research:

Journal Papers

(1) Majid Roshanfar, Salar Taki, Amir Sayadi, Renzo Cecere, Javad Dargahi, Amir Hooshiar, *"Hyperelastic Modeling and Validation of Hybrid-Actuated Soft Robot with Pressure Stiffening"*, published in Journal of Micromachines, 2023 [68].

(2) Majid Roshanfar, Javad Dargahi, Amir Hooshiar, *"Cosserat Rod-Based Dynamic Modeling of a Hybrid-Actuated Soft Robot for Robot-Assisted Cardiac Ablation"*, submitted in Journal of Actuators, 2023.

(3) Majid Roshanfar, Javad Dargahi, Amir Hooshiar, *"Design Optimization of a Hybrid-Driven Soft Surgical Robot with Biomimetic Constraints"*, submitted in Journal of Biomimetics, 2023.

Conference Papers

(1) Majid Roshanfar, Amir Sayadi, Javad Dargahi, Amir Hooshiar, *"Stiffness Adaptation of a Hybrid Soft Surgical Robot for Improved Safety in Interventional Surgery"*, published in 2022 annual international conference of the IEEE Engineering in Medicine & Biology Society (EMBC) [69].

(2) Majid Roshanfar, Javad Dargahi, Amir Hooshiar, *"Toward Semi-Autonomous Stiffness Adaptation of Pneumatic Soft Robots: Modeling and Validation"*, published in 2021 IEEE International Conference on Autonomous Systems (ICAS) [70].

(3) Majid Roshanfar, Naghmeh Bandari, Amir Hooshiar, Javad Dargahi, *"Addressing the COVID-19 Healthcare Needs by Teleoperated Robot-Assisted Intervention"*, published in ICRA 2021 Workshop, Impact of COVID-19 on Medical Robotics and Wearables Research: Learning from the Past and Strategizing for the Future [71].

Other Publications

(1) Majid Roshanfar, Pedram Fekri, Javad Dargahi, *"A Deep Learning Model for Tip Force Estimation on Steerable Catheters Via Learning-from-Simulation"*, published in 2023 Hamlyn Symposium on Medical Robotics [72].

(2) Seyedfarzad Famouri, Pedram Fekri, Majid Roshanfar, Javad Dargahi, *"Towards Surgical Skill Modeling in Cardiac Ablation Using Deep Learning"*, published in 2023 international conference on Methods and Models in Automation and Robotics (MMAR) [73].

(3) Majid Roshanfar, Pedram Fekri, Javad Dargahi, *"Toward Autonomous Cardiac Catheterization Through a Parametric Finite Element Simulation With Experimental Validation"*, published in 2023 international conference on Autonomic and Autonomous Systems (ICAS) [74].

(4) Tannaz Torkaman, Majid Roshanfar, Javad Dargahi, Amir Hooshiar, *"Embedded Six-DOF Force-Torque Sensor for Soft Robots with Learning-based Calibration"*, published in 2023 IEEE Sensors Journal [75].

(5) Mohammad Haghayeghjahromi, M Roshanfar, J Dargahi, *"Analysis of Self-expanded and Balloon-expanded Coronary Stents using Finite Element Method"*, published in 2022 International Journal of Mechanical and Production Engineering (IJMPE) [76].

(6) Tannaz Torkaman, Majid Roshanfar, Javad Dargahi, Amir Hooshiar, *"Accurate Embedded Force Sensor for Soft Robots with Rate-dependent Deep Neural Calibration"*, published in 2022 IEEE International Symposium on Robotic and Sensors Environments (ROSE) [77].

(7) Mehrshad Alizadeh, Mohammad Choulaei, Majid Roshanfar, Javad Dargahi, *"Vibrational Characteristic of Heart Stent Using Finite Element Model"*, published in 2022 International Journal of Health Sciences (IJHS) [78].

(8) Tannaz Torkaman, Majid Roshanfar, Javad Dargahi, Amir Hooshiar, *"Analytical Modeling and Experimental Validation of a Gelatin-based Shape Sensor for Soft Robots"*, published in 2022 International Symposium on Medical Robotics (ISMR) [79].

1.8 Thesis Layout

The clinical requirements outlined in Chapter 1 were used as a basis for the objectives of this thesis. These objectives involved developing, verifying, and validating a mechanical model capable of precise, and reliable stiffness adjustment in robot-assisted intervention systems. Additionally, an extensive literature review was conducted to identify various actuation mechanisms, materials, and working conditions of soft robots. The aim was to select the most appropriate approach for stiffness adaptation in the context of robot-assisted surgical interventions. Subsequently, a feasibility study was carried out to create a model of a soft robot based on the Cosserat rod theory, assuming quasi-static conditions and initial value problem (IVP) constraints. This design included a central channel for air pressure and the relationship between internal pressure and soft robot stiffness was calculated in Chapter 2. This study confirmed the hypothesis of stiffness adaptation. In Chapter 3, the Cosserat

rod model was further improved by incorporating the nonlinearity of the silicon material using the two-terms Mooney–Rivlin (2MR) model, which was combined with the Cosserat rod model. Additionally, an identifier was introduced to measure the soft robot's stiffness based on tip force and tip displacement, as functions of the internal pressure. To validate the Cosserat rod model for applications requiring stiffness adaptation, Chapter 4 introduced three passages for tendons to validate the Cosserat rod model in a 3D space. The effect of tendon tension on the local strains of the soft robot was also captured, and the variation of flexural rigidity in response to chamber pressure was successfully validated against experimental results. In Chapter 5, the final improvement of the Cosserat rod model involved deriving a set of dynamic partial differential equations (PDEs) for the soft robot, taking into account the 2MR model and boundary value problem (BVP) conditions. This enabled a more comprehensive understanding of the soft robot's dynamic behavior. Finally, Chapter 6 focused on optimizing the geometry of the soft robot to minimize radial deformation and reduce actuation efforts, thereby making it more suitable for position-stiffness control. In summary, this study successfully met the clinical demand for a flexible tool with adaptable stiffness in procedures involving robot-assisted interventions, as discussed in Chapter 7.

Chapter 2

Toward Semi-Autonomous Stiffness Adaptation of Pneumatic Soft Robots: Modeling and Validation

The inherent constraint created by the constant stiffness of soft medical robots significantly limits their ability to transmit forces effectively. In order to overcome this constraint, the primary objective of the present study was to investigate the influence of chamber pressure on the stiffness characteristics of pneumatic soft robots. Consequently, a single-chamber pneumatic soft robot was precisely designed and fabricated for experimental purposes. Subsequently, a mechanistic model describing the behavior of the robot under external forces and varying chamber pressures was developed. The model was mathematically solved as an IVP, incorporating homogeneous Neumann and Dirichlet boundary conditions (BCs). A comprehensive comparison between the theoretical predictions and the experimental data related to tip displacement and stiffness was conducted, revealing consistent trends with a maximum discrepancy of 8.7%. These findings validate the viability of adjusting stiffness by regulating the chamber pressure in pneumatic soft robots.

2.1 Introduction

2.1.1 Background

Soft robots exhibit a range of advantageous characteristics that make them highly suitable for various applications within the domain of MIS. Nevertheless, a significant challenge arises when considering the practicality of employing soft surgical robots in such contexts. Typically, these robots are introduced into the patient's body either percutaneously or through existing anatomical orifices, subsequently being guided towards the target site. Consequently, their low stiffness becomes a highly desirable characteristic, facilitating optimal maneuverability and steering capabilities. However, once positioned at the intended target, such as during an ablation procedure as exemplified [13], the soft surgical robot must possess the capability to effectively transmit forces to the surrounding environment. Notably, the force transmission capacity of these robots is intrinsically linked to their inherent stiffness. Consequently, a delicate compromise arises between the desired deformability and the essential force transmission capacity of soft robots within the scope of MIS procedures.

In this context, the majority of the presently proposed soft MIS robotic systems exhibit constant stiffness, which is inherent to their material properties and structural design. However, a notable drawback of such robots is their limited maneuverability and force transmission capabilities due to their predetermined stiffness. For instance, a highly flexible robot may be proficient in navigating through narrow lumens, but it may lack the necessary force capacity. On the other hand, a rigid robot can exert substantial force, but it may encounter difficulties conforming to complex and convoluted trajectories. Consequently, the development of a soft robot with adjustable stiffness holds significant clinical relevance. Such a robot would enable the creation of control frameworks that can semi-autonomously modulate stiffness, thereby facilitating enhanced intraoperative adaptability to meet specific task requirements, including force capacity.

The motivation behind this study was to propose and validate a mechanistic model that investigates the influence of chamber pressure on the stiffness of pneumatic-driven soft robots. This model represents a crucial step toward future research endeavors aimed at developing a semi-autonomous framework for stiffness adaptation during interventional procedures employing soft surgical robots.

2.1.2 Related Studies

A range of soft robotic systems have been proposed for diverse applications in MIS, including cardiovascular interventions [9, 80], endoscopy [43], drug delivery [81], and general surgical procedures [82]. Soft robots theoretically offer infinite DOF. However, for the sake of simplification, researchers have commonly modeled the deformation of soft robots as a curve [83, 84, 85], or as a collection of small rigid segments interconnected by flexible joints [86]. Another widely used approach in the literature is the utilization of the PCC model [53]. More recently, the Cosserat rod model has gained traction for modeling soft robots in MIS applications, as it provides a unified formulation for addressing both small and large deformations, thereby simplifying the model derivation [58]. However, it is worth noting that, to the best of the author's knowledge, the impact of internal pressure on the structural stiffness variation of soft pneumatic robots has not yet been investigated.

2.1.3 Contributions

The study made several significant contributions, including:

(1) Introduction of a novel approach for modeling the deformation of a single-chamber pneumatic-driven soft flexure using the Cosserat rod model. This innovative method allowed for a more accurate representation of the flexure's behavior and provided insights into its mechanical properties.

(2) Development of a solution to the Cosserat model, treating the problem as an IVP. By solving the model for a given force, the study provided a practical and reliable method for predicting the flexure's response under different loading conditions.

(3) Thorough validation of the proposed model was achieved by using carefully designed experiments. By comparing the model predictions with experimental measurements, the study confirmed the accuracy and effectiveness of the Cosserat rod model in capturing the flexure's deformation behavior.

(4) Demonstration of the feasibility of stiffness modulation by manipulating the chamber pressure. The study successfully showcased the ability to modulate the flexure's stiffness by adjusting the pressure within the pneumatic chamber. This finding has practical implications for various applications that require adaptive or tunable stiffness mechanisms.

Overall, this study has made advancements in the field by introducing a novel modeling approach for the deformation analysis of a single-chamber pneumatic-driven soft flexure, employing the Cosserat rod model. The study not only presented this innovative method but also developed a robust solution technique for the Cosserat model, treating it as an IVP. This approach enables accurate predictions of the flexure's response under various loading conditions. Furthermore, the study rigorously validated the proposed model through a comprehensive experimental investigation.

2.2 Mechanistic Modeling

In this section, a systematic derivation of the kinematics and force balance equations is presented as a fundamental basis for understanding the underlying mechanics. These equations describe the relationship between the flexure's deformation and the forces acting upon it. Subsequently, the constitutive equation is derived, establishing a vital link between the applied forces and moments and the resulting kinematic displacements. This equation allows for a comprehensive characterization of the flexure's mechanical behavior. Moving forward, a solution schema for the IVP is introduced, offering a practical framework for solving the derived equations. This solution methodology enables the determination of the flexure's response under specific loading conditions, providing valuable insights into its deformation characteristics.

Additionally, the section addresses the derivation of stiffness from the tip force, a significant parameter influencing the flexure's behavior. By establishing a quantitative relationship between the applied force and the resulting stiffness, the study enables a comprehensive understanding of how the flexure's mechanical properties can be modulated and controlled. By presenting a step-by-step derivation of the kinematics and force balance equations, followed by the constitutive equation and the IVP solution schema, this section lays a solid foundation for comprehending the complex mechanics of the single-chamber pneumatic-driven soft flexure. Furthermore, the derivation of

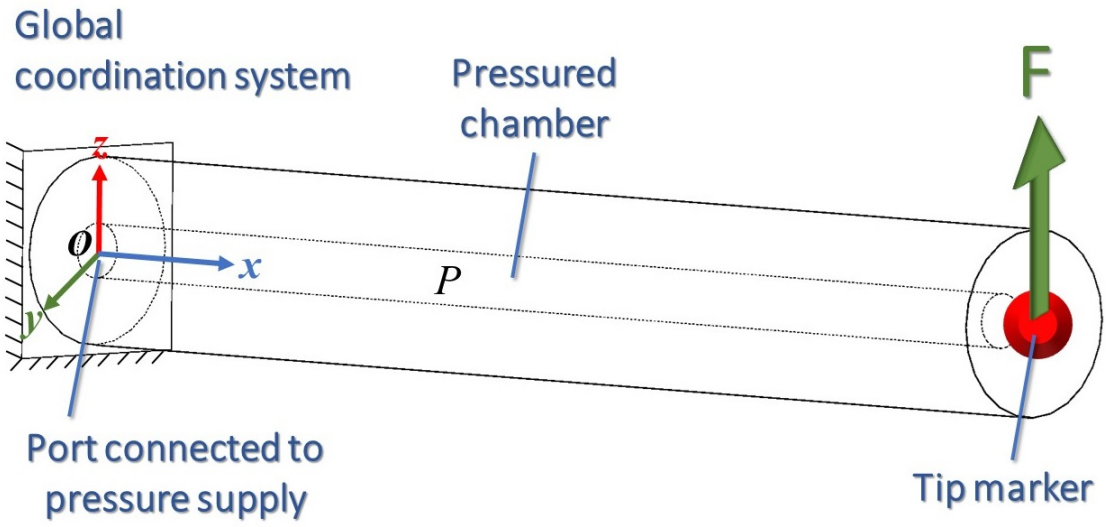

Figure 2.1: Schematic initial shape of the soft robot with internal pressure P an external tip force $\mathbf{F}$.

stiffness from the tip force enhances our ability to manipulate and optimize the flexure's behavior for various applications.

2.2.1 Kinematics

Figure 2.1 depicts a hollow soft robot with a cross-sectional area A in its initial shape, subjected to an internal pressure P, and an external tip force $\mathbf{F}$. The soft robot is also subjected to distributed gravitational force (weight). Each point on the backbone is parameterized by an arc parameter $s \in [0, L]$ and a locally orthonormal frame $\mathbf{R}(s)$ [53]. The position of any point on the arc, with respect to the base of the arc at a distance s, is defined by the position vector $\mathbf{p}(s)$. With the presented shape parameterization, the extension and shear strains along the backbone, $\mathbf{v}(s)$, are derived as shown in [87]:

$$\mathbf{v}(s) = \mathbf{R}^T(s)\frac{\partial \mathbf{p}(s)}{\partial s} \tag{1}$$

while the bending and torsion strains, **u(s)**, are [87]:

$$\mathbf{u}(s) = \left(\mathbf{R}^T(s)\frac{\partial \mathbf{R}(s)}{\partial s}\right)^{\vee} \tag{2}$$

where $(.)^{\vee}$ is the vee-operator, a mapping for $\mathfrak{so}(3)$ to $\mathbb{R}^3$ [88]. The kinematic equations relate the internal strains throughout the length of the robot to its parameterized shape.

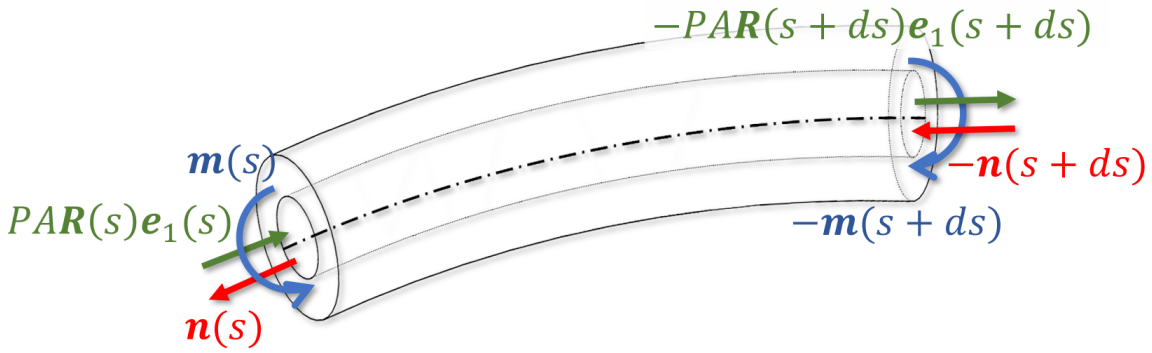

Figure 2.2: Free-body diagram of an infinitesimally small element along the length of the soft robot.

2.2.2 Force Balance Equations

Figure 2.2 depicts the free-body diagram of an infinitesimally small element along the length of the soft robot. From a mechanical standpoint, the chamber pressure generates a constant longitudinal tensile force along the length of the soft robot, with a magnitude of PA_{ch}, where A_{ch} represents the cross-sectional area of the chamber perpendicular to its backbone. It is noteworthy that the internal pressure exhibits symmetry about the longitudinal axis of the soft robot, thereby not affecting the force distribution in the perpendicular planes to the longitudinal axis. By utilizing the fundamental Cosserat rod theory, the quasi-static balance equations of the soft robot were derived [87].

$$\frac{\partial \mathbf{p}(s)}{\partial s} = \mathbf{R}(s)\mathbf{v}(s) \tag{3}$$

$$\frac{\partial \mathbf{R}(s)}{\partial s} = \mathbf{R}(s)(\mathbf{u}(s))^{\wedge} \tag{4}$$

$$\frac{\partial \mathbf{n}(s)}{\partial s} = -\rho A\mathbf{g} - PA_{ch}\mathbf{e}_1(s) - \mathbf{f} \tag{5}$$

$$\frac{\partial \mathbf{m}(s)}{\partial s} = -\left(\frac{\partial \mathbf{p}(s)}{\partial s}\right)^{\wedge}\mathbf{n}(s) - \mathbf{l} \tag{6}$$

where $\mathbf{n}(s)$ and $\mathbf{m}(s)$ are the internal force and moment vectors in the global coordination system, P is the chamber pressure, ρ is the material density (constant), $\mathbf{g}$ is the gravity vector, $\mathbf{e}_1$ is the first unit vector of $\mathbf{R}(s)$ (tangential to the backbone), $\mathbf{f}$ and $\mathbf{l}$ are any remaining external force and moment, and $(.)^{\wedge}$ is the hat-operator, a mapping from $\mathbb{R}^3$ to $\mathfrak{so}(3)$ such that $((.)^{\wedge})^{\vee} = (.)$ [88]. In

fact, (1–6) describe the nonlinear state-space representation of the the soft robot's mechanics with six state variables, i.e., $\begin{pmatrix}\mathbf{u}(s) & \mathbf{v}(s) & \mathbf{p}(s) & \mathbf{R}(s) & \mathbf{m}(s) & \mathbf{n}(s)\end{pmatrix}$.

2.2.3 Constitutive Equations

Typically, soft robots are constructed using hyperelastic elastomers. The mechanical properties of hyperelastic materials vary with local stretches. However, for a given stretch (at any location s), the tangent moduli $\mathbf{K}_{se}$ and $\mathbf{K}_{bt}$ represent the mechanical stiffness for unit length in shear and elongation, respectively. To determine the tangent moduli, a 2MR constitutive model is commonly assumed to describe the material behavior of the soft robot. (7) presents the 2MR model for uniaxial elongation:

$$T_{11} = 2(c_{01} + \frac{c_{10}}{\lambda})(\lambda^2 - \lambda^{-1}) \tag{7}$$

with T_{11} longitudinal nominal stress, λ longitudinal stretch, c_{01} and c_{10} as material constants. Moreover, the initial shear modulus $G_\circ$ and initial Hooke's modulus $E_\circ$ of 2MR material is obtained by:

$$G_\circ = 2(c_{01} + c_{10}) \tag{8}$$

$$E_\circ = 2G_\circ(1 + \vartheta) \tag{9}$$

with ϑ as the Poisson's ratio that is ≈ 0.5 for near-incompressible elastomers. Based on the Cosserat rod model, the basic linear elastic constitutive equations are [87]:

$$\mathbf{n}(s) = \mathbf{R}(s)\mathbf{K}_{se}\Big(\mathbf{v}(s) - \mathbf{v}^\star(s)\Big) \tag{10}$$

$$\mathbf{m}(s) = \mathbf{R}(s)\mathbf{K}_{bt}\Big(\mathbf{u}(s) - \mathbf{u}^\star(s)\Big) \tag{11}$$

where $(.)^\star$ refers to the state variables before deformation (initial state). Assuming, an initially straight soft robot extended along the global $x-$axis, $\mathbf{v}^\star(s) = \begin{pmatrix}1 & 0 & 0\end{pmatrix}^T$ and $\mathbf{u}^\star(s) = \mathbf{0}$. Also,

substituting the derived shear and Hooke's moduli the tangent stiffness matrices were obtained as:

$$\mathbf{K}_{se} = \text{diag}\begin{pmatrix} E_\circ A & G_\circ A & G_\circ A \end{pmatrix} \tag{12}$$

$$\mathbf{K}_{bt} = \text{diag}\begin{pmatrix} 2G_\circ I & E_\circ I & E_\circ I \end{pmatrix} \tag{13}$$

where I is the second moment of inertia of the soft robot's cross-section perpendicular to the backbone. The soft robot was also subjected to homogenous Dirichlet and Neumann BCs at $s = 0$ that were formulated as:

$$\mathbf{p}(s)|_{s=0} = \begin{pmatrix} 0 & 0 & 0 \end{pmatrix}^T \tag{14}$$

$$\mathbf{v}(s)|_{s=0} = \begin{pmatrix} 1 & 0 & 0 \end{pmatrix}^T \tag{15}$$

$$\mathbf{R}(s)|_{s=0} = \mathbf{I}_{3\times 3} \tag{16}$$

$$\mathbf{u}(s)|_{s=0} = \mathbf{0} \tag{17}$$

Also, it was assumed that the reaction forces at $s = 0$ were available by reading the force and moments from a six-DOF force/torque sensor placed at $s = 0$. Therefore, two additional BCs were formulated as:

$$\mathbf{n}(s)|_{s=0} = -\mathbf{n}_\circ \tag{18}$$

$$\mathbf{m}(s)|_{s=0} = -\mathbf{m}_\circ \tag{19}$$

where $\mathbf{n}_\circ$ and $\mathbf{m}_\circ$ were the force and torque vectors in the global coordination system, directly measured at $s = 0$.

2.2.4 Solution Schema

In order to find the deformation of the soft robot, initially the constitutive equations were substituted into the force and moment balance equations. Afterward, by assuming *a-priori* knowledge of the reaction forces and moments at the $s = 0$, the system of nonlinear differential equations (1–6) were integrated using 4-th order Runge-Kutta (RK4) method with a step-size of $\delta s = \frac{L}{100}$. Table 2.1

Table 2.1: Model parameters of the prototyped soft robot.

Parameter	**Length** L (mm)	**Outer Dia.** D_o (mm)	**Inner Dia.** D_i (mm)	**2MR Constants** c_{01} (kPa)	c_{10} (kPa)	**Density** ρ ($\frac{g}{cc}$)
	85	12	3.5	277	-209	1.04

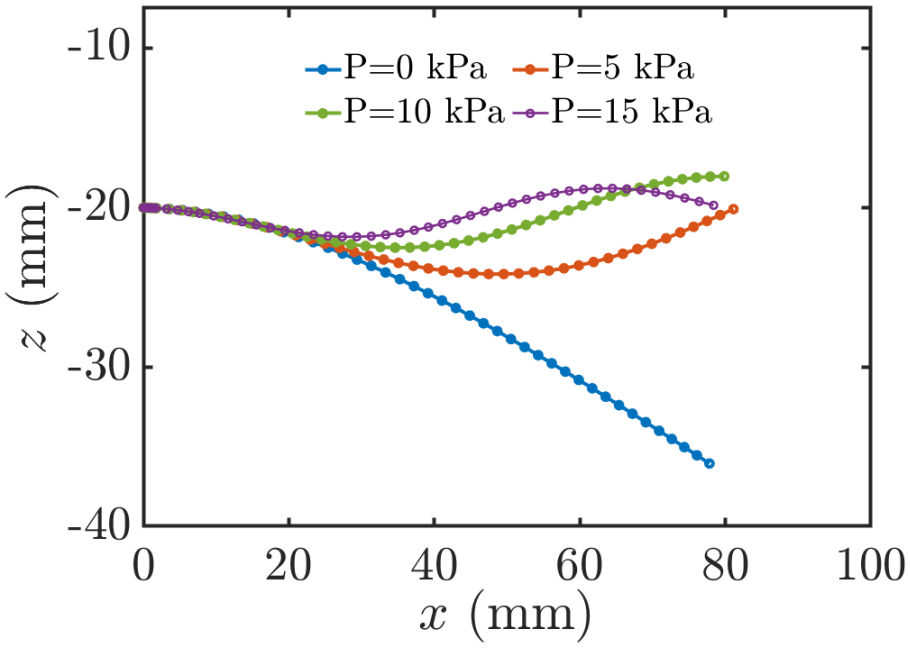

Figure 2.3: Deformation of the soft robot under its weight and a tip force of 30 mN in +z-direction with various chamber pressures.

summarizes the model parameters used in the solution. Also, Figure 2.3 depicts the deformation of the soft robot under its weight and a tip force of 30 mN in +z-direction and various chamber pressures. As depicted, increasing the internal pressure decreased the tip displacement. In other words, it showed that increasing the internal pressure had increased the bending stiffness of the soft robot.

2.2.5 Stiffness Variations

The stiffness of cantilever beams is typically defined as the ratio of the service load (external force) to the maximum deflection. Adopting a similar definition, the stiffness of the modeled soft

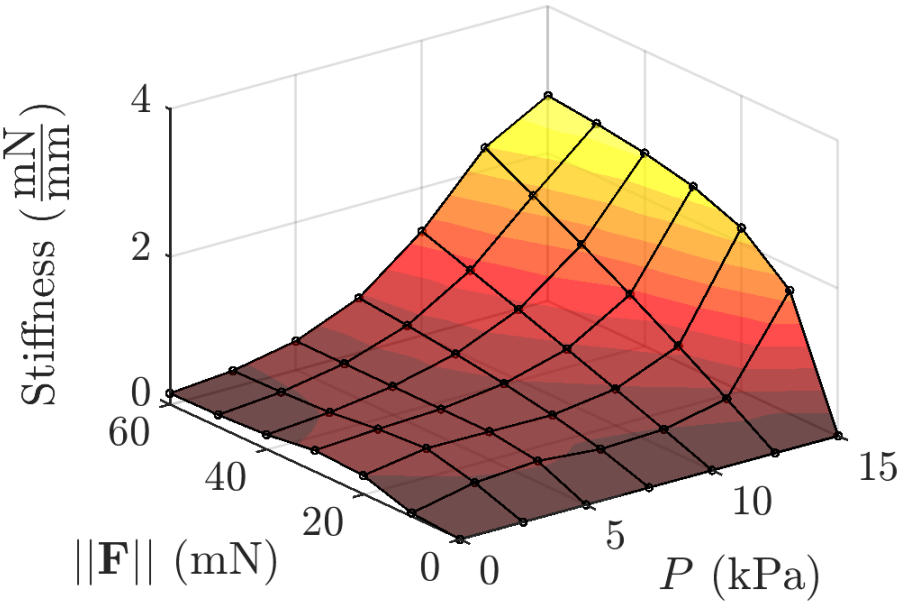

Figure 2.4: Variation of the soft robot's stiffness with internal pressure and tip force.

robot was computed on model results for chamber pressure ranging from $P \in [0, 15]$ kPa and for tip forces (+z-direction) ranging from $||\mathbf{F}|| \in [0, 60]$ mN. Figure 2.4 depicts the variation of the soft robot's stiffness with chamber pressure and tip force. It was observed that the soft robot's stiffness changes both with the internal pressure and tip force. The variation of the stiffness with chamber pressure was deemed as the result of the longitudinal tension caused by the chamber pressure. In addition, because of the hyperelasticity incorporated into the constitutive equation, the tip force would increase the strain thus increasing the bulk moduli.

2.3 Validation Study

2.3.1 Study Design

Four individual experiments were performed for the validation study, i.e., with chamber pressures of 0, 4, 12, and 20 kPa. With each chamber pressure, the tip of the soft robot was pulled upward from the resting position while the force/torque sensor recorded the base reaction forces and torques. In parallel, a camera tracked the tip position of the soft robot for validation comparison. Using the recorded force/torque data the developed model was solved and the tip computed tip

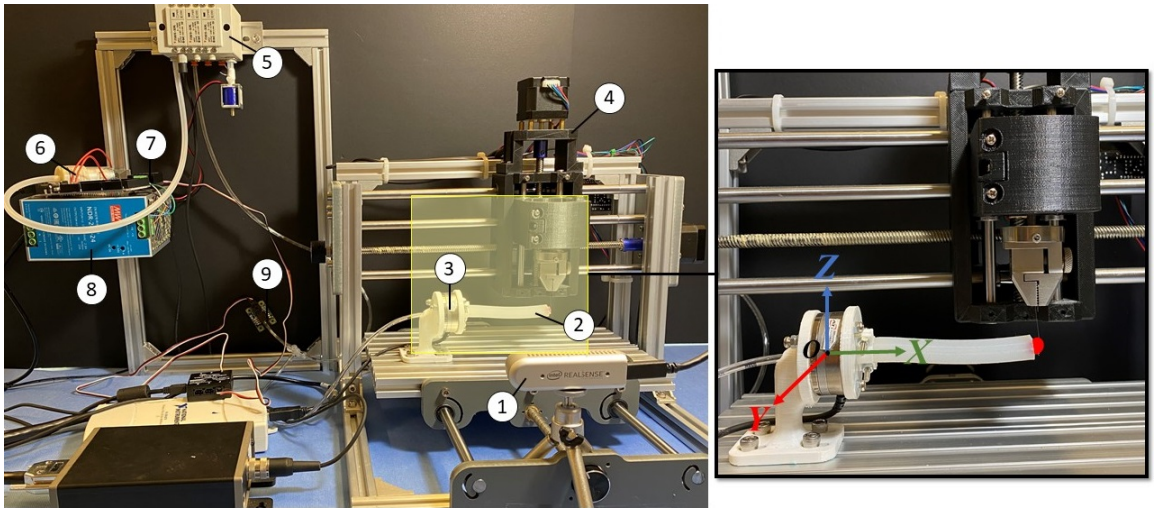

Figure 2.5: Components of the mechanical and electrical modules in the prototyped soft robot (1) 3D-camera (2) soft robot (3) F/T sensor (4) 3-axis CNC machine (5) electronic pressure controller and manifold (6) air pump (7) 12-bit analog voltage generator (8) power supply (9) air pressure sensor.

positions were compared with the ground truth.

2.3.2 Soft Robot Prototype and Experimental Setup

For the fabrication, a cylindrical mold was rapid-prototyped with a 3D printer (Replicator+, MakerBot, NY, USA) using PLA material. Ecoflex™00-50 (Smooth-On Inc., PA, USA) was used to make the body of the soft robot. Also, a platform housing was 3D-printed to install the soft robot's based on the force/torque sensor. The silicone mixture was degassed in a vacuum chamber and rested for 24 hours at 24°C for curing. Figure 2.5 shows the experimental setup for this study. A 6-DOF force/torque sensor (ATI Industrial Automation, F/T Sensor: Mini40) was used to measure the soft robot's base reaction force and torques. An air pump (KPM27C, DC 6V, Koge Electronics) supplied the air pressure and a pressure sensor (Phidgets Inc., AB, Canada) was utilized to record the chamber's real-time pressure during the experiment. Also, an electronic pressure regulator (ITV0010-3UML, SMC, Tokyo, Japan) was used. For tracking of the soft robot's tip, a camera (D435i, Intel Corp., CA, USA) was used.

2.4 Results and Discussion

Figure 2.6 shows representative shapes of the soft robot pulled upward 15 mm with 0 and 20 kPa chamber pressure. Also, Table 2.2 compares the theoretical and experimental results for the tip position for the four experiments. Similar to the simulation results, the stiffness (ratio of force to maximum deflection) It was observed that the model error increased with increasing the chamber pressure. The reason might be related to the cross-sectional expansion of the soft robot which was neglected in the model. Nevertheless, the maximum relative error of the proposed model was 8.7%. This level of error is comparable to other studies in the literature, e.g., [87]. In addition, the post-processing showed that the stiffness of the soft robot increased from 3.4 $\frac{mN}{mm}$ ($P = 0$ kPa) to 5.9 $\frac{mN}{mm}$ ($P = 20$ kPa) indicating a 74% pressure-stiffening effect. These findings confirmed the accuracy of the proposed model to capture the effects of internal pressure on the stiffness of the soft robots.

Table 2.2: Comparison of the model results with experiments.

Pressure	Tip Force	Tip Displacement		Displacement Error		Stiffness
		Model	Reference	Absolute	Relative	
(kPa)	(mN)	(mm)	(mm)	(mm)	(%)	(mN/mm)
0	51	14.4	15	0.6	3.4%	3.4
4	64	14.3	15	0.7	4.7%	4.3
12	73	13.9	15	1.1	7.3%	4.9
20	89	13.7	15	1.3	8.7%	5.9

2.5 Summary

This study proposed, solved, and validated a mechanistic model to capture the effect of chamber pressure on the stiffness of soft pneumatic-driven robots. The developed model was employed to simulate the behavior of the soft robot under different tip force and chamber pressure conditions. Through experimental investigation, we confirmed the accuracy of the proposed model. This

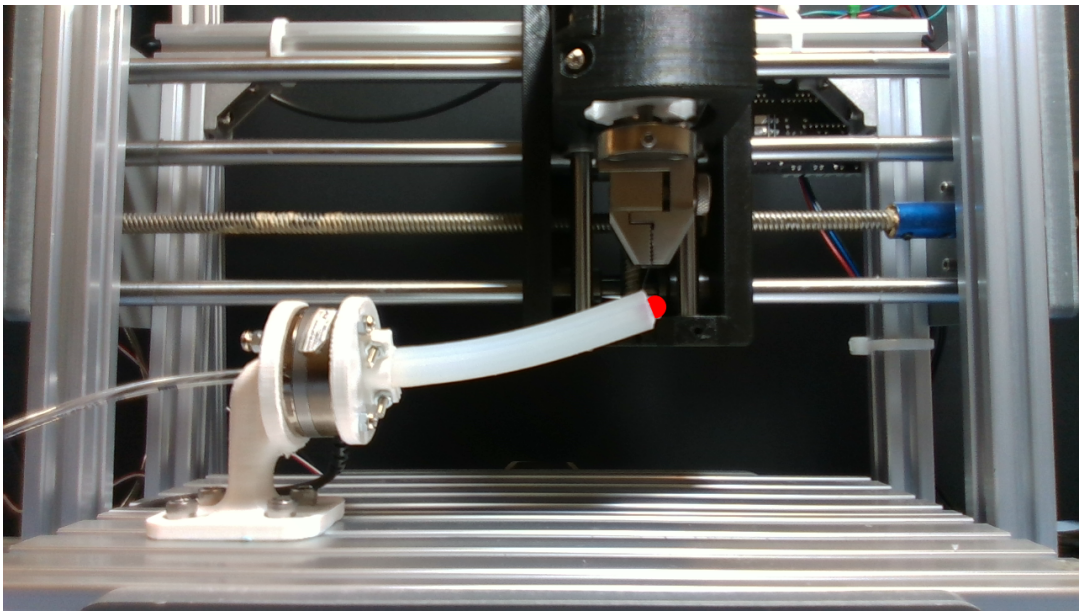

(a)

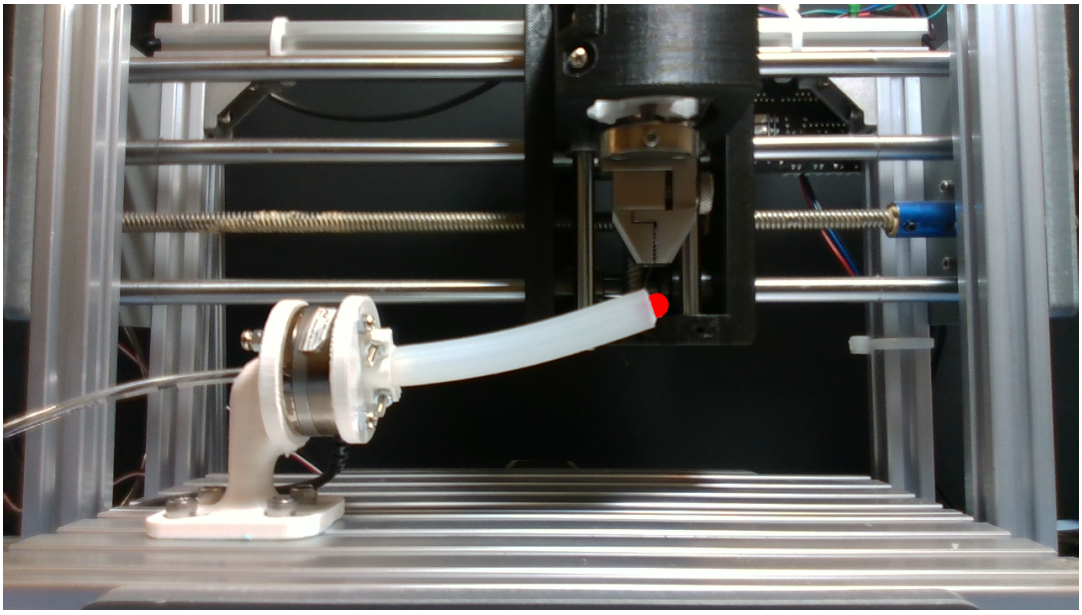

(b)

Figure 2.6: Deformed shape of the catheter with (a) 0 kPa and (b) 20 kPa chamber pressures.

study represents an important initial step towards harnessing the pressure-stiffening phenomenon for stiffness adaptation in soft surgical robots during interventional procedures. By understanding and leveraging the relationship between chamber pressure and robot stiffness, we can enhance the robot's performance and enable more precise and controlled manipulations. As for the next step, the study will investigate the effects of incorporating multiple chambers in the robot design to achieve directional stiffening capabilities. This will enable us to selectively control the robot's stiffness in different directions, offering more versatility in its operations. By further advancing our comprehension of pressure-stiffening phenomena and conducting further exploration in these areas, we aspire to unveil novel possibilities for the advancement of soft robots. These developments aim to provide such robots with enhanced capabilities and improved performance across a multitude of applications, with a specific focus on the field of MIS.

Chapter 3

Stiffness Adaptation of a Hybrid Soft Surgical Robot for Improved Safety in Interventional Surgery

Minimally invasive procedures require the percutaneous insertion of specialized instruments, which are then guided toward the intended anatomical target. While the instruments' low stiffness provides an advantage, enabling safer navigation through the body, they face a significant challenge when force transmission is required upon reaching the target. Constant stiffness inherently limits maneuverability and the capacity for force transmission. On the other hand, highly flexible devices perform well in safely navigating the body but lack the ability to handle heavy payloads. Conversely, highly rigid devices can accommodate relatively high loads but struggle to navigate through complex, convoluted trajectories. To address these limitations, this study proposed an innovative solution: an adaptive stiffness soft robot. This approach aimed to investigate the influence of chamber pressure on the robot's stiffness. A pneumatic soft robot with a single chamber and one tendon was designed and manufactured for this purpose. Subsequently, a continuum mechanics model based on the nonlinear Cosserat rod model, incorporating a hyperelastic material model and accounting for large deformation kinematics, was developed. By employing the shooting method, the model was solved as a BVP with Dirichlet and Neumann BCs. The outcomes of the model demonstrated

the feasibility of stiffness adaptation through simultaneous tendon-driving and pneumatic actuation. To validate the theoretical findings, a series of experimental studies were conducted, varying the pressure within a range of 33 to 44 kPa and the tendon tension within a range of 0 to 2.4 N. The results from both the theoretical and experimental analyses exhibited similar trends in terms of tip displacement and stiffness, with a maximum error of 8.25%. These findings provide empirical support for the theoretical conclusions, lending credibility to the proposed adaptive stiffness soft robot concept.

3.1 Introduction

3.1.1 Background

A meta-analysis of the literature reveals a growing interest in the usability of soft robots in MIS [24]. This increasing interest can be attributed to the natural compliance of the structural materials used in soft robots, such as elastomers, which make them well-suited for interacting with unstructured environments [26] and for medical applications [27]. Various soft robotic MIS systems have been proposed for different medical procedures, including cardiovascular interventions [80], endoscopy [43], drug delivery [81], and general surgery [82]. To illustrate this, Figure 3.1 depicts a soft surgical robot being used for intra-cardiac interventions as a representative case. However, a dilemma exists concerning the performance of soft robots within the context of medical devices [70]. On one hand, their low stiffness is advantageous for navigation purposes. On the other hand, when soft robots reach the target site, they are required to perform specific tasks such as ablation [13], which necessitates effective force transmission to the body tissue. The force transmission capacity is directly influenced by the stiffness of the soft robot. Consequently, there exists a trade-off between the deformability and force transmission capacity of soft robots in minimally invasive interventions.

The lack of adaptivity in current instruments can result in oversteering and vessel rupture [9]. Extensive studies have demonstrated a significant risk of embolization, perforation, and thrombosis associated with excessive contact force between the catheter and the vascular wall [22]. In situations where rigid instruments are ineffective or unable to reach the surgical site, soft instruments

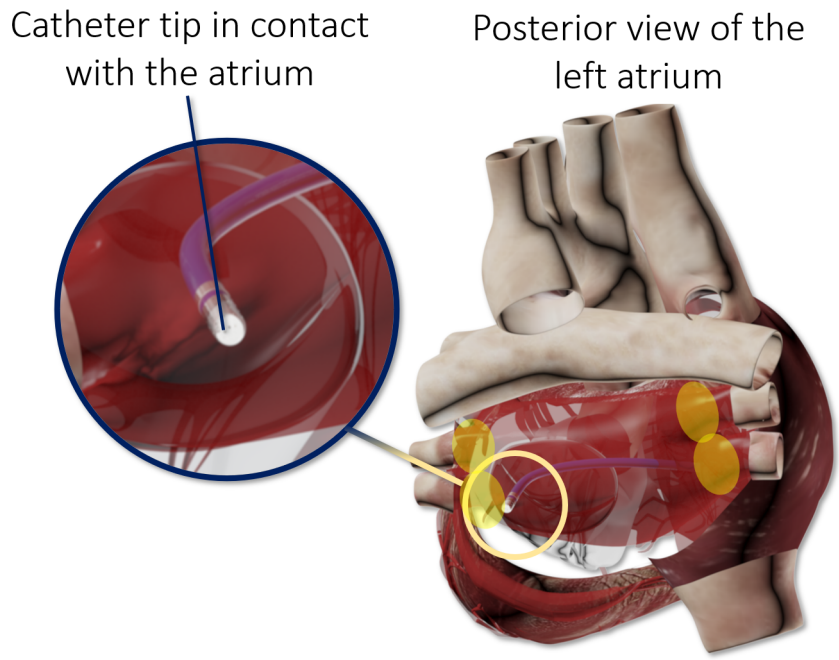

Figure 3.1: Soft surgical robot for intra-cardiac interventions [13].

are employed. However, if soft devices also prove ineffective, open surgery remains the only viable option. Current research focuses on enhancing the usability of soft robots in minimally invasive interventions by combining the precise controllability of rigid robots, the accessibility of soft instruments, and the safety provided by soft materials to address existing limitations. Overcoming the challenges faced by current MIS instruments necessitates the development of compliant, variable stiffness, and safe new instruments [23].

Nevertheless, the majority of currently proposed soft MIS robots exhibit constant stiffness due to their material properties and structural design [13]. For instance, in tendon-driven catheters, which are widely used in steerable catheters, the backbone typically consists of super-elastic nitinol (NiTi) alloy. While a highly flexible robot can be maneuvered safely through orifices, it may lack sufficient force capacity. Conversely, a highly rigid device can exert relatively high force but may struggle to navigate highly tortuous trajectories. Therefore, the clinical value of a soft robot with controllable stiffness (enabling intraoperative adaptability) cannot be overstated. Such a soft robot facilitates the development of control frameworks for semi-autonomous stiffness modulation, enhancing intraoperative adaptation to task-specific requirements such as force capacity [70]. This

study proposes and validates a mechanistic model to examine the influence of chamber pressure on the stiffness of a tendon-driven soft robot. Leveraging these capabilities and addressing the force-flexibility dilemma will contribute to the advancement of next-generation robotic instruments for robot-assisted interventions.

3.1.2 Related Studies

Soft robots, in theory, are continuum robots characterized by possessing infinite DOF. However, one of their primary limitations lies in their diminishing ability to exert force along their length [3]. To facilitate mechanical modeling, the deformation of soft robots has often been simplified using Euler-Bernoulli's beam theory [89]. Nonetheless, experimental findings have demonstrated that the relationship between shape and bending moment exhibits significant nonlinearity [52], rendering Euler-Bernoulli's beam theory invalid. Alternative approaches involve modeling the soft robot as a curve [83, 84, 85] or as a collection of small rigid segments interconnected by flexible joints [86]. Another widely utilized approach in the literature is the PCC model [53].

To account for diverse loading conditions, researchers have proposed considering the soft robot as a one-dimensional slender object, employing the Cosserat rod model [56, 57, 58, 87]. This modeling framework offers several advantages, including the capability to incorporate the effects of gravity, torsion, and external loading. Moreover, the Cosserat rod model enables the unified treatment of small and large deformations of soft robots, simplifying the model derivation process. Comparative studies have demonstrated the superiority of this modeling approach over the PCC model, particularly when shear and gravitational loading are taken into account [59].

3.1.3 Contributions

This study aimed to contribute to the field by designing, modeling, and experimentally validating a tendon-driven pneumatically actuated soft robot with controllable stiffness. The primary objective was to demonstrate that such a soft robot exhibits variable stiffness based on different combinations of input mechanical stimuli, specifically air pressure and tendon tension. This variable stiffness enables the soft robot to adjust its deformability and force transmission capacity to

suit various phases of minimally invasive interventional procedures. The feasibility of this hypothesis was initially established in a previous work [70]. Notably, the investigation of stiffness control through hybrid air-tendon actuation remains unexplored in the existing literature pertaining to interventional surgeries.

By controlling the stiffness of the soft robot, its deformability can be increased during the steering phase to navigate safely through complex anatomical sites. Conversely, stiffness can be increased during load-bearing tasks to enhance force transmission. To achieve these objectives, the main contributions of this study were as follows:

(1) Development of a comprehensive model using the Cosserat rod model to accurately describe the deformation of the hybrid-actuated soft robot, taking into account the influences of both driving modalities.

(2) Integration of nonlinear material properties, specifically hyperelasticity, into the Cosserat rod model to capture the behavior of the soft robot's materials.

(3) Validation of the proposed model through experimental verification and comparison with experimental data.

(4) Demonstration of the proof-of-concept for stiffness adaptation by manipulating the chamber pressure in a tendon-driven soft robot.

By addressing these research objectives, this study enhances our understanding of soft robot behavior and contributes to the advancement of adaptive and controllable soft robotic systems for interventional procedures.

3.2 Material and Method

In this section, the material modeling is presented, and subsequently, the kinematics and force balance equations of the soft robot are derived based on the Cosserat rod model. Subsequent to this, the hyperelastic constitutive equations were proposed to establish a relationship between the forces and moments and the kinematic displacements. Following that, the solution schema for the

BVP is introduced, and ultimately, the derivation of stiffness from the tip force and displacement is provided.

3.2.1 Material Modeling

The mechanical responses of silicone rubber were modeled as being nonlinear elastic, isotropic, and incompressible under quasi-static loading. In order to achieve this, the hyperelastic constitutive model of the soft robot was chosen to be the 2MR model. The strain energy density function (W) of the 2MR model was as follows:

$$W = C_{10}(I_1 - 3) + C_{01}(I_2 - 3) \tag{20}$$

where I_1 and I_2 are the deviatoric strains invariant and C_{10} and C_{01} are material constants. To find the material constants, L. Marechal et al. [90] performed a series of uniaxial tensile tests based on the ASTM D412 standard [91] for different kinds of silicone rubbers used for prototyping the soft robots in this study. Table 3.1 shows the values for the material constants.

3.2.2 Geometrical Design

One of the primary concerns associated with the utilization of soft robots in MIS applications was the ballooning effect observed during pneumatic actuation, as noted by Hoeg et al. [92]. This effect manifested in the form of excessive ballooning, which could result in the exertion of high local forces on tissue organs or even lead to the rupture of the soft robot. Furthermore, the ballooning effect caused a wastage of energy through radial expansion, while the desired expansion direction for effective operation was longitudinal.

In this study, a soft robot constructed from Ecoflex 0050 and featuring a central chamber was devised, drawing upon the recommendations provided by Y. Elsayed et al. [47]. Their research suggests that the ratio of the chamber length (L^{ch}) to the length of the soft robot (L) should ideally be approximately 0.85. Furthermore, to mitigate the ballooning effect, the ratio of the chamber area ($\mathbf{A}^{ch}$) to the cross-sectional area of the soft robot ($\mathbf{A}$) should be around 0.04. Adhering to these guidelines, a soft robot with an external diameter of 15 mm and a length of 75 mm was

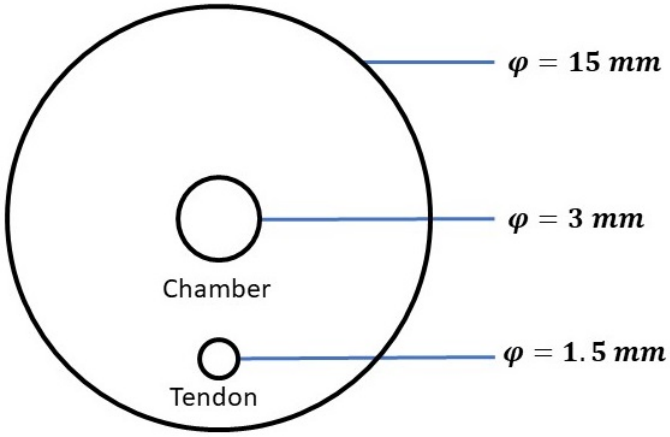

Figure 3.2: Cross-section of the soft robot with the central chamber for air pressure and a passage for the tendon.

conceptualized. This design encompassed a chamber diameter of 3 mm, a chamber length of 65 mm, and tendon passages with a diameter of 1.5 mm. Figure 3.2 illustrates the cross-section of the soft robot, featuring the central chamber, in response to pneumatic pressure.

3.2.3 Mechanistic Modeling

Kinematics

The soft robot in question has been conceptualized as a slender elastic object [93], and its behavior has been mathematically formulated using a set of differential equations rooted in Cosserat rod theory [87]. For the purpose of analysis, it was posited that the tension along the length of the tendon remained constant, and the position of the tendon relative to the cross-section of the soft robot remained unchanged throughout the deformation. Additionally, the 2MR material model was employed as a representative to maintain general applicability. Notably, the viscoelastic properties of the soft robot, such as creep, relaxation, and rate-dependency, were disregarded. Finally, it was assumed that the internal chamber pressure did not significantly deform the cross-sectional area.

Figure 3.3 illustrated a hollow soft robot in its initial configuration, exhibiting a cross-sectional area denoted as A. This robot experienced an internal pressure denoted as P, along with a tendon force $\mathbf{F}$ applied at its tip. Additionally, the soft robot encountered a distributed gravitational force (weight). The backbone of the robot was characterized by points parameterized through an arc

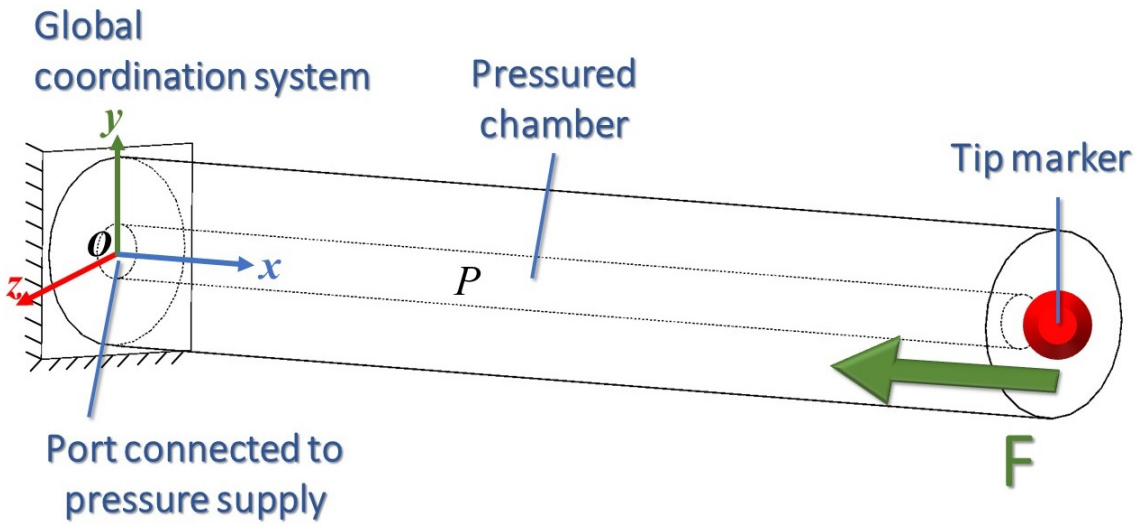

Figure 3.3: Schematic initial shape of the soft robot with internal pressure P and a tendon force $\mathbf{F}$.

parameter $s \in [0, L]$ (representing the reference arc length parameter). Here, L denoted the original length of the rod, while each point on the backbone possessed a locally orthonormal frame denoted as $\mathbf{R}(s)$ [53]. The position of any given point on the backbone of the soft robot, relative to the base of the arc at a distance s, was defined using the position vector $\mathbf{p}(s)$.

With the presented shape parameterization, the extension, and shear strains along the backbone, $\mathbf{v}(s)$ (the partial derivative of $\mathbf{p}$ over the arclength in the local frame), are [87]:

$$\mathbf{v}(s) = \mathbf{R}^T(s)\frac{\partial \mathbf{p}(s)}{\partial s} \tag{21}$$

while partial derivative of $\mathbf{R}$ over the arclength in the local frame is a term for the curvature, $\mathbf{u}(s)$, (bending and torsion strains) [87]:

$$\mathbf{u}(s) = \left(\mathbf{R}^T(s)\frac{\partial \mathbf{R}(s)}{\partial s}\right)^{\vee} \tag{22}$$

where $(.)^{\vee}$ is the vee-operator, a mapping for $\mathfrak{so}(3)$ to $\mathbb{R}^3$ [88]. The kinematic equations relate the internal strains throughout the length of the robot to its parameterized shape.

Conservation of Momentum

From the mechanical point of view, the pressure of chamber causes a constant longitudinal tensile force along the soft robot's length with a magnitude of PA, where A is the cross-sectional area of the robot perpendicular to its backbone. It is noteworthy that the internal pressure has symmetry about the longitudinal axis of the soft robot; therefore, it does not affect the force distribution in the perpendicular planes to the longitudinal axis [70]. The quasi-static balance equations of the soft robot were obtained by using the Cosserat rod theory as [87]:

$$\frac{\partial \mathbf{p}(s)}{\partial s} = \mathbf{R}(s)\mathbf{v}(s) \tag{23}$$

$$\frac{\partial \mathbf{R}(s)}{\partial s} = \mathbf{R}(s)(\mathbf{u}(s))^{\wedge} \tag{24}$$

$$\frac{\partial \mathbf{n}(s)}{\partial s} = -\rho A\mathbf{g} - PA\hat{\mathbf{e}}_1 - \mathbf{F} \tag{25}$$

$$\frac{\partial \mathbf{m}(s)}{\partial s} = -\left(\frac{\partial \mathbf{p}(s)}{\partial s}\right)^{\wedge}\mathbf{n}(s) - \mathbf{r}\times\mathbf{F} \tag{26}$$

where $\mathbf{n}(s)$ and $\mathbf{m}(s)$ are the internal force and moment vectors in the global coordination system, ρ is the mass density (constant), A is the cross-sectional area of the soft robot, $\mathbf{g}$ is the gravity vector, $\mathbf{r}$ is the tendon's offset from the cross-section, and $(.)^{\wedge}$ is the hat-operator, a mapping from $\mathbb{R}^3$ to $\mathfrak{so}(3)$ [88]. In fact, (21–26) describe the nonlinear state-space representation of the soft robot's mechanics with six state variables, i.e., $\begin{pmatrix}\mathbf{v}(s) & \mathbf{u}(s) & \mathbf{p}(s) & \mathbf{R}(s) & \mathbf{n}(s) & \mathbf{m}(s)\end{pmatrix}$.

Constitutive Equations

The quasi-statics system governed by (21–26) have independent variables $\mathbf{v}(s)$ and $\mathbf{u}(s)$. So, a material constitutive law should be used to relate them with internal forces. Linear elasticity theory, large strain theory, and visco-hyperviscoelastic assumptions are popular material constitutive laws [94]. Any combination of the Cosserat rod model, as the mechanical model, and the above constitutive laws results in a set of differential equations governing the quasi-statics response of the system. Generally, large strain theory is used for modeling the behavior of hyperelastic materials [94]. In this case, the mechanical properties of hyperelastic materials changes with local stretches, however for a given stretch (at any s), the tangent moduli $\mathbf{K}_{se}$ and $\mathbf{K}_{bt}$ represent the mechanical

stiffness for unit length in shear and elongation momentarily. The "se" subscript refers to shear and extension, and "bt" refers to bending and torsion. To calculate the tangent moduli, first, a 2MR constitutive model for the material behavior of the soft robot was assumed. (27) represents the 2MR model for uniaxial elongation:

$$T_{11} = 2\left(C_{10} + C_{01}\lambda^{-1}\right)\left(\lambda^2 - \lambda^{-1}\right) \tag{27}$$

with T_{11} longitudinal nominal stress and λ is the principal stretch. Moreover, the initial shear modulus $G_\circ$ and initial Hooke's modulus $E_\circ$ of 2MR material is obtained by:

$$E_\circ = 2G_\circ(1+\vartheta) \tag{28}$$

$$G_\circ = 2(C_{10} + C_{01}) \tag{29}$$

with ϑ as the Poisson's ratio that is ≈ 0.5 for near-incompressible elastomers. During the deformation, the tangent elastic modulus of the soft robot's can be estimated using the strain energy density function. Based on the Cosserat rod model, the basic linear elastic constitutive equations are [87]:

$$\mathbf{n}(s) = \mathbf{R}(s)\mathbf{K}_{se}\Big(\mathbf{v}(s) - \mathbf{v}^\star(s)\Big) \tag{30}$$

$$\mathbf{m}(s) = \mathbf{R}(s)\mathbf{K}_{bt}\Big(\mathbf{u}(s) - \mathbf{u}^\star(s)\Big) \tag{31}$$

where, $(.)^\star$ refers to the state variables before deformation (initial state). Assuming, an initially straight soft robot extended along the global $x-$axis, $\mathbf{v}^\star(s) = \begin{pmatrix} 1 & 0 & 0 \end{pmatrix}^T$ and $\mathbf{u}^\star(s) = \mathbf{0}$. Also, substituting the derived shear and Hooke's moduli the tangent stiffness matrices were obtained as:

$$\mathbf{K}_{se} = \text{diag}\begin{pmatrix} G\mathbf{A} & G\mathbf{A} & E\mathbf{A} \end{pmatrix} \tag{32}$$

$$\mathbf{K}_{bt} = \text{diag}\begin{pmatrix} EI & EI & 2GI \end{pmatrix} \tag{33}$$

with:

$$G = \frac{\partial T_{11}}{\partial \lambda} \tag{34}$$

where I is the second moment of inertia of the soft robot's cross-section perpendicular to the backbone. $\mathbf{K}_{se}(P)$ and $\mathbf{K}_{bt}(P)$ are determined by the material properties and cross-sectional geometry and are function of P. More specifically, the flexural rigidity EI is affected by chamber pressure. E changes as W changes with pressurization of the chambers due to accumulated strain in the hyperelastic body of the robot. Nevertheless, I remains constant as the effect of pressure on the crossectional geometry is neglected.

Boundary Conditions

Necessary for the solution of the balance equations, the BCs are determined from the physics and structure of the problem. The first set of BCs relate to the kinematic constraints at the base of the soft robot, i.e., $s = 0$. From the mechanical point of view, the soft robot is a cantilever, thus:

$$\mathbf{p}\big|_{s=0} = \mathbf{p}_0 \tag{35}$$

$$\mathbf{R}\big|_{s=0} = I_{3\times 3} \tag{36}$$

where $\mathbf{p}_0$ is the position of the backbone at $s = 0$ before the deformation. These BCs translate into six independent scalar kinematic constraints. Also, it is assumed that the tendon is terminated at the distal end of the soft robot, i.e., $s = L$, and the tendon tension is applied tangent to the extension direction of the soft robot, i.e., local $x-$direction, thus:

$$\mathbf{n}\big|_{s=L} = \mathbf{R}\big(PA\big|_{s=L} - \mathbf{F}\big|_{s=L}\big) \tag{37}$$

$$\mathbf{m}\big|_{s=L} = \mathbf{R}\big(-\mathbf{r}\times\mathbf{F}\big|_{s=L}\big) \tag{38}$$

these sets of BCs represent six independent BCs that must be fulfilled with the solution. The BCs indicate certain constraints to be satisfied by the solution at both ends of the soft robot. From a mathematical point of view, such conditions constitute a BVP.

Table 3.1: Model parameters of the prototyped soft robot.

Length L (mm)	**Outer Dia.** D_o (mm)	**Inner Dia.** D_i (mm)	**2MR Constants [90]** c_{01} (kPa)	c_{10} (kPa)	**Density** ρ ($\frac{g}{cc}$)	**Tendon offset** r (mm)
75	15	3	35.3	-105	1.112	5

Solution Schema

In order to find the deformation of the soft robot, the constitutive equations were initially substituted into the force and moment balance equations. It is assumed that we completely know the initial posture of the robot. For the system of nonlinear differential equations (21–26), there are two BCs (concerning to **p**, **R**) available at the proximal end and the others (for **n** and **m**) at the distal end. For solving this problem, a shooting method was implemented. Then, the simulation loop starts, and the ODE sets with the corresponding BCs solved iteratively, leading to the visualization of the response. Table 3.1 summarizes the model parameters used in the solution. Also, Figure 3.4 depicts the deformation of the soft robot under its weight and various tendon forces with constant chamber pressures and Figure 3.5 depicts the deformation of the soft robot under its weight without any tip force in various chamber pressures. As depicted, it showed that increasing the internal pressure had increased the bending of the soft robot.

Stiffness Variations

The stiffness of cantilever beams is defined as the ratio of the external force to the maximum deflection. According to this definition, the stiffness of the fabricated soft robot was calculated on simulation results for a range of chamber pressures from 33 to 44 kPa and for tip forces from 0 to 2.4 N. In addition, elastic modulus, and consequently the flexural rigidity EI, are dependent on the chamber pressures. However, in practice, W cannot be measured; thus, indirect measurement is proposed. To this end, the kinematic stiffness of the soft robot is proposed to be measured as the surrogate (indicator) of the flexural rigidity. The kinematic stiffness in this study is defined as:

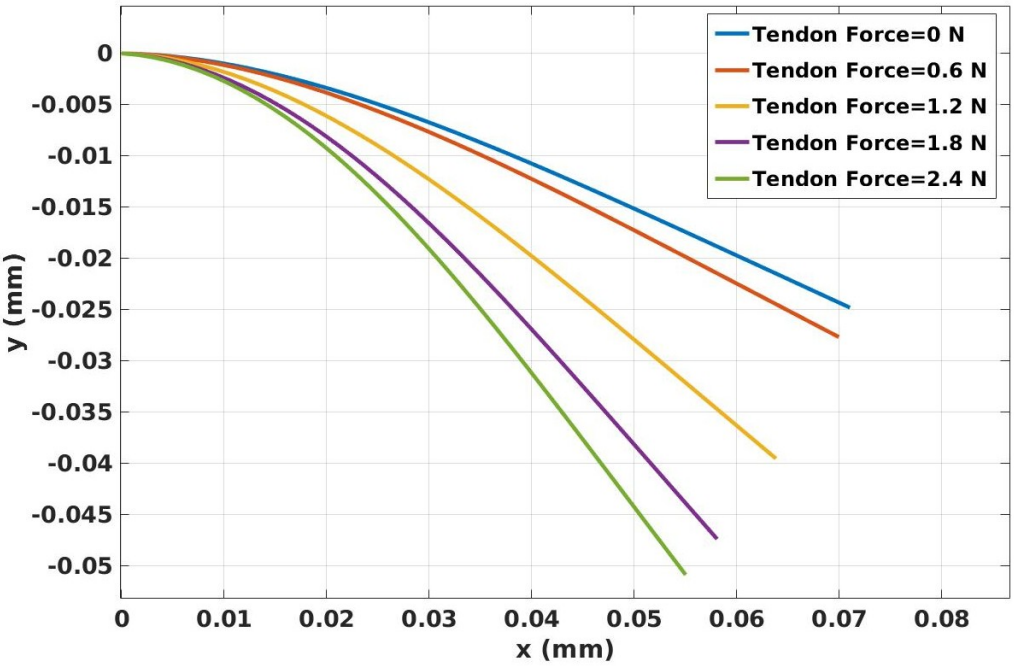

Figure 3.4: Deformation of the soft robot under its weight and various tendon forces with constant chamber pressures.

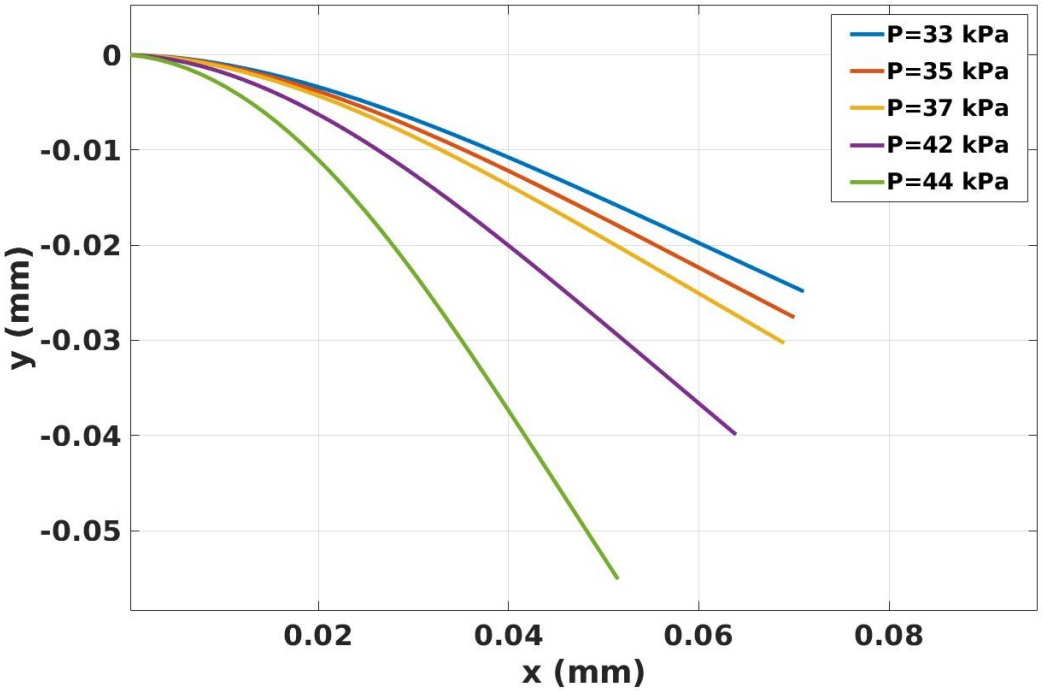

Figure 3.5: Deformation of the soft robot under its weight without any tip force in various chamber pressures.

$$k(P) = \frac{\partial |\mathbf{RF}|}{\partial \left| \mathbf{p}\Big|_{s=L} - \mathbf{p}_0\Big|_{s=L} \right|} \tag{39}$$

As can be seen, the proposed stiffness estimation, (39), requires measurement of tendon forces and tip displacement of the soft robot. The proposed formulation indicates that with a constant tendon force, pressurization of the chambers opposes the tendon force and decreases the robot's tip displacement. This phenomenon increases $k(P)$ through decreasing the denominator in (39). From a constitutive perspective, an increase in the chamber pressure increases the stretch in the soft robot's body and stiffness. For real-time stiffness adaptation, it is proposed to adopt a proportional-derivative-integral (PID) controller to control the pressure inside the chambers such that $k(P)$ remains at the user's desired level. In other words, the tendon drivers would measure the tendon tensions, and the tip displacement would be measured either through the proposed kinematic model (using the tendon lengths) or the use of an external stereo camera. The stiffness would be estimated using these data and (39), while with the PID controller, the internal pressure would change the stiffness, thus the tip displacement of the soft robot. This way, the user can change the robot's stiffness during interventional tasks per the clinical need.

Figure 3.6 depicts the variation of the soft robot's stiffness with chamber pressure and tendon force.

It was observed that the soft robot's stiffness changes both with the internal pressure and tip force. The changes in the stiffness with chamber pressure were considered as the result of the longitudinal tension caused by the chamber pressure. In addition, the tip force would increase the strain because of the hyperelasticity incorporated into the constitutive equations, thus increasing the bulk moduli. On the other hand, the internal pressure in the chamber of a soft robot causes longitudinal and lateral deformation of the body. The deformations also affect the apparent stiffness of the robot by shifting the nonlinear material's strain on its constitutive curve (material stiffness) and by changing the robot's geometry (geometric stiffness) [70].

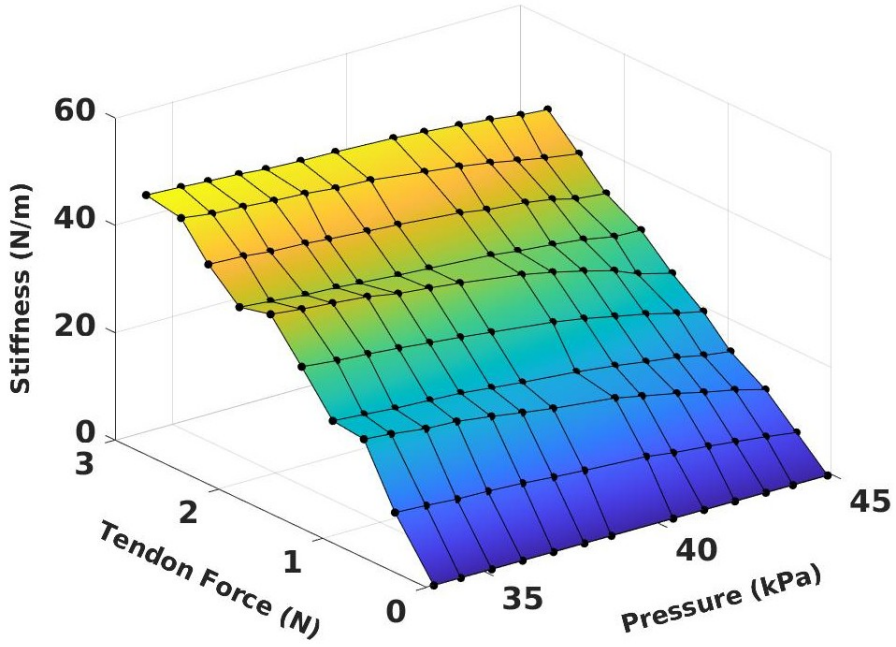

Figure 3.6: Variation of the soft robot's stiffness with internal pressure and tendon force.

3.3 Validation Study

3.3.1 Study Protocol

In this study, 130 individual experiments were performed for the validation study, i.e., with various chamber pressures and various tendon forces. With each tendon force, the internal pressure increased and deformed the soft robot from its resting position. In parallel, a camera saved the tip position of the soft robot for validation comparison. Using the recorded tendon forces data from the motor, the developed model was solved, and the computed tip positions were compared with the ground truth.

3.3.2 Experimental Setup

To fabricate the soft robot, a cylindrical mold with the internal passes for the chamber and tendon was rapid-prototyped with a 3D printer (Replicator+, MakerBot, NY, USA) using PLA material. Also, a platform housing was 3D-printed to install the soft robot's base. Ecoflex™00-50 (Smooth-On Inc., PA, USA) was used to make the body of the soft robot. The silicone mixture was made

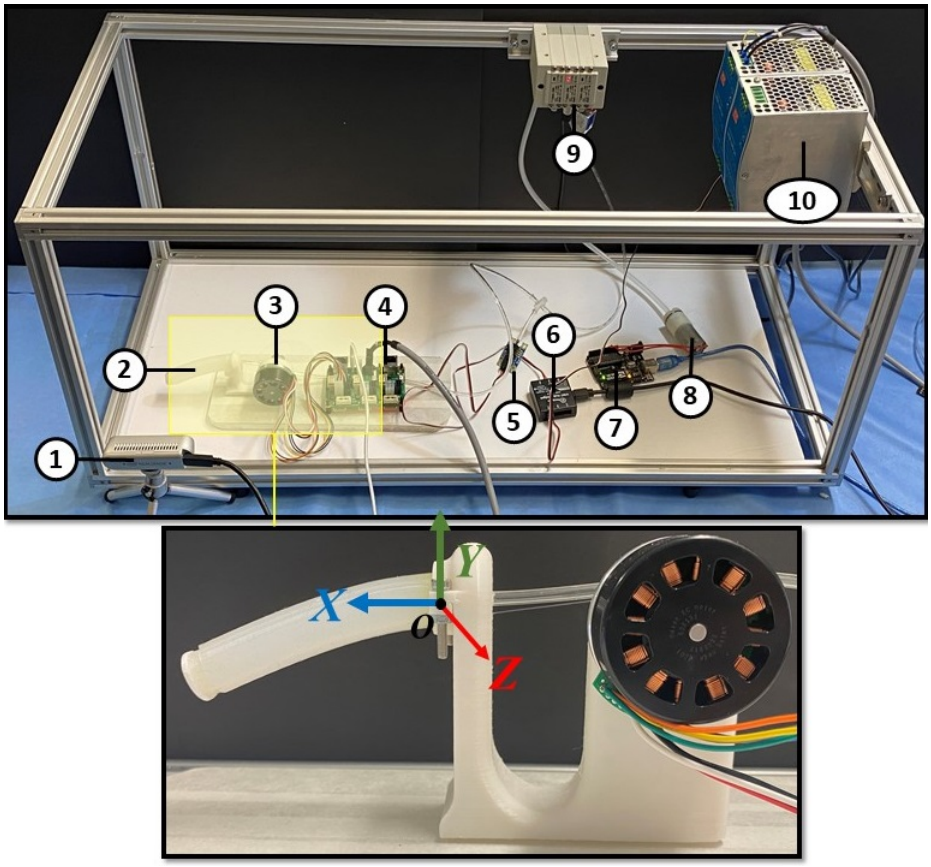

Figure 3.7: Components of the mechanical and electrical modules in the prototyped soft robot (1) camera (2) soft robot (3) motor (4) motor controller (5) air pressure sensor (6) Phidget hub (7) Arduino Uno (8) air pump (9) electronic pressure controller and manifold (10) power supply.

with two parts A and B (50:50) and degassed in a vacuum chamber, and rested for 24 hours at 24°C for curing. Figure 3.7 shows the experimental setup for this study. An air pump (KPM27C, DC 6V, Koge Electronics) supplied the air pressure, and a pressure sensor (Phidgets Inc., AB, Canada) was utilized to record the chamber's real-time pressure during the experiment. Also, an electronic pressure regulator (ITV0010-3UML, SMC, Tokyo, Japan) was used to set the internal pressure of the soft robot. A camera (D435i, Intel Corp., CA, USA) was used to track the soft robot's tip position. In addition, a motor (Maxon, EC 45 flat ϕ 42.8 mm, brushless, 60 W, with Hall sensors) with a digital positioning controller (Maxon, EPOS4 Compact 24/5 EtherCAT 3-axes) was integrated into the setup to provide the tendon force at the tip of the soft robot.

3.4 Results and Discussion

Figure 3.8 shows representative shapes of the soft robot pulled with the tendon force of 0.9 N with 33 and 44 kPa chamber pressure. The results showed that, in accordance with the theoretical findings, with a given tip tension force increasing pressure would have a pressure-softening effect. This phenomenon might be related to the increase of bending deformation with increasing pressure. Also, increasing the tip tension force increases the stiffness with a given chamber pressure. This phenomenon is also in accordance with the strain-stiffening phenomenon of hyperelastic materials. To the best of the authors' knowledge, theoretical and experimental observation of this phenomenon in fully soft robots is not available in the current literature. Moreover, Table 3.2 compares the theoretical and experimental results for the tip position for the 12 experiments. Based on the experimental observations, the maximum absolute difference between the experimental findings and theoretical predictions was 4.88 mm (6.5% of length). The average absolute discrepancy between the experiment and theory was 2.01 mm. The reason for the elevation of error with increasing pressure might be related to non-negligible cross-sectional deformation of the catheter at high pressures that have not been accounted for in the mechanical model. Thus, one of the future improvements of the model could be to incorporate the pressure-dependent cross-sectional deformation of the catheter into the mechanical model. In this study, the extreme values for the pressure were investigated to study the worst-case scenarios. Nevertheless, thanks to the type of pressure regulators used in this study, the continuous adaptation of the pressure is possible and will be performed in future studies. Moreover, the observed high accuracy of the theoretical model allows for generating a large dataset of the control states, i.e., tendon tensions, chamber pressure, and the rate of change of those, to develop a learning-based real-time controller for stiffness adaptation.

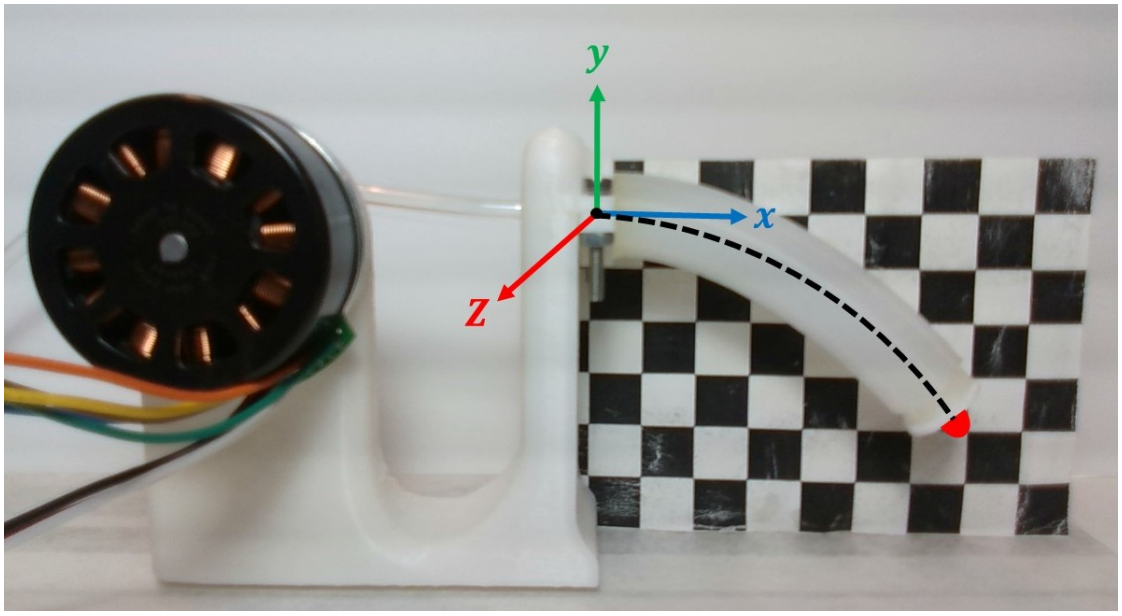

(a)

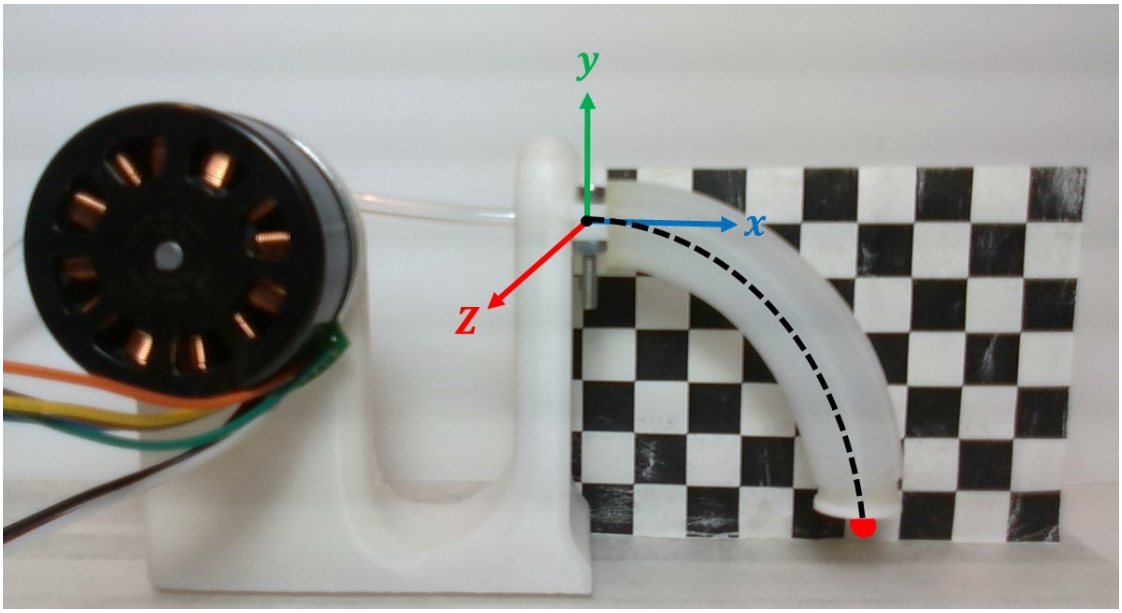

(b)

Figure 3.8: Deformed shape of the soft robot pulled with the tendon force of 0.9 N and (a) 33 kPa, (b) 44 kPa chamber pressure.

Table 3.2: Model and experiments results comparison.

Pressure	Tip Force	Tip Displacement		Displacement Error	
		Model	Reference	Absolute	Relative
(kPa)	(N)	(mm)	(mm)	(mm)	(%)
33	0	24.83	24.90	0.07	0.28%
37	0	28.66	29.27	0.61	2.08%
40	0	31.74	34.18	2.44	7.13%
43	0	40.62	44.18	3.56	8.05%
33	0.9	39.36	39.45	0.09	0.22%
37	0.9	41.59	42.18	0.59	1.39%
40	0.9	43.34	46.72	3.38	7.23%
43	0.9	49.31	53.63	4.32	8.05%
33	1.8	50.25	50.36	0.11	0.21%
37	1.8	52.27	52.91	0.64	1.20%
40	1.8	53.16	56.63	3.47	6.12%
43	1.8	54.21	59.09	4.88	8.25%
Mean:				2.01	4.19%

3.5 Summary

This study aimed to address one of the primary usability limitations associated with soft robots used in robot-assisted interventions, namely the lack of stiffness adaptation. Furthermore, it represented an endeavor towards the development of next-generation surgical robots capable of task autonomy, whereby the robot adjusts its compliance to fulfill specific tasks such as intraluminal

navigation. In pursuit of this objective, a mechanistic model was proposed, solved, and validated to capture the influence of chamber pressure on the stiffness of soft pneumatic-driven robots for applications in robot-assisted minimally invasive interventions. The proposed mechanistic model of the soft robot was employed to determine the robot's shape under various pressure and tendon tension conditions. Through an experimental study, the accuracy of the proposed model was confirmed. It should be noted that the solution obtained from this model is incremental, thereby making it suitable for real-time applications. Future work will involve the presence of multiple chambers for directional stiffening will be examined, along with the feasibility of position-stiffness hybrid control through tendon-pneumatic actuation. These investigations will significantly enhance the state-of-the-art in soft surgical robots by introducing a new capability for intraoperative adaptability.

Chapter 4

Hyperelastic Modeling and Validation of Hybrid-Actuated Soft Robot with Pressure-Stiffening

Soft robots have garnered significant attention in recent years, particularly in intraluminal applications, due to their inherent safety in surgical interventions compared to flexures featuring rigid backbones. This research study focused on investigating a pressure-regulating stiffness tendon-driven soft robot and developing a continuum mechanics model to enable its utilization in adaptive stiffness applications. To achieve this objective, a central single-chamber pneumatic and tri-tendon-driven soft robot was initially designed and fabricated. Subsequently, the classical Cosserat's rod model was employed and enhanced with a hyperelastic material model. The resulting model was then formulated as a BVP and solved implementing the shooting method. In order to investigate the pressure-stiffening effect, a parameter-identification problem was formulated to establish the correlation between the flexural rigidity of the soft robot and its internal pressure. The flexural rigidity of the robot was optimized at different pressures to align with the anticipated deformations based on theoretical calculations and experimental observations. Subsequently, the theoretical predictions for arbitrary pressures were compared against experimental results for validation purposes. The internal chamber pressure ranged from 0 to 40 kPa, while the tendon tensions spanned from 0 to 3

N. The theoretical and experimental outcomes exhibited a reasonable level of agreement in terms of tip displacement, with a maximum error of 6.40% of the flexure's length.

4.1 Introduction

4.1.1 Background

Soft robots have gained significant prominence in the field of MIS [95]. This can be attributed to their utilization of flexible and compliant structural materials, particularly elastomers, which enable them more suitable for interactions with the human body and minimize the likelihood of injury to surrounding tissue during surgical interventions. The inherent characteristics of soft robots make them highly compatible with human-robot interaction and well-suited for executing procedures via natural orifices or small surgical incisions [96].

Furthermore, the integration of soft sensors within soft robots enables the provision of valuable feedback regarding the surgical environment, consequently enhancing surgical precision [75, 77, 79]. Consequently, the application of soft robot-assisted MIS systems has been proposed for diverse medical procedures, including ablation [13], cardiovascular interventions [9], and bronchoscopy [97]. A representative use case demonstrating the utilization of a soft surgical robot for intra-bronchial interventions is illustrated in Figure 4.1. In such instances, a soft robot can adeptly navigate the intricate and narrow airways of the lungs to conduct diagnostic and therapeutic procedures such as biopsy and tumor removal. The compliant and flexible structure of the soft robot enables it to adapt to the dynamic anatomy of the airways, minimizing the risk of tissue damage and thereby enhancing patient outcomes.

In the field of MIS, studies have demonstrated limitations associated with instruments employing rigid end-effectors [98]. These limitations include a lack of adaptability, resulting in issues such as over-steering and vessel rupture [9]. Multiple reports have indicated that the excessive force exerted by rigid instruments can lead to complications such as embolization, perforation, thrombosis, and dissection of the vascular wall. Consequently, there is a recognized necessity for alternative instruments. As a potential substitute for rigid instruments, soft robots utilizing hybrid actuation methods involving air pressure and tendons have been proposed, particularly in scenarios where

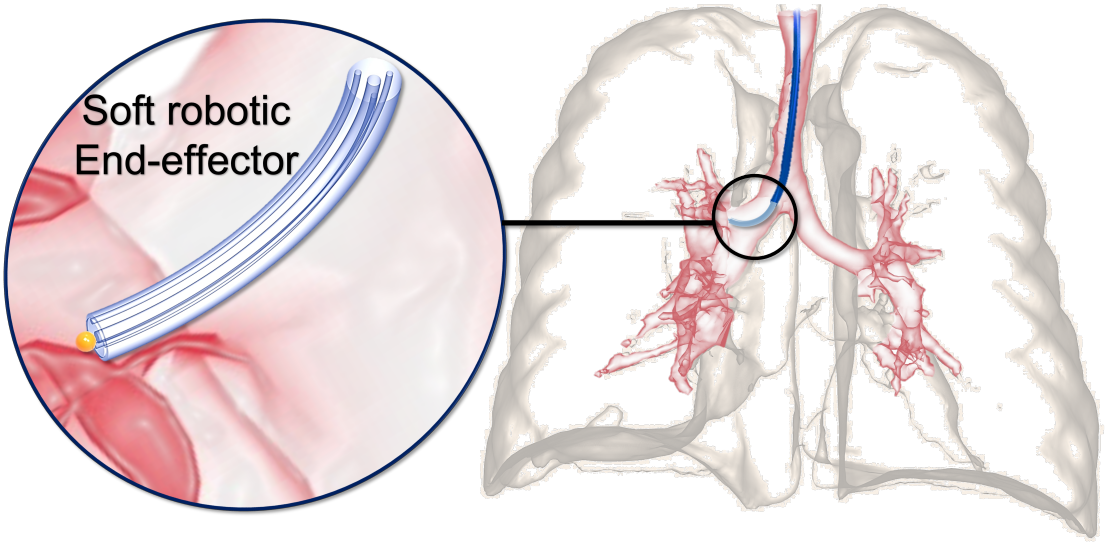

Figure 4.1: A representative use case of soft robots for intraluminal procedures.

rigid instruments fail to complete surgical tasks or access hard-to-reach areas [69, 70]. These soft instruments offer enhanced safety during surgical interventions and can contribute to expedited post-surgery recovery [99]. Diverse researchers have dedicated their efforts to the development of soft surgical instruments, encompassing those equipped with antagonistic actuation [100], stiffness control, and the capability to adapt to the surgical environment, all aimed at improving surgical outcomes.

4.1.2 Related Studies

Soft robots were continuum robots that, in theory, possessed an infinite number of DOF. However, in practice, they were controlled by a limited number of kinematic inputs [2]. It is worth noting that these robots were susceptible to a reduction in their ability to exert force along their length on the environment [3]. To quantify the deformation of soft robots, researchers had employed Euler-Bernoulli's beam theory [101, 102], which simplified the mechanical modeling process. Nevertheless, experimental findings indicated that the relationship between bending moment and deformation exhibited a highly nonlinear behavior, suggesting the inadequacy of this theory under extreme loading conditions of soft robots [52].

Another approach to modeling soft robots was explored by using constant or VC models [103],

including the widely used PCC model [53]. However, these models were found to be inadequate in capturing pressure-stiffening phenomena such as the effect of shear, leading to inaccuracies. While the integration of Finite Element Analysis (FEA) with PCC was shown to enhance the kinematic model of soft robots [104], this approach remained computationally expensive, thereby limiting its practicality for real-time applications.

As an alternative, recent literature has suggested modeling soft robots as one-dimensional slender objects based on the Cosserat rod model [87, 105]. This approach allows for the incorporation of the effects of gravity, torsion, and external loads, while also simplifying the model derivation process [69]. It treats small and large deformations of soft robots with a unified formulation. Research has demonstrated that the Cosserat rod model outperforms the PCC model when shear and gravitational loading are considered [59]. Furthermore, its ability to incorporate hyperelasticity of materials enables accurate tracking of pressure-stiffening phenomena. Table 4.1 summarizes recent research on modeling the multi-physical deformation of soft-actuated robots, highlighting the superiority of the Cosserat rod model in capturing highly nonlinear deformation behavior under various loading conditions. This ability distinguishes it from other models that neglect material nonlinearity, resulting in a more precise representation of the mechanical response of soft robots. For a comprehensive study on the modeling of continuum robots, refer to [106] and [107].

In the present study, a novel mechanistic model based on the Cosserat rod theory was proposed to investigate the impact of tendon forces and pneumatic chamber pressure on the pressure-stiffening phenomenon of a soft robot. The utilization of the Cosserat rod model proves advantageous in depicting the highly nonlinear deformation behavior exhibited by soft robots and facilitates the incorporation of the pressure-stiffening effect through a hyperelastic constitutive model. However, it remains imperative to experimentally characterize and validate this effect to ascertain the model's accuracy. To address this need, the proposed Cosserat rod model underwent validation using a soft robot consisting of three tendons and one central air pressure chamber. The pressure-stiffening phenomenon holds significant relevance in terms of both the functionality and control of soft robots. Therefore, accurately modeling this phenomenon plays a crucial role in advancing the development of sophisticated soft instruments for robot-assisted surgical interventions. The validation of the proposed model against a real soft robot successfully demonstrates its potential in accurately capturing

Table 4.1: Comparison of a representative set of recent literature on mechanical modeling soft robots.

Study	Method	Material Model	Hybrid Actuation	Dynamic	Error (mm)
Roshanfar et al. [69]	Cosserat	Non-Linear	✓	×	8.25%
Hooshiar et al. [105]	Cosserat	Linear	×	×	7%
Wang et al. [108]	Cosserat	Linear	×	✓	-
Dou et al. [109]	Euler-Bernoulli	Linear	✓	×	Less than 8%
Huang et al. [110]	VC	Linear	×	×	2.89%
Niu et al. [111]	Cosserat	Linear	×	×	Less than 4%
Ghoreishi et al. [112]	Euler-Bernoulli	Linear	×	✓	-
Li et al. [113]	Cosserat	Linear	×	✓	Less than 5%
Caasenbrood et al. [114]	PCC	Non-Linear	×	✓	RMS error was ±0.55

the intricate mechanical behavior of soft robots across diverse loading conditions. Furthermore, this study emphasizes the criticality of combining experimental validation with theoretical modeling to ensure the precision and dependability of the proposed model.

4.1.3 Contributions

A pivotal contribution of the conducted study involved the modeling and experimental validation of a tendon-driven pneumatically actuated soft robot, which exhibited a pressure-stiffening effect. This work significantly differed from prior studies by incorporating hyperelastic effects and implementing stiffness adaptation through auxiliary pressure. While previous research primarily focused on modeling and experimentation pertaining to soft robots, our approach significantly advances the comprehension of soft robot behavior under diverse conditions, encompassing their nonlinear material properties. Through the incorporation of hyperelasticity and stiffness adaptation via auxiliary pressure, our model aptly captures the pressure-stiffening effect and adeptly adjusts its flexural rigidity. The soft robot encompasses a range of inputs, including air pressure and tendon tension. Consequently, manipulating the air pressure and tendon tension of the soft robot leads to corresponding changes in its deformability during interventions. To provide further elucidation, the primary contributions of this study were as follows:

(1) A Cosserat rod model was developed to incorporate pressure-stiffening phenomena in a soft robot under both pneumatic and tendon-driven modalities. The model accounted for the tangent elastic modulus as a function of internal pressure.

(2) The hyperelastic constitutive model was integrated into the Cosserat rod framework to ensure accurate representation of material nonlinearity.

(3) The proposed model was experimentally validated to capture the effects of pressure-stiffening during hybrid tendon-pneumatic actuation.

(4) The adaptive flexural rigidity of an inflatable tendon-driven soft robot was predicted by employing a nonlinear constitutive law within a Cosserat rod framework.

This study represents a significant advancement compared to previous research, as it successfully predicted the adaptive flexural rigidity of an inflatable tendon-driven soft robot by incorporating a nonlinear constitutive law into a Cosserat rod framework. While earlier studies primarily focused on modeling and experimentally analyzing soft robots, this study expands the understanding of their behavior by considering their nonlinear material properties. Notably, this study addressed a limitation of prior work where the material property remained constant during inflation by reducing the maximum error through the incorporation of the chamber pressure as a factor influencing the material property. Furthermore, the experimental section of this study comprehensively evaluated the performance of the soft robot in 3D space, which provides a more comprehensive analysis in comparison to previous studies that solely examined two-dimensional (2D) bending. By employing an electromagnetic tracking sensor at the tip of the soft robot, the 3D deformation was captured, in contrast to the previous study that utilized a camera positioned perpendicular to the bending plane to measure the bending angle in 2D.

4.2 Materials and Methods

4.2.1 Mechanistic Modeling

Kinematics

The kinematic equations played a crucial role in comprehending the overall behavior of the soft robot and its response to external stimuli. By determining the internal strains along the robot's length, one could ascertain the required force magnitude to achieve a specific deformation or predict the robot's behavior under particular loading conditions. Soft robots were typically described mathematically using a set of differential equations derived from the nonlinear Cosserat rod theory. These models often portrayed soft robots as flexible and slender objects. However, it is important to note that certain assumptions were made in this study. First, the influence of the robot's internal chamber pressure on the deformation of its cross-sectional area was assumed to be negligible. Additionally, it was assumed that tension forces remained constant along the length of the tendon, and the viscoelastic properties and rate-dependent behaviors (such as creep and relaxation) were

excluded from the 2MR material model. The information presented in this study was derived from relevant research works cited in [70, 115]. Moreover, considering the soft robot's weight, distributed gravitational forces acted upon it. To eliminate the influence of this force on the initial posture of the robot, it was positioned upside down throughout the entirety of the experiment.

Figure 4.2 illustrates a cantilever hollow soft robot in its initial shape, characterized by a cross-sectional area A. The robot is subjected to an internal pressure P and three tendon forces $\mathbf{T}_i$ applied at the tip. Furthermore, Figure 4.3 presents the cross-section of the soft robot, depicting tendons arranged at angular separations of 120° with equal offsets from the center. To describe the soft robot's configuration, each point along its backbone is parameterized using an arc parameter $s \in [0 \;\; L]$, where L represents the initial length of the robot. Additionally, a locally orthonormal frame $\mathbf{R}(s)$ is associated with each point along the backbone [53]. By employing this shape parameterization, it becomes possible to determine the position of any point on the backbone relative to the base of the arc at distance s using the position vector $\mathbf{p}(s)$. The partial derivative of $\mathbf{p}(s)$ with respect to the arc length within the local frame provides the extension and shear strains along the backbone, represented as the strain vector $\mathbf{v}(s)$. These strains can be further classified as the "linear strain" of the soft robot, as defined in [87] as follow:

$$\mathbf{v}(s) = \mathbf{R}^T(s)\frac{\partial \mathbf{p}(s)}{\partial s} \tag{40}$$

The "angular strain" vector, designated as $\mathbf{u}(s)$, was defined as the partial derivative of $\mathbf{R}(s)$ with respect to the arc length in the local frame. This component accounts for the curvature resulting from bending and torsion strains. Specifically, $\mathbf{u}(s)$ characterizes the deformations of the soft robot's backbone in relation to its angular variations along the arc length [87].

$$\mathbf{u}(s) = \left(\mathbf{R}^T(s)\frac{\partial \mathbf{R}(s)}{\partial s}\right)^{\vee} \tag{41}$$

where $(.)^{\vee}$ is the vee-operator, a mapping for $\mathfrak{so}(3)$ to $\mathbb{R}^3$ [88]. The kinematic equations describe the relationship between the internal strains and the overall shape of the soft robot by representing its geometry as a parameterized curve. These equations provide a way to calculate the local curvature and twist of the robot's backbone and the rotation of its cross-section.

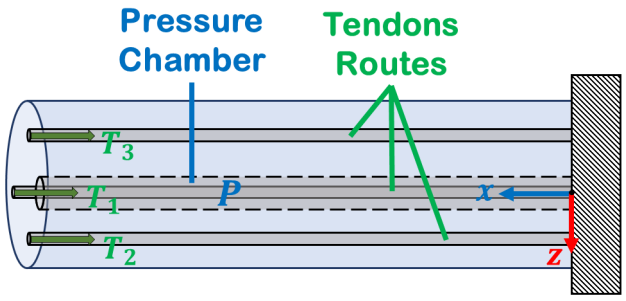

Figure 4.2: Schematic initial shape of the soft robot with central pressure P and three tendon forces $\mathbf{T}_i$.

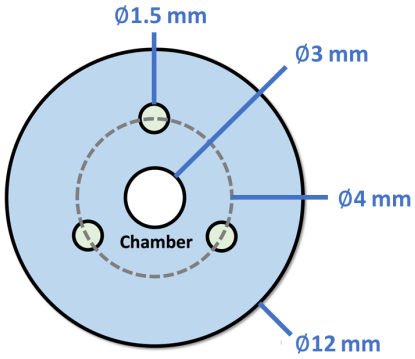

Figure 4.3: Cross-section of the hybrid-actuated soft robot.

Force Balance

The Cosserat rod theory, as presented in [87], was employed to derive the quasi-static balance equations of the soft robot. This was accomplished by eliminating the time derivative from the dynamic equations. The aforementioned assumption can be justified by the low velocity and inertia exhibited by the system during intervention, rendering any temporal variation insignificant. The resulting quasi-static balance equations are expressed as follows:

$$\frac{\partial \mathbf{p}(s)}{\partial s} = \mathbf{R}(s)\mathbf{v}(s) \tag{42}$$

$$\frac{\partial \mathbf{R}(s)}{\partial s} = \mathbf{R}(s)(\mathbf{u}(s))^{\wedge} \tag{43}$$

$$\frac{\partial \mathbf{n}(s)}{\partial s} = -\rho A\mathbf{g} - P\frac{\partial \mathbf{R}}{\partial s}A^{ch}\hat{\mathbf{e}}_1 - \mathbf{T}^t \tag{44}$$

$$\frac{\partial \mathbf{m}(s)}{\partial s} = -\left(\frac{\partial \mathbf{p}(s)}{\partial s}\right)^{\wedge}\mathbf{n}(s) - PA^{ch}\mathbf{R}\left(\mathbf{v}\times\hat{\mathbf{e}}_1\right) - \mathbf{l}^t \tag{45}$$

the internal force and moment vectors in the global coordinate system were denoted as $\mathbf{n}(s)$ and $\mathbf{m}(s)$, respectively. The mass density (assumed constant) was represented by ρ, while A^{ch} referred to the cross-sectional area of the air chamber. The gravity vector was denoted by $\mathbf{g}$, and $\hat{\mathbf{e}}_1$ represented the unit vector. The notation $(.)^\wedge$ corresponded to the hat-operator, which is a mapping from $\mathbb{R}^3$ to $\mathfrak{so}(3)$ [88]. From a mechanical perspective, the chamber pressure exerted a uniform longitudinal tensile force along the entire length of the soft robot. This force had a magnitude of PA, where A denoted the cross-sectional area of the robot perpendicular to its backbone. It is important to note that the internal pressure exhibited symmetry with respect to the longitudinal axis of the robot. Consequently, it did not affect the distribution of forces in planes perpendicular to the axis. Furthermore, the tendon forces and moments were represented by $\mathbf{T}^t$ and $\mathbf{l}^t$, respectively. These quantities were defined in terms of the kinematic parameters of the backbone [94]:

$$\begin{aligned} \mathbf{T}^t &= \mathbf{R}(\mathbf{a} + \mathbf{A}\mathbf{v}_{,s} + \mathbf{G}\mathbf{u}_{,s}) \\ \mathbf{l}^t &= \mathbf{R}(\mathbf{b} + \mathbf{G}^T\mathbf{v}_{,s} + \mathbf{H}\mathbf{u}_{,s}) \end{aligned} \tag{46}$$

in which:

$$\begin{aligned} \mathbf{a} &= \sum_{i=1}^{m} \mathbf{a}_i, \quad \mathbf{a}_i = \mathbf{A}_i[\widehat{\mathbf{u}}(\mathbf{p}^b_{i,s} + \mathbf{r}^t_{i,s}) + \mathbf{r}^t_{i,ss}] \\ \mathbf{b} &= \sum_{i=1}^{m} \mathbf{b}_i, \quad \mathbf{b}_i = \widehat{\mathbf{r}}^t_i \mathbf{a}_i \\ \mathbf{A} &= \sum_{i=1}^{m} \mathbf{A}_i, \quad \mathbf{A}_i = -\tau_i \frac{\left((\mathbf{p}^b_{i,s})^\wedge\right)^2}{\|\mathbf{p}^b_{i,s}\|^3} \\ \mathbf{G} &= \sum_{i=1}^{m} \mathbf{G}_i, \quad \mathbf{G}_i = -\mathbf{A}_i \widehat{\mathbf{r}}^t_i \\ \mathbf{H} &= \sum_{i=1}^{m} \widehat{\mathbf{r}}^t_i \mathbf{G}_i \\ \mathbf{p}^b_{i,s} &= \widehat{\mathbf{u}}\mathbf{r}^t_i + \mathbf{r}^t_{i,s} + \mathbf{v} \end{aligned} \tag{47}$$

where $\mathbf{r}^t$ is the tendon's offset from the cross-section, $\mathbf{p}^b$ is the representation of $\mathbf{p}$ in the local frame (i.e., $\mathbf{p}^b = \mathbf{R}^T\mathbf{p}$), and τ_i is the tendon tension. (40)–(45) describe the nonlinear state-space representation of the soft robot's mechanics with six state variables: $\begin{pmatrix} \mathbf{v}(s) & \mathbf{u}(s) & \mathbf{p}(s) & \mathbf{R}(s) & \mathbf{n}(s) & \mathbf{m}(s) \end{pmatrix}$.

The quasi-statics system, governed by (40)–(45), had independent variables $\mathbf{v}(s)$ and $\mathbf{u}(s)$. Consequently, establishing a relationship between the external forces acting on the soft robot and its

internal loading necessitated the implementation of a material constitutive law. Among the most widely utilized material constitutive laws is linear elasticity theory. By incorporating the Cosserat rod model, which serves as the mechanical model, with the appropriate constitutive laws, a set of differential equations could be derived to govern the quasi-static response of the system. Typically, hyperelastic materials exhibit alterations in their mechanical characteristics when subjected to local stretches. Nevertheless, at a specific stretch value at any given s, the tangent moduli $\mathbf{K}_{se}$ and $\mathbf{K}_{bt}$ describe the mechanical stiffness per unit length. The subscript "se" denotes shear and extension, while "bt" refers to bending and torsion. During deformation, the tangent elastic modulus of the soft robots could be estimated by employing the strain energy density function W, which will be defined in the subsequent section. The fundamental linear elastic constitutive equations are outlined in [87].

$$\mathbf{n}(s) = \mathbf{R}(s)\mathbf{K}_{se}\Big(\mathbf{v}(s) - \mathbf{v}^{\star}(s)\Big) \tag{48}$$

$$\mathbf{m}(s) = \mathbf{R}(s)\mathbf{K}_{bt}\Big(\mathbf{u}(s) - \mathbf{u}^{\star}(s)\Big) \tag{49}$$

where $(.)^{\star}$ refers to the state variables before deformation (initial state). Assuming, an initially straight soft robot extended along the global $x-$axis, $\mathbf{v}^{\star}(s) = \begin{pmatrix} 1 & 0 & 0 \end{pmatrix}^{T}$ and $\mathbf{u}^{\star}(s) = \mathbf{0}$. Additionally, substituting the derived shear and Hooke's moduli, the tangent stiffness matrices were obtained as:

$$\mathbf{K}_{se} = \text{diag}\begin{pmatrix} E(P)A_{\circ} & G(P)A_{\circ} & G(P)A_{\circ} \end{pmatrix} \tag{50}$$

$$\mathbf{K}_{bt} = \text{diag}\begin{pmatrix} G(P)I_{11} & E(P)I_{22} & E(P)I_{33} \end{pmatrix} \tag{51}$$

with I_{ii} denoting the second moment of inertia about the $i = 1,2,3$ normal bases of the local coordinate systems along the robot, E is Young's modulus which relates to P, G is the shear modulus, and $A_{\circ}$ the undeformed cross-sectional area of the soft robot.

4.2.2 Constitutive Model

The mechanical behavior of silicone rubber under quasi-static loading conditions was characterized using a nonlinear elastic model that incorporates isotropic and incompressible properties. In this context, the Poisson's ratio (ϑ) was approximately 0.5, as near-incompressible elastomers tend to exhibit such behavior. To accurately represent the hyperelastic constitutive response of the soft robot, a 2MR model was employed. In accordance with the 2MR model, the strain energy density function (W) was formulated as follows:

$$W = C_{10}(I_1 - 3) + C_{01}(I_2 - 3) \tag{52}$$

where C_{10} and C_{01} are material constants and I_1 and I_2 are the stretch invariants as:

$$\begin{aligned} I_1 &= \lambda_1^2 + \lambda_2^2 + \lambda_3^2 \\ I_2 &= \lambda_1^2\lambda_2^2 + \lambda_2^2\lambda_3^2 + \lambda_1^2\lambda_2^2 \\ I_3 &= \lambda_1^2\lambda_2^2\lambda_3^2 \end{aligned} \tag{53}$$

where λ_i ($i = 1,2,3$) represents the deformation of a differential cubic volume element along the principal axes of a Cartesian coordinate system and $I_3 = 1$ for an incompressible material such as elastomer in this study. From finite-strain theory in continuum mechanics, λ_i ($i = 1,2,3$) are the principal stretches that are in tandem square roots of the eigenvalues of the right Cauchy-Green strain tensor $\mathbf{C}$.

4.2.3 Boundary Conditions

The assumption was made that the tendon terminated at the distal end of the soft robot, specifically at $s = L$. Additionally, it was assumed that the tendon tension was applied tangentially to the extension direction of the soft robot, that is, in the local $x-$direction. Consequently, the following

relationship holds:

$$\mathbf{n}\big|_{s=L} = \mathbf{n}_i^t\big|_{s=L} + \mathbf{n}^{pr}\big|_{s=L} = -\tau_i \frac{\mathbf{R}\mathbf{p}_{i,s}^b(L)}{\|\mathbf{R}\mathbf{p}_{i,s}^b(L)\|} + PA^{ch}\mathbf{R}\hat{\mathbf{e}}_1 \tag{54}$$

$$\mathbf{m}\big|_{s=L} = \widehat{\mathbf{R}\mathbf{r}}_i^t \mathbf{n}_i^t\big|_{s=L} + \mathbf{l}_{pr}\big|_{s=L} = -\widehat{\mathbf{R}\mathbf{r}}_i^t \tau_i \frac{\mathbf{R}\mathbf{p}_{i,s}^b(L)}{\|\mathbf{R}\mathbf{p}_{i,s}^b(L)\|} + PA^{ch}\mathbf{R}[\mathbf{v}\times\hat{\mathbf{e}}_1] \tag{55}$$

Also, the initial set of BCs relates to the kinematic constraints at the base of the soft robot, i.e., at $s = 0$. From a mechanical standpoint, the soft robot can be considered as a cantilever, thereby implying that:

$$\mathbf{p}\big|_{s=0} = \mathbf{p}_0 \tag{56}$$

$$\mathbf{R}\big|_{s=0} = \mathbf{I}_{3\times 3} \tag{57}$$

The original shape of the soft robot before deformation, denoted as $\mathbf{p}_0$, serves as the reference point for the following analysis. These initial conditions give rise to six distinct scalar kinematic constraints that govern the behavior of the system. The prescribed set of six BCs outlined herein represents a collection of independent constraints that the solution must adhere to. These BCs impose specific requirements on the solution at both extremities of the soft robot. By satisfying these conditions, a BVP is formulated, wherein the goal is to identify a solution that satisfies the specified constraints at the boundaries. Resolving this BVP entails solving a system of differential equations to ascertain a solution that adequately meets the given constraints.

4.2.4 Solution Schema

To ascertain the deformation of the soft robot, the constitutive equations were incorporated into the force equations through a sequential procedure. It was assumed that the initial configuration of the robot was entirely known, facilitating the development of a precise mathematical model to evaluate its mechanical response. The system of nonlinear differential equations ((40)–(45)) was accompanied by two BCs concerning $\mathbf{n}$ and $\mathbf{m}$ at the distal end, while additional conditions pertaining to $\mathbf{p}$ and $\mathbf{R}$ were imposed at the proximal end of the soft robot. To address this problem, a shooting method was employed, entailing the initiation of a simulation loop and the iterative solution

of equation sets along with their respective BCs. This iterative process eventually culminated in the visualization of the system's response.

4.2.5 Pressure-Stiffening and Tangent Modulus

The tangent moduli, $\mathbf{K}_{se}(P)$ and $\mathbf{K}_{bt}(P)$ were determined as functions of P using the 2MR model and continuum balance equations. Based on the definitions in (48) and (49), $\mathbf{v}-\mathbf{v}^{\star}$ is the Lagrangian finite strain for shear and extension modes and $\mathbf{u}-\mathbf{u}^{\star}$ is the Lagrangian finite strain for bending and torsion. Assembling the Lagrangian finite strain Υ with adding local strains based on the prescribed internal forces and moments from extension, shear, and bending in tangent and oscular local planes resulted in:

$$\Upsilon = \begin{pmatrix} v_1 & v_2+u_1 & v_3-u_1 \\ v_2+u_1 & -\vartheta v_1 & 0 \\ v_3-u_1 & 0 & -\vartheta v_1 \end{pmatrix} \tag{58}$$

with $\vartheta \approx 0.5$ denoting the Poisson's ratio for incompressible polymers. On the other hand, the Lagrangian strain tensor is related to the right Cauchy-Green deformation tensor $\mathbf{C}$ such that:

$$\mathbf{C} = 2\Upsilon + \mathbf{I} \tag{59}$$

with $I_{ij} = \delta_{ij}$, the Kronecker's delta. On the other hand, the first and second principal invariants can be calculated from $\mathbf{C}$ using:

$$I_1 = \mathrm{Tr}(\mathbf{C}) \tag{60}$$

$$I_2 = \frac{1}{2}\left(\mathrm{Tr}(\mathbf{C})^2 - \mathrm{Tr}(\mathbf{C}^2)\right) \tag{61}$$

$$I_3 = \det(\mathbf{C}) = 1 \tag{62}$$

where $\mathrm{Tr}(X_{ij}) = X_{ii}$ is the trace operator (Einstein notation). Afterward, the second Piola Kirschoff stress σ definition in terms of $\mathbf{C}$ was used to find the relationship between $\mathbf{u}$ and $\mathbf{v}$ with stress components:

$$\sigma(P,\mathbf{C}) = -p^{\star} I_{3\times 3} + 2C_{10}\mathbf{C}^{T} - 2C_{01}\mathbf{C}^{-T} \tag{63}$$

with volumetric stress component $p^{\star}$:

$$p^{\star} = \frac{2}{3}\left(C_{10}I_1 - C_{01}I_2\right) \tag{64}$$

As can be seen in (63), the stress throughout the robot's body is affected by the internal pressure's effect on strain components manifested in σ while the robot's material properties affect the stress through C_{01} and C_{10}. In the end, to obtain the tangent elastic modulus the σ_{11} component of the stress tensor was used to obtain E as a function of P:

$$E(P) = \frac{\partial \sigma_{11}}{\partial \lambda_1} = \frac{\partial \sigma_{11}}{\partial I_1}\frac{\partial I_1}{\partial \lambda_1} + \frac{\partial \sigma_{11}}{\partial I_2}\frac{\partial I_2}{\partial \lambda_1} \tag{65}$$

where λ_1 is the square root of the largest eigenvalue of C tensor. To illustrate the effect of pressure on tangent elastic modulus three load cases were simulated. The first load case was pressurizing the chamber in the absence of tendon tension. This load case would theoretically result in mere tension in the soft robot and elongate its length without a significant bending effect. The second load case was applying a 3 N tensile force to one of the tendons in the absence of chamber pressurization. Theoretically, it was not expected to observe significant pressure-stiffening. However, small changes in elastic modulus were expected due to the natural strain-stiffening of the hyperelastic material. The third load case was the combination of load case 1 and load case 2, where the chamber was pressurized gradually up to 40 kPa in the presence of a 3 N tendon tension.

4.3 Validation Study

4.3.1 Soft Robot Design

In this study, a soft robot made of Ecoflex 00-50 with a central chamber and three tendons is designed. The outer diameter of the soft robot was 12 mm, and its length was 85 mm. In this design, the central chamber diameter was 3 mm, the chamber length was 80 mm, the diameter of tendon passages was 1.5 mm, and the tendons' offset is 4 mm. Table 4.2 summarizes the model parameters and 2MR material constants [90] used in the study.

Table 4.2: Model parameters and 2MR material constants of the prototyped soft robot.

Length	**Outer Dia.**	**Inner Dia.**	**Density**	**Tendon Offset**	**2MR Constants [90]**	
L (mm)	D_o (mm)	D_i (mm)	ρ ($\frac{g}{cc}$)	r (mm)	C_{10} (MPa)	C_{01} (MPa)
85	12	3	1.070	4	0.0188	-0.014

4.3.2 Experimental Setup

In order to construct the soft robot, an initial step involved creating a cylindrical mold through the utilization of a 3D printer (Replicator+, MakerBot, New York, NY, USA) and PLA material. The mold was designed to incorporate internal channels for the tendons and chamber. Additionally, a 3D-printed housing platform was employed to securely attach the soft robot's base to the aluminum frame. For the fabrication of the soft robot's body, Ecoflex 00-50 (Smooth-On Inc., Macungie, PA, USA) was selected. This material was prepared by thoroughly mixing parts A and B in a 1:1 ratio, followed by degassing the resulting silicone mixture within a vacuum chamber. After allowing the soft robot to rest at 24 $^{\circ}C$ for 24 hours to facilitate curing, it was deemed ready for testing.

Figure 4.4 illustrates the experimental setup employed in this study. To supply the necessary air pressure during the experiment, an air pump (KPM27CKoge Electronics, KMP Electronics Ltd., Sofia, Bulgaria) was utilized. Real-time monitoring of the chamber's pressure was achieved through the implementation of a pressure sensor (Phidgets Inc., Calgary, AB, Canada). Furthermore, an electronic pressure regulator (ITV0010-3UML, SMC, Tokyo, Japan) was employed to establish the desired internal pressure within the soft robot. To accurately track the position of the soft robot's tip, an electromagnetic motion tracker (Microsensor 1.8^{TM}, Polhemus, Colchester, VT, USA) was employed. The experimental setup was further enhanced by the integration of three motors (Maxon, EC 45 flat, 60 W, Irvine, CA, USA) equipped with a digital positioning controller (Maxon, EPOS4 Compact, Irvine, CA, USA) to provide tendon force at the tip of the soft robot. These motors were connected to a power supply (24 V, 10 A).

Furthermore, a specialized software application was created using the C# programming language to facilitate the acquisition and regulation of data pertaining to pneumatic servo-valves and motor torque. The control of the motors' torque was achieved through the utilization of Maxon's

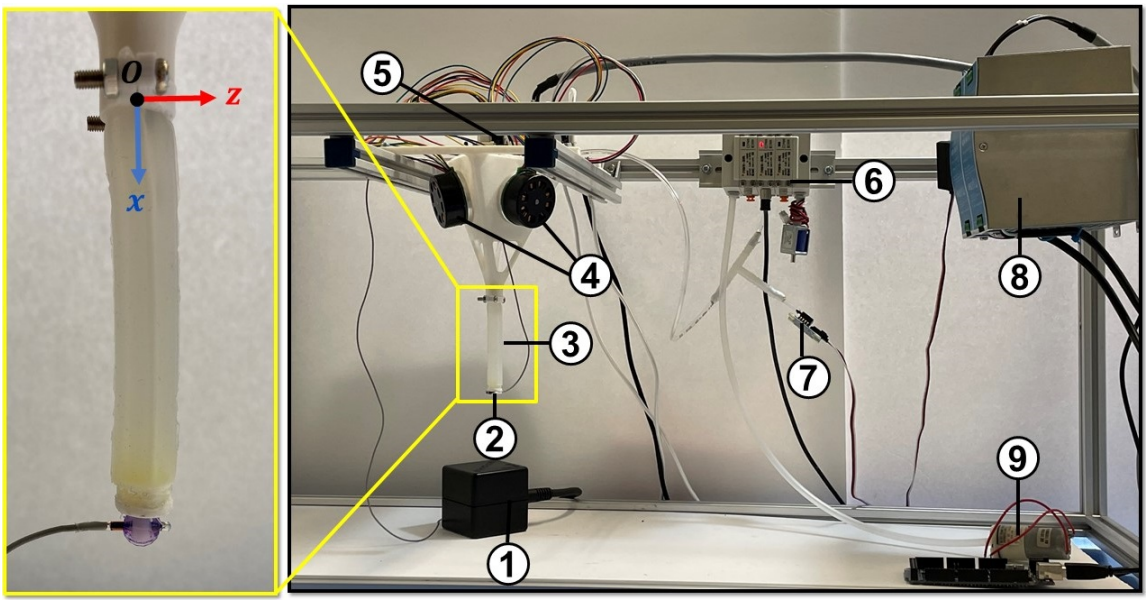

Figure 4.4: Components of the mechanical and electrical modules in the prototyped soft robot (1) source of electromagnetic field (2) tracking sensor (3) soft robot (4) motors (5) motor controller (6) electronic pressure controller and manifold (7) pressure sensor (8) power supply (9) air pump.

software development kit and the internal proportional-integral controller embedded within the motor driver. By employing the diameter of the pulley, an estimation of the tendon tension was derived. The control panel of the experimental setup is depicted in Figure 4.5.

4.3.3 Study Protocol

The objective of the conducted experiments was to validate the proposed hybrid-actuated soft robot model, which was based on the Cosserat rod model. To achieve this, a total of 15 experiments were performed, involving variations in chamber pressures ranging from 0 to 40 kPa and tendon forces ranging from 0 to 3 N. In order to ensure data reliability, each experiment was repeated three times, and the average results were reported. In each experiment, a fixed internal pressure was applied, followed by an increase in tendon forces, causing the soft robot to deform from its initial resting position. The first tendon force was gradually increased from 0 to 3 N in each experiment, while maintaining a constant pressure inside the air chamber. Subsequently, the first tendon was released, allowing the tip of the soft robot to return to its initial position. This process was then repeated for the second and third tendons. Additionally, the experiment was replicated for internal

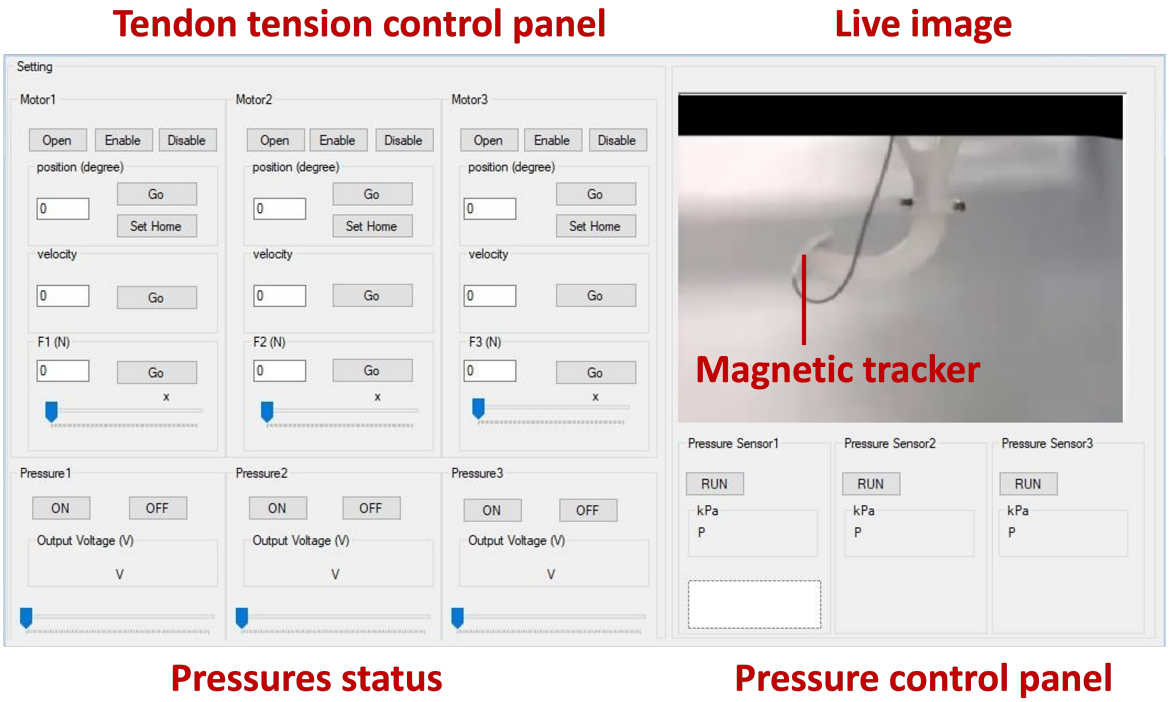

Figure 4.5: Tendon tension and pressure control panel of the experimental setup.

chamber pressures of 10, 20, 30, and 40 kPa.

During the pulling of the first tendon, the tip of the soft robot moved in the y-direction, while the distance of the tip in the x-direction decreased. As tendon 2 was pulled, the displacement of the tip increased in the z-direction, but decreased in both the y and x-directions. Concurrently, a magnetic tracking sensor recorded the position of the soft robot's tip for comparison and validation purposes. The recorded current data from the motors was utilized to solve the developed model, enabling a comparison between the computed tip positions and the actual positions (ground truth). Figure 4.6 illustrates the trajectory of the soft robot's tip under a 3 N tendon tension, without the presence of an internal chamber pressure ($P = 10$ kPa).

4.3.4 Results and Discussion

Based on the results of the experimental study, it was shown that, in accordance with the theories, for a given tendon tension and internal chamber pressure, the soft robot would have a pressure-stiffening effect. Figure 4.7 and Table 4.3 demonstrates the error of tip displacement in each experiment.

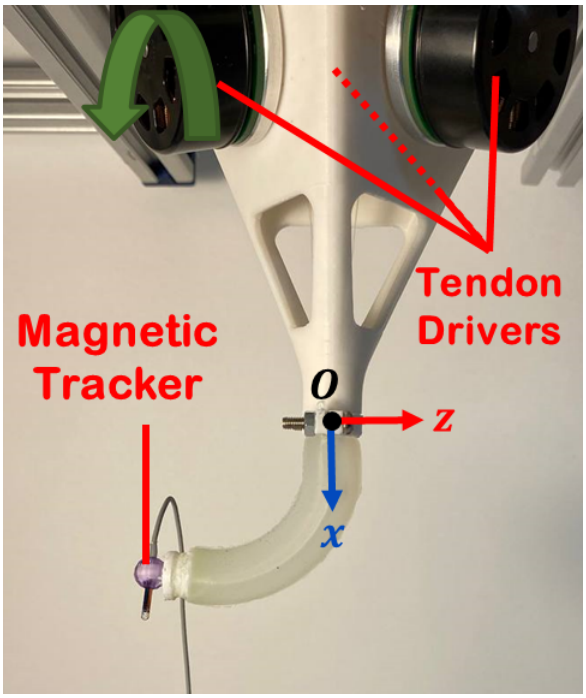

Figure 4.6: The deformation of a soft robot under the force of a 3 N tendon tension without the presence of internal chamber pressure.

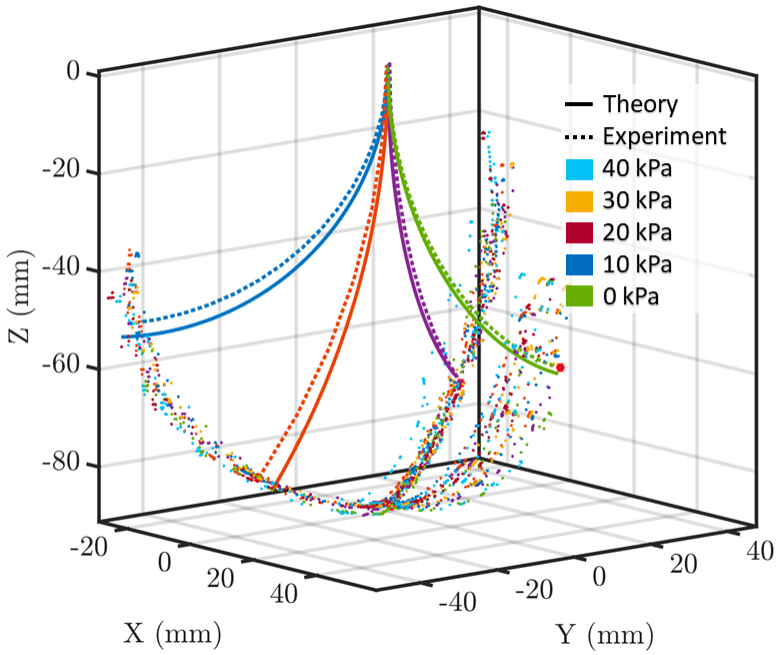

Figure 4.7: Comparison of the proposed Cosserat model with experimental setups under various internal pressures.

Table 4.3: Cosserat rod model prediction error with respect to experimental observations.

Pressure (kPa)	Tendon Tension (Sequential) F1 (N)	F2 (N)	F3 (N)	Tip Error Rel. MAE (%)
0	0–3	0	0	5.58%
10	0–3	0–3	0	5.12%
20	0–3	3	0–3	5.98%
30	0	0–3	0–3	5.89%
40	0	0	0–3	6.40%
Mean:				5.79%

Figure 4.8 illustrates the variation in rigidity (EI) of the soft robot in relation to the internal chamber pressure. The experiment was conducted three times for each chamber pressure, and the solid line represents the average value. The increase in internal pressure is observed to result in higher rigidity. The observed variation in rigidity aligns with the hyperelastic model employed to represent the material properties of the soft robot. The augmentation of EI with increasing air pressure inside the chamber can be attributed to two key factors. Firstly, the strain-stiffening effect induces an increase in the modulus of elasticity ($E(P)$). Secondly, the radial expansion of the soft robots contributes to an increase in the moment of inertia (I). To mitigate excessive radial expansion and constrain I, the utilization of fabric reinforcements was proposed as a solution [116].

Furthermore, a validation point was examined at $P = 25$ kPa to verify the predicted rigidity. It was determined that this point fell within the 95% confidence interval. Additionally, an optimization approach was employed to determine the appropriate EI that would minimize the error between the deformation predicted by the Cosserat model and the experimental data. Through an iterative process, the identified EI value was substituted into the constitutive equations to determine the position vector of the soft robot, denoted as $\mathbf{p}(s)$. The study findings have revealed that the Cosserat rod

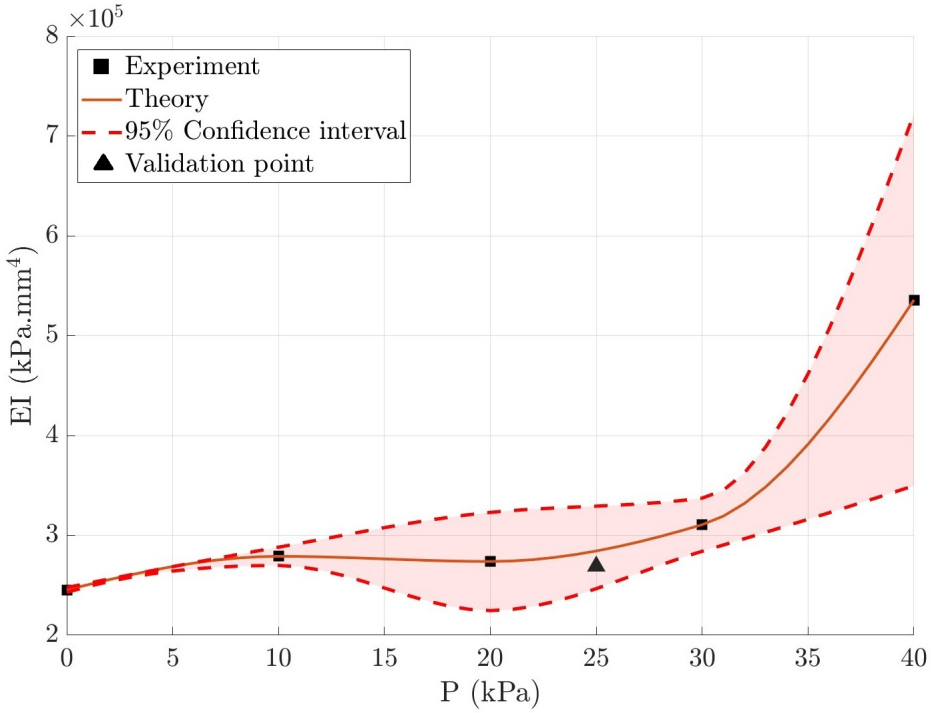

Figure 4.8: Variation of flexural rigidity of the soft robot with chamber pressure pressure-stiffening.

model was capable of accurately predicting the pressure-stiffening effect exhibited by soft robots. The experimental results indicated that the theoretical predictions yielded a maximum relative mean absolute error (MAE) of 6.4% in relation to the length of the robot. It is important to note that the experiment involved varying the tendon tensions within the range of 0 to 3 N, which resulted in the robot's tip exhibiting movement in 3D space (Figure 4.6). It is worth mentioning that the observed errors could potentially be attributed to the neglecting the soft robot's viscoelastic behavior and the failure to account for the radial expansion of the robot.

4.4 Summary

Throughout this study, the proposed mechanistic model of the soft robot was solved in order to determine the robot's shape at various pressures and tensions of its tendons. The proposed approach extended upon the existing literature by incorporating hyperelastic effects and stiffness adaptation through the utilization of an auxiliary pressure. To incorporate the effects of pressure-stiffening,

modifications were made to the volumetric stress component in the 2MR material model. Consequently, this modification resulted in an input-dependent tangent stiffness tensor in the Cosserat rod model. Experimental validation was conducted to verify the accuracy of the proposed model under various scenarios. An additional extension of this work would involve considering the effect of the ratio of the robot's cross-sectional area to its length on the accuracy of the model. It is important to note that flexure slenderness may impact the boundaries (in terms of pressure and tendon tension) within which the proposed model remains valid. Moreover, the feasibility of real-time dynamics for a hybrid-actuated soft robot, based on Cosserat rod models, will be explored. It is anticipated that this feature will enhance the state-of-the-art of soft surgical robots by introducing a new capability for adaptability during interventions.

Research Scope

Investigating a model-based approach for simulating the hybrid-driven soft robot that included: (1) Validating and assessing the feasibility of a Cosserat rod model to account for pressure-stiffening phenomena in a soft robot under both pneumatic and tendon-driven modalities. (2) Experimental validation of the proposed model for capturing the effects of pressure-stiffening effect during hybrid tendon-pneumatic actuation.

Objective

To model and validate the pressure-stiffening of a hybrid-driven soft robot, by employing the Cosserat rod model, accounting for material nonlinearity. The aim was to demonstrate the variation of flexural rigidity as a function of internal pressure, with the intention of utilizing it in intraluminal procedures in which the adjustable stiffness is required.

Contributions

The first and second authors contributed equally to this work [68]. The fourth and sixth authors are the academic advisors, and the fifth author is the academic supervisor. Majid's contributions

were in conceptualization, methodology, model derivation, theoretical results, prototype development, validation of the proposed model for stiffness adaptation, visualization, and writing—first draft and editing of the paper.

Chapter 5

Cosserat Rod-Based Dynamic Modeling of a Hybrid-Actuated Soft Robot for Robot-Assisted Cardiac Ablation

Soft robotics has emerged as a promising field due to the unique characteristics offered by compliant and flexible structures. Overcoming the challenge of precise position control is crucial in the development of such systems that require accurate modeling of soft robots. In response, a hybrid-actuated soft robot employing both air pressure and tendons was proposed, modeled, and validated using the dynamic Cosserat rod theory. This approach comprehensively addresses various aspects of deformation, including bending, torsion, shear, and extension. The designed robot was intended for robot-assisted cardiac ablation, a minimally invasive procedure that is used to treat cardiac arrhythmias. Within the framework of the Cosserat model, dynamic equations were discretized over time, and ordinary differential equations (ODEs) were solved at each time step. These equations of motion facilitated the prediction of the robot's response to different control inputs, such as air pressure and tension applied to the tendons. Experimental studies were conducted on a physical prototype to examine the accuracy of the model. The experiments covered a tension range of 0 to 3 N for each tendon and an air pressure range of 0 to 40 kPa for the central chamber. The results confirmed the accuracy of the model, demonstrating that the dynamic equations successfully predicted

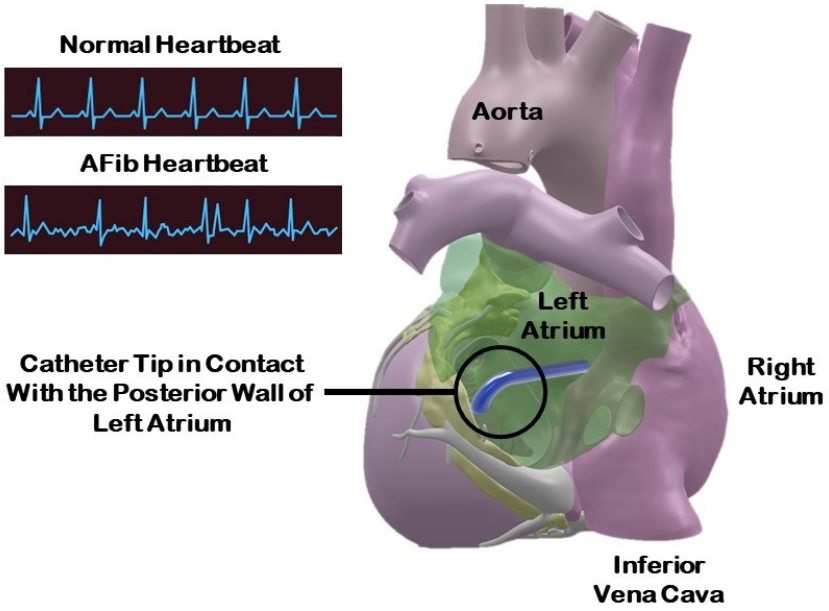

Figure 5.1: Representation of a hybrid-actuated soft robot during RFA ablation (3D heart model from Zygote Media Group Inc.).

the robot's motion in response to diverse control inputs.

5.1 Introduction

5.1.1 Background

Cardiac abnormalities have been widely recognized as a significant contributing factor to hospitalization and mortality worldwide. Arrhythmias, characterized by disruptions in heart rhythm resulting from changes in the electrical conduction system, represent the second most commonly observed clinical occurrence of cardiovascular abnormalities [117]. Atrial fibrillation (AFib), the most prevalent type of arrhythmia, exhibits the highest incidence rate [118]. The primary cause of AFib is the imbalanced discharge of signals originating from the pulmonary veins (PVs), leading to severe cardiovascular complications. Extensive research has demonstrated that individuals diagnosed with AFib face a risk of stroke incidence over five times higher than those without AFib [119].

Ablation catheters, which are long and flexible medical devices, had emerged as a prominent

treatment approach for stabilizing arrhythmia rates. Previous studies have indicated that the utilization of catheter-based ablation procedures was associated with a low risk of complications during the periprocedural phase and demonstrated a favorable safety profile [120]. During the ablation procedures, the ventricular muscles responsible for causing undesirable pulses or movements in the heart were incapacitated through either freezing or burning. Among the different modalities of ablation, Radio Frequency Ablation (RFA) had been considered the most favorable option. Nevertheless, the efficacy of RFA relied heavily on the size of the lesion created during the ablation process [121]. Figure 5.1 illustrates the configuration of a hybrid-actuated soft robot functioning as a catheter within a patient's heart during RFA ablation.

Robot-assisted catheter intervention (RCI) represents state-of-the-art technology used to treat cardiac abnormalities [122, 9]. The introduction of robotic catheterization aimed to mitigate the risks associated with traditional manual intervention methods [123, 13]. However, the currently available catheters have fixed stiffness and utilize rigid instruments [72, 74]. Adjusting the stiffness between the instrument and the organ within the patient's body is necessary during the manipulator's intervention for treatment or diagnosis to ensure a safe procedure [124]. Previous research has demonstrated that the efficacy of RFA is closely related to maintaining the catheter-tissue contact force within a range of 10 to 30 grf [125]. To address this challenge, recent studies have shown that soft robots can provide a range of stiffness options during an intervention, thereby ensuring the procedure's safety [68, 69, 70]

5.1.2 Hybrid-Actuated Soft Robots

Soft slender objects have gained increasing prominence in the field of surgical robotics, particularly in the context of soft manipulators [40, 126, 127] and soft sensors [75, 77, 79]. In an effort to overcome the constraints associated with single-actuation modalities, investigations have been undertaken into a hybrid-actuation modality. This approach consists of integrating two or more different driving modalities, with the intent of augmenting the load-bearing capacity and precision of control exhibited by flexible manipulatory systems. An illustrative example of such a hybrid-actuation mode is the combination of the fluid-actuation mode alongside the cable-actuation mode. The fluid-actuation mode demonstrated favorable characteristics in pressure-bearing while

exhibiting relatively weak performance in tensile-bearing. In contrast, the cable-actuation mode offered robust tensile-bearing while being limited in its capability to withstand compressive forces. Through the integration of these two different driving modalities, flexible manipulators stand to gain from both their pressure-bearing and tensile-bearing attributes, resulting in an amplification of load capacity and improved position control accuracy.

While recent research has focused on the inverse approach for force estimation [105, 58], forward dynamic models are essential for modeling and developing soft robot designs, control schemes, as well as studying dynamic events like catheterization in real-world scenarios. In surgical interventions, accounting for sudden dynamic movements is crucial, even when the system exhibits minimal inertia effects and acceleration. Such unexpected movements can significantly impact procedural outcomes and jeopardize patient safety. Thus, a real-time dynamic model that can anticipate and compensate for these movements becomes indispensable. Dynamic movements primarily arise from the structure of the robot, loading conditions, and discontinuous changes in loading, rendering quasi-static assumptions inadequate for accurately estimating deformations in soft robots [128]. Numerous approaches have been proposed in the literature for modeling soft robots. For instance, the PCC representation has been employed to model robot shapes [86, 2]. However, under the consideration of external loads or inertial dynamics, a CC representation may no longer be sufficient due to torsion, shear, extension, or variations in curvature. To address this challenge, a Cosserat-based dynamic formulation for hybrid-driven soft robots under general loading conditions was introduced.

A key contribution of this study lies in the derivation of a set of dynamic PDEs for a soft robot that is actuated simultaneously by air pressure and tendons. The principal distinction from prior research lay in the incorporation of the time-dependent parameter within the Cosserat rod model. The governing equations of motion for a slender soft robot are presented in Section 5.2, followed by a proposed representation of forces and moments generated by tendons and an air chamber. Furthermore, a linear constitutive model is employed to establish a relationship between loadings and the material properties of the soft robot. By discretizing time, the set of PDEs is transformed into a system of ODEs, enabling the estimation of the soft robot's shape based on known BCs. In Section 5.3, the obtained results are presented and discussed in conjunction with the theoretical framework, allowing for a comprehensive comparison.

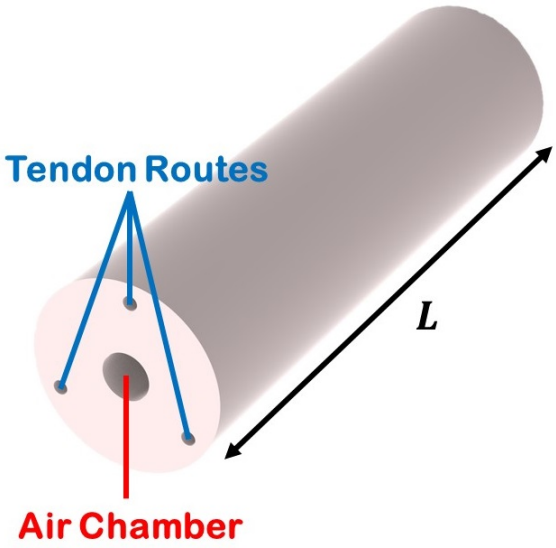

Figure 5.2: Air chamber and tendons routes of hybrid-actuated soft robot.

5.2 Materials and Methods

5.2.1 Dynamic Model of a Hybrid-Actuated Soft Robot

Governing Equations of Motion

Slender objects can be effectively represented as one-dimensional structures, with their state variables being expressed as functions of time t and an arc length parameter $s \in [0 \;\; L]$, where L denotes the length of the soft robot. In this study, the soft robot is equipped with a central channel to regulate air pressure, along with m pathways to accommodate the passage of tendons. The configuration of the robot's cross-section, depicted in Figures 5.2 and 5.3, serve to illustrate the arrangement of the air chamber and tendons, where r represents the radius of the backbone, and r^t indicates the offset of the tendons from the central axis. When the air chamber is inflated and the tendons are tensioned, the backbone of the robot becomes subject to various forces and moments. Consequently, this results in deformation, which can be accurately described using the Cosserat rod model. The dynamic response of the robot is dependent upon its mechanical properties as well as external loads applied to it. As a general principle, a Cosserat rod is characterized by the curve of its centerline, denoted as $\mathbf{p}(s,t)$, as well as a rotation matrix, denoted as $\mathbf{R}(s,t)$. Moreover, in the local frame, the rate of positional change with respect to arc length is represented by $\mathbf{v}(s,t)$, while

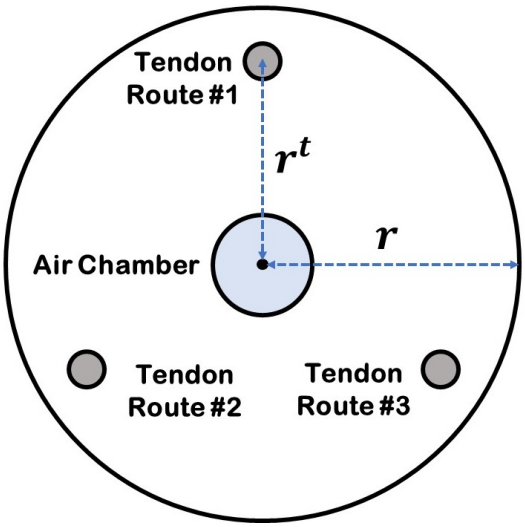

Figure 5.3: Cross section of the soft robot in which r is the backbone radius, and r^t is the tendons offsets.

the curvature is defined by $\mathbf{u}(s,t)$ [87]:

$$\begin{aligned} \mathbf{v} &= \mathbf{R}^T \mathbf{p}_{,s} \\ \mathbf{u} &= \left(\mathbf{R}^T \mathbf{R}_{,s}\right)^\vee \end{aligned} \tag{66}$$

where $(.)^T$ is the transpose of vector, $\mathbf{X}_{,s} = \partial \mathbf{X}/\partial s$ in which $\mathbf{X}$ is a dummy symbol (same for $\mathbf{X}_{,t} = \partial \mathbf{X}/\partial t$), and operator $(.)^\vee$ maps $\mathfrak{so}(3)$ to $\mathbb{R}^3$. For a typical vector $\mathbf{a} = [a_1 \;\; a_2 \;\; a_3]^T$ [129]:

$$\widehat{\mathbf{a}} = \begin{bmatrix} 0 & -a_3 & a_2 \\ a_3 & 0 & -a_1 \\ -a_2 & a_1 & 0 \end{bmatrix} \text{ and } (\widehat{\mathbf{a}})^\vee = \mathbf{a} \tag{67}$$

Linear velocity $\mathbf{q}(s,t)$ and angular velocity $\omega(s,t)$ in the local frame can also be calculated using time derivation of centerline curve and orientation matrix as [87]:

$$\begin{aligned} \mathbf{q} &= \mathbf{R}^T \mathbf{p}_{,t} \\ \omega &= \left(\mathbf{R}^T \mathbf{R}_{,t}\right)^\vee \end{aligned} \tag{68}$$

An arbitrary element of the rod with the corresponding parameters was illustrated in Figure 5.4. By assuming constant tendon tension along the length and fixed tendon locations relative to the

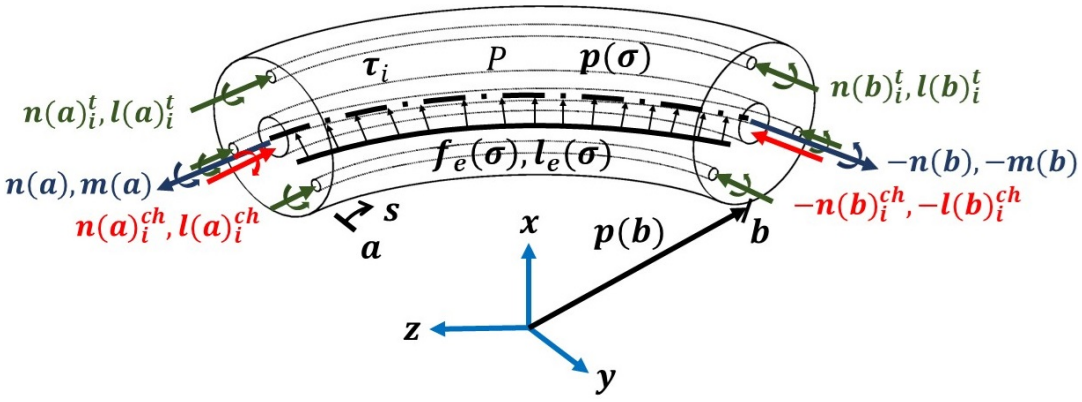

Figure 5.4: An arbitrary element of the hybrid-actuated soft robot subject to distributed forces and moment at the time t.

robot's cross-section during deformation, the PDEs that govern the dynamic response of a soft robot in the global coordinate frame were formulated [87]:

$$\begin{aligned}
\mathbf{p}_{,s} &= \mathbf{R}\mathbf{v} \\
\mathbf{R}_{,s} &= \mathbf{R}\widehat{\mathbf{u}} \\
\mathbf{q}_{,s} &= \mathbf{v}_{,t} - \widehat{\mathbf{u}}\mathbf{q} + \widehat{\omega}\mathbf{v} \\
\omega_{,s} &= \mathbf{u}_{,t} - \widehat{\mathbf{u}}\omega \\
\mathbf{n}_{,s} &= \rho A\mathbf{R}(\widehat{\omega}\mathbf{q} + \mathbf{q}_{,t}) - \mathbf{f} \\
\mathbf{m}_{,s} &= (\rho\mathbf{R}\mathbf{J}\omega)_{,t} - \widehat{\mathbf{p}}_{,s}\mathbf{n} - \mathbf{l} \\
\mathbf{p}_{,t} &= \mathbf{R}\mathbf{q} \\
\mathbf{R}_{,t} &= \mathbf{R}\widehat{\omega}
\end{aligned} \tag{69}$$

where $\mathbf{n}(s,t)$ and $\mathbf{m}(s,t)$ are the internal force and moment in the global frame, $\mathbf{f}(s,t)$ and $\mathbf{l}(s,t)$ are the general distributed external force and moment, A is the soft robot cross-sectional area, ρ is the material density, and $\mathbf{J}$ is the second mass moment of inertia tensor:

$$\mathbf{J} = \begin{bmatrix} I_{xx} & 0 & 0 \\ 0 & I_{yy} & 0 \\ 0 & 0 & I_{zz} \end{bmatrix} \tag{70}$$

in which I_{xx}, I_{yy}, I_{zz} are the second moment of area. For a circular rod $I_{xx} = I_{yy} = \pi r^4/4$ with soft robot radius r, and $I_{zz} = I_{xx} + I_{yy}$. Also, general force and moment terms in (89) can be defined as:

$$\begin{aligned} \mathbf{f} &= \mathbf{f}_{te} + \mathbf{f}_{pr} + \mathbf{f}_{e} \\ \mathbf{l} &= \mathbf{l}_{te} + \mathbf{l}_{pr} + \mathbf{l}_{e} \end{aligned} \tag{71}$$

where $\mathbf{f}_{te}$ and $\mathbf{l}_{te}$ are distributed force and moment terms due to tendon tension, $\mathbf{f}_{pr}$ and $\mathbf{l}_{pr}$ are distributed force and moment terms due to air pressure, and $\mathbf{f}_{e}$ and $\mathbf{l}_{e}$ denote any other external distributed force and moment terms, respectively. The tendon force and moment can be rewritten in terms of backbone kinematic parameters as [94]:

$$\begin{aligned} \mathbf{f}_{te} &= \mathbf{R}(\mathbf{a} + \mathbf{A}\mathbf{v}_{,s} + \mathbf{G}\mathbf{u}_{,s}) \\ \mathbf{l}_{te} &= \mathbf{R}(\mathbf{b} + \mathbf{G}^T\mathbf{v}_{,s} + \mathbf{H}\mathbf{u}_{,s}) \end{aligned} \tag{72}$$

in which:

$$\begin{aligned} \mathbf{a} &= \sum_{i=1}^{m} \mathbf{a}_i \quad \mathbf{a}_i = \mathbf{A}_i[\widehat{\mathbf{u}}(\mathbf{p}_{i,s}^b + \mathbf{r}_{i,s}^t) + \mathbf{r}_{i,ss}^t] \\ \mathbf{b} &= \sum_{i=1}^{m} \mathbf{b}_i \quad \mathbf{b}_i = \widehat{\mathbf{r}}_i^t \mathbf{a}_i \\ \mathbf{A} &= \sum_{i=1}^{m} \mathbf{A}_i \quad \mathbf{A}_i = -\tau_i \frac{\left((\mathbf{p}_{i,s}^b)^\wedge\right)^2}{\|\mathbf{p}_{i,s}^b\|^3} \\ \mathbf{G} &= \sum_{i=1}^{m} \mathbf{G}_i \quad \mathbf{G}_i = -\mathbf{A}_i \widehat{\mathbf{r}}_i^t \\ \mathbf{H} &= \sum_{i=1}^{m} \widehat{\mathbf{r}}_i^t \mathbf{G}_i \\ \mathbf{p}_{i,s}^b &= \widehat{\mathbf{u}}\mathbf{r}_i^t + \mathbf{r}_{i,s}^t + \mathbf{v} \end{aligned} \tag{73}$$

which $\mathbf{p}^b$ is the representation of the variable $\mathbf{p}$ in the local frame (i.e. $\mathbf{p}^b = \mathbf{R}^T\mathbf{p}$) and τ_i is the tendon tension. Air pressure forces always act normally on a cross-sectional plane. Thus, distributed forces ($\mathbf{f}_{pr}$) and moments ($\mathbf{l}_{pr}$) due to air chamber can be considered as:

$$\begin{aligned} \mathbf{f}_{pr} &= PA^{ch}\mathbf{R}_{,s}\mathbf{e}_3 \\ \mathbf{l}_{pr} &= PA^{ch}\mathbf{R}[\mathbf{v} \times \mathbf{e}_3] \end{aligned} \tag{74}$$

where P and A^{ch} are the uniform pressure and cap area of the air chamber, respectively. Also, $\mathbf{e}_3$ is the unit vector ($\mathbf{e}_3 = [0\ \ 0\ \ 1]^T$). Lastly, external distributed forces can be considered as gravitational and air drag resistance forces, thus $\mathbf{f}_e = \mathbf{f}_d + \mathbf{f}_g$:

$$\begin{aligned} \mathbf{f}_d &= \mathbf{RCq} \odot |\mathbf{q}| \\ \mathbf{f}_g &= \rho A \mathbf{g} \end{aligned} \tag{75}$$

where $\mathbf{g}$ is gravitational acceleration vector, $\mathbf{C}$ is the square-law-drag damping coefficient, and $\odot$ is the Hadamard product.

Material Constitutive Law

The dynamic system, governed by (89), had independent variables $\mathbf{v}$ and $\mathbf{u}$. Therefore, it was necessary to implement a material constitutive law to establish the relationship between these variables and internal loadings. By combining the Cosserat rod model with the appropriate constitutive laws, a set of PDEs was derived to describe the dynamic response of the system. For the purposes of this study, the backbone of the system was assumed to be composed of elastic materials, and a linear elasticity law with material damping was employed [87]:

$$\begin{aligned} \mathbf{n} &= \mathbf{R}\left[\mathbf{K}_{se}(\mathbf{v} - \mathbf{v}^*) + \mathbf{B}_{se}\mathbf{v}_{,t}\right] \\ \mathbf{m} &= \mathbf{R}\left[\mathbf{K}_{bt}(\mathbf{u} - \mathbf{u}^*) + \mathbf{B}_{bt}\mathbf{u}_{,t}\right] \end{aligned} \tag{76}$$

where $\mathbf{v}^*$ and $\mathbf{u}^*$ corresponded to the initial posture of the rod when $\mathbf{n} = \mathbf{0}$ and $\mathbf{m} = \mathbf{0}$, respectively. For a rod that is initially straight in z-direction, $\mathbf{v}^* = [0\ \ 0\ \ 1]^T$ and $\mathbf{u}^* = [0\ \ 0\ \ 0]^T$. Also, $\mathbf{K}_{se} = diag(GA\ \ GA\ \ EA)$ is the stiffness matrix for shear and extension, and $\mathbf{K}_{bt} = diag(EI_{xx}\ \ EI_{yy}\ \ GI_{zz})$ is the stiffness matrix for bending and torsion, in which E is Young's modulus, G is the shear modulus, in which $E = 2G(1+\nu)$ where ν is Poisson's ratio. Also, $\mathbf{B}_{se}$ and $\mathbf{B}_{bt}$ are coefficients for Kelvin–Voigt-type viscous damping [130].

Boundary Conditions

Consider a soft robot with three tendons and a central air chamber in a cantilever configuration (Figure 5.5). Tendons that are terminated at the distal end as well as the cap of the air chamber will

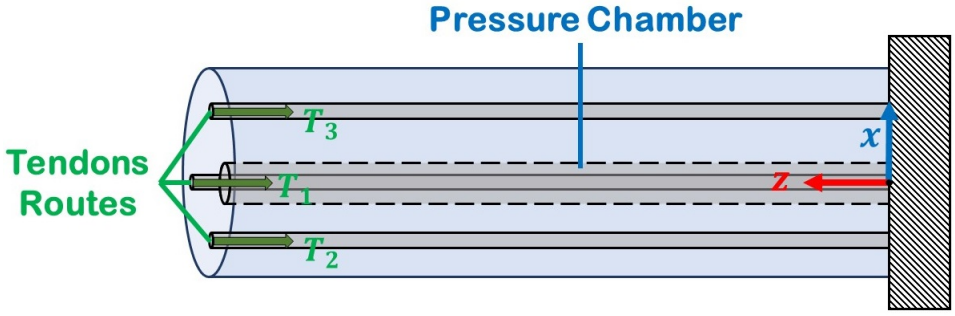

Figure 5.5: Cantilever configuration of a hybrid-actuated soft robot.

contribute to BCs. As tendon tension is always and anywhere tangent to posture, the clamp-free soft robot BCs would be:

$$s = 0 \rightarrow \begin{cases} \mathbf{p} = \mathbf{p}_0 \\ \mathbf{R} = \mathbf{I}_{3\times 3} \\ \mathbf{q} = \mathbf{0} \\ \omega = \mathbf{0} \end{cases} \tag{77}$$

$$s = L \rightarrow \begin{cases} \mathbf{n} = \mathbf{n}_i^t + \mathbf{n}_i^{pr} = -\tau_i \frac{\mathbf{R}\mathbf{p}_{i,s}^b(L)}{\|\mathbf{R}\mathbf{p}_{i,s}^b(L)\|} + PA^{ch}\mathbf{R}\mathbf{e}_3 \\ \mathbf{m} = \widehat{\mathbf{R}\mathbf{r}}_i^t \mathbf{n}_i^t + \mathbf{l}_{pr} \end{cases} \tag{78}$$

where $\mathbf{p}_0$ proximal position, $\mathbf{I}$ is the identity matrix. The shooting method was employed to solve the BVP iteratively by estimating the unknown initial values. Subsequently, the guessed values were iteratively adjusted using a selected nonlinear optimization routine to minimize the residual error of the distal BCs until they reached zero.

Semi-Discretization in Time for General PDE Solution

By substituting the formulas of implicit differentiation for all the time derivative terms in (89), a set of ODEs could be derived. Given the initial configuration of the robot, the dynamic simulation loop was initiated, and the problem was iteratively solved in the time domain. In order to achieve

this, Backward Differentiation Formulas of order (BDF-α) were employed for the implicit approximation of time derivatives [131]. Additionally, the shooting method utilizing MATLAB's fsolve function and the forward Euler method for spatial integration were employed. The time derivatives of any state variables y could be calculated as follows:

$$y_{,t}^{(i)} = c_0 y^{(i)} + c_1 y^{(i-1)} + c_2 y^{(i-2)} + d_1 y_{,t}^{(i-1)} \tag{79}$$

in which:

$$\begin{aligned} c_0 &= (1.5+\alpha)/[\delta t(1+\alpha)] \quad c_1 = -2/\delta t \\ c_2 &= (0.5+\alpha)/[\delta t(1+\alpha)] \quad d_1 = \alpha/(1+\alpha) \end{aligned} \tag{80}$$

with α representing the coefficient associated with the BDF-α method, and δt denoting the time increment. The iterative solution of the ODE set, along with the corresponding BCs, was carried out by implementing Euler's method. The current problem encompassed four BCs, specifically pertaining to the variables **p**, **q**, **R**, and ω, at the proximal end, while the remaining BCs for **n** and **m** were present at the distal end.

5.2.2 Experimental Setup

Consideration was given to a tendon-driven pneumatic-actuated soft robot comprising a central chamber and three tendons positioned angularly around the backbone, separated by a fixed angle of 120°. The soft robot had an outer diameter of 12 mm. The design consisted of a central chamber with a diameter of 3 mm. The tendon passages possessed a diameter of 1.5 mm, while the tendons were offset by 4 mm. The pertinent model parameters employed to solve the set of equations outlined in (89) during the study are summarized in Table 5.1. Initially, the rod was assumed to be straight, thus establishing a correlation between the initial conditions and the rod's straight posture.

The fabrication process of the soft robot was conducted by employing a 3D printer (Replicator+, MakerBot) to swiftly produce a cylindrical mold with internal passages, designed to accommodate the chamber and tendons. Additionally, a 3D-printed housing platform was created to facilitate the installation of the soft robot's base into the aluminum frame. The body of the soft robot was constructed using Ecoflex 00-50 (Smooth-On Inc., PA, USA), a silicone mixture comprising two

Table 5.1: Model parameters of the soft robot.

Parameter	Symbol	Value	Unit
Backbone radius	r	6	mm
Air chamber diameter	D^{ch}	3	mm
Tendon passages diameter	D^{t}	1.5	mm
Tendons offset	r^{t}	4	mm
Young's modulus	E	0.05	MPa
Density	ρ	1070	kg/m^3
Poisson's ratio	ν	0.49	–
Viscous damping coefficients (bt) [87]	$\mathbf{B_{bt}}$	$10^{-6} \times \mathbf{I}$	Nm^2
Viscous damping coefficients (se) [87]	$\mathbf{B_{se}}$	$\mathbf{0}$	Nm^2
Drag damping coefficient [87]	$\mathbf{C}$	$0.03 \times \mathbf{I}$	kg/m^2
Time increment [87]	δt	0.015	s
Coefficient of BDF-alpha method [87]	α	-0.2	–

parts, A and B, in a 1:1 ratio. This mixture underwent degassing in a vacuum chamber and was subsequently allowed to cure for a duration of 24 hours at a temperature of $24°C$. To supply air pressure, an air pump (KPM27CKoge Electronics) was utilized, while a pressure sensor (Phidgets Inc.) was employed to record real-time pressure measurements within the chamber throughout the experiment. The internal pressure of the soft robot was precisely regulated using an electronic pressure regulator (ITV0010-3UML, SMC). The position of the soft robot's tip was tracked using an electromagnetic motion tracker (Microsensor 1.8 mm, Polhemus). Moreover, the experimental setup incorporated three motors (Maxon, EC 45 flat, 60 W) and a digital positioning controller (Maxon, EPOS4 Compact) to provide tendon force at the tip of the soft robot. These motors were connected to a power supply (24 V, 10 A). The experimental setup employed in this study is illustrated in Figure 5.6.

Furthermore, a C# program was meticulously developed to facilitate the acquisition and regulation of pneumatic pressure and motor torque. The motors' torque control was effectively accomplished by employing Maxon's software development kit and harnessing the inherent proportional-integral controller of the motor driver. To accurately estimate the tension of the tendons, the pulley's

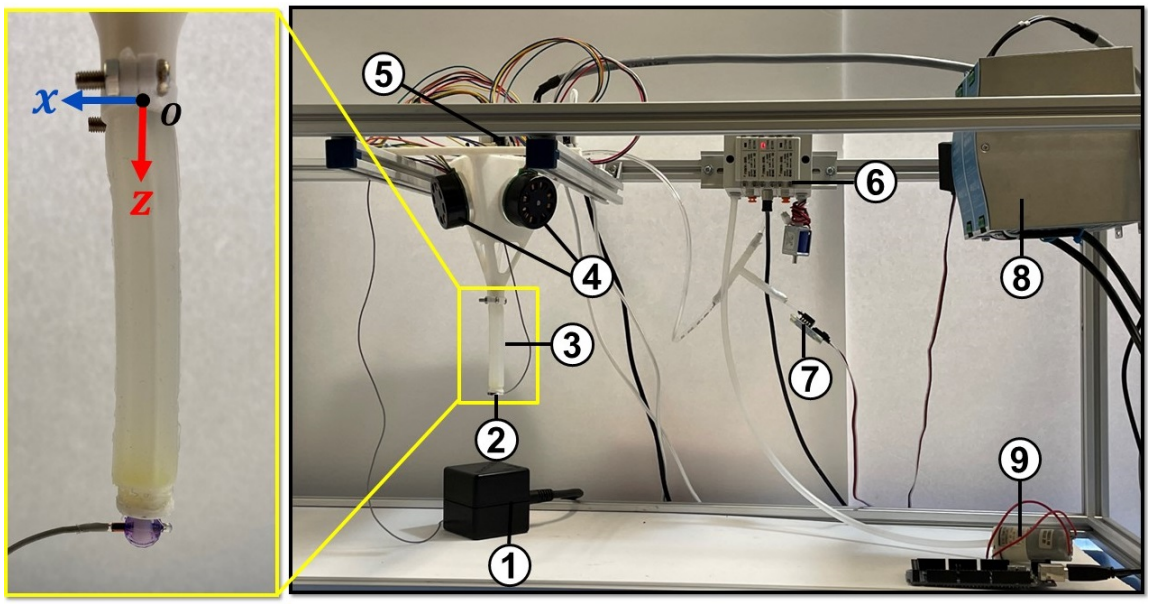

Figure 5.6: Components of the mechanical and electrical modules in the prototyped soft robot (1) source of electromagnetic field (2) tracking sensor (3) soft robot (4) motors (5) motor controller (6) electronic pressure controller and manifold (7) pressure sensor (8) power supply (9) air pump.

diameter was incorporated in conjunction with the motor torque control capabilities provided by the aforementioned software. In the validation study, a series of fifteen experiments were conducted to investigate the influence of chamber pressure and tendon tension on the deformation of a soft robot. The experiments involved varying the chamber pressures from 0 kPa to 40 kPa and the tendon forces from 0 N to 3 N. To enhance the reliability of the findings, each experiment was repeated three times, and the average measurements were recorded. Throughout each experiment, the tendon forces were gradually increased from 0 N to 3 N while maintaining a constant pressure inside the air chamber. As the tendon forces increased, the soft robot underwent deformation from its initial resting position. Upon reaching the maximum force of 3 N, the first tendon was released, causing the tip of the soft robot to return to its original position. This process was repeated for the second and third tendons. The experiments were further repeated under four different internal chamber pressures: 10, 20, 30, and 40 kPa. The experimental validation methodology employed in this study is presented in Table 5.2.

During each experiment, the tip position of the soft robot was recorded by the magnetic tracking sensor to facilitate a comparison with the results obtained from the Cosserat model. These

Table 5.2: Experimental validation methodology.

Case	Pressure	Tendons Tensions (Sequential)		
	P (kPa)	τ_1 (N)	τ_2 (N)	τ_3 (N)
1	0	0-3	0	0
2	10	0-3	0-3	0
3	20	0-3	0	0-3
4	30	0	0-3	0-3
5	40	0	0	0-3

recorded positions were subsequently evaluated against the ground truth data in order to ascertain the accuracy of the model. The results provided strong evidence that the deformations exhibited by the soft robot were consistent with the predictions of the established model. As depicted in Figures 5.7-5.10, the configurations of the soft robot were illustrated, showcasing its initial shape and the impact of a 3 N tendon tension on each motor individually, while applying an internal chamber pressure of 10 kPa. The analysis conducted in the subsequent section revealed that, under fixed conditions of internal chamber pressure and tendon tension, the soft robot consistently demonstrated similar deformation patterns. This finding further bolstered the alignment between the soft robot's behavior and the anticipated outcomes outlined by the Cosserat model. Furthermore, Figure 5.11 illustrated the tip trajectory of the hybrid-actuated soft robot, providing a visual representation of its motion characteristics. The depicted trajectory served as supplementary evidence supporting the alignment between the observed behavior of the soft robot and the predictions derived from the model. Through the comprehensive analysis of experimental results and a thorough examination of the soft robot's behavior, it was convincingly demonstrated that the deformations of the soft robot were in accordance with the expectations established by the Cosserat model.

5.3 Results and Discussion

Figures 5.12 and 5.13 show the test data and working space of the soft robot. As can be seen, first, the internal pressure of the air chamber was set to a constant amount, and then the tip of the soft robot was pulled to the x-axis. Then the robot returned to its initial position, and the second

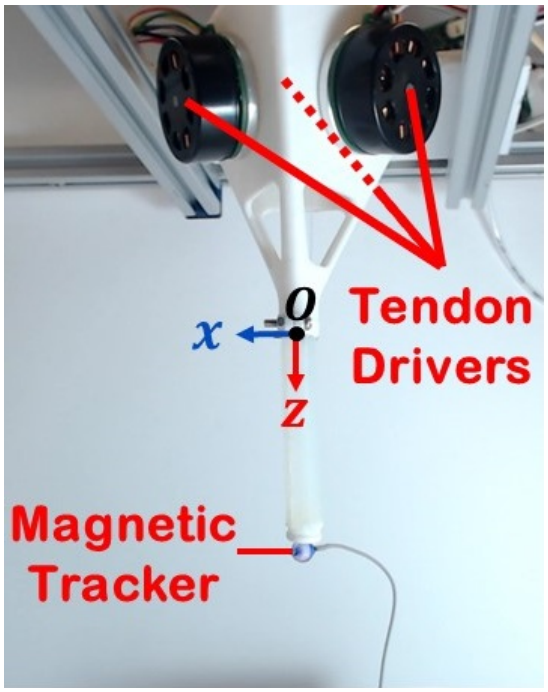

Figure 5.7: Initial shape of soft robot

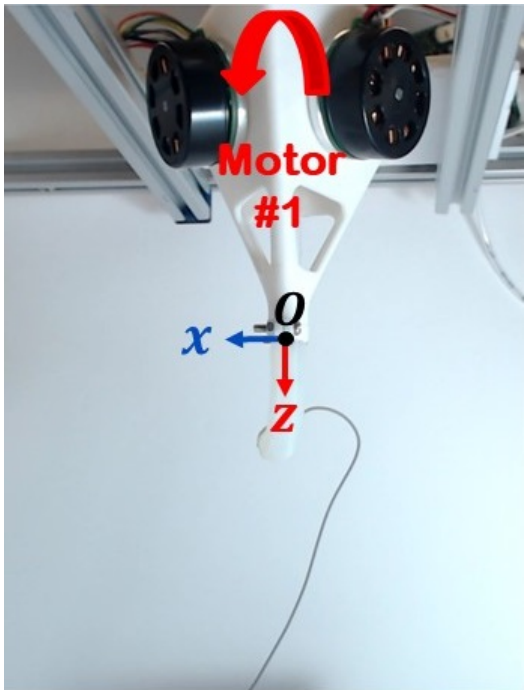

Figure 5.8: The effect of 3 N tendon tension on each motor while applying a 10 kPa of internal chamber pressure on the deformation of the soft robot.

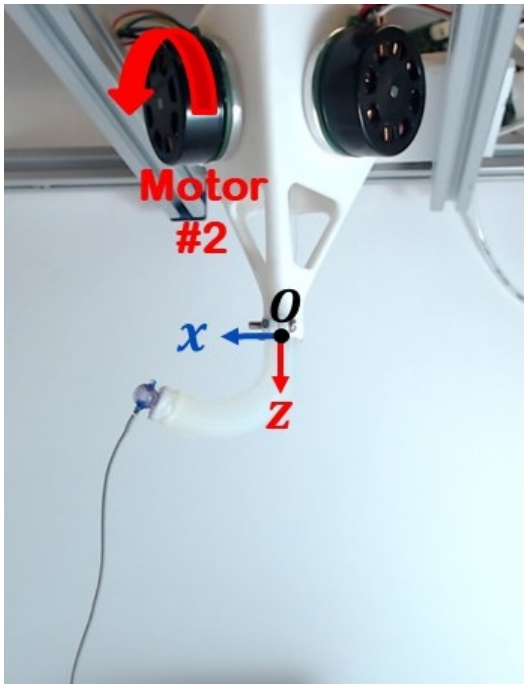

Figure 5.9: The effect of 3 N tendon tension on each motor while applying a 10 kPa of internal chamber pressure on the deformation of the soft robot.

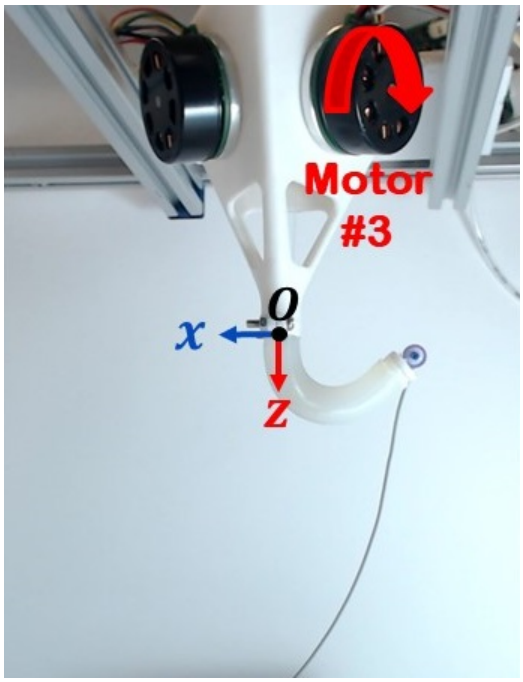

Figure 5.10: The effect of 3 N tendon tension on each motor while applying a 10 kPa of internal chamber pressure on the deformation of the soft robot.

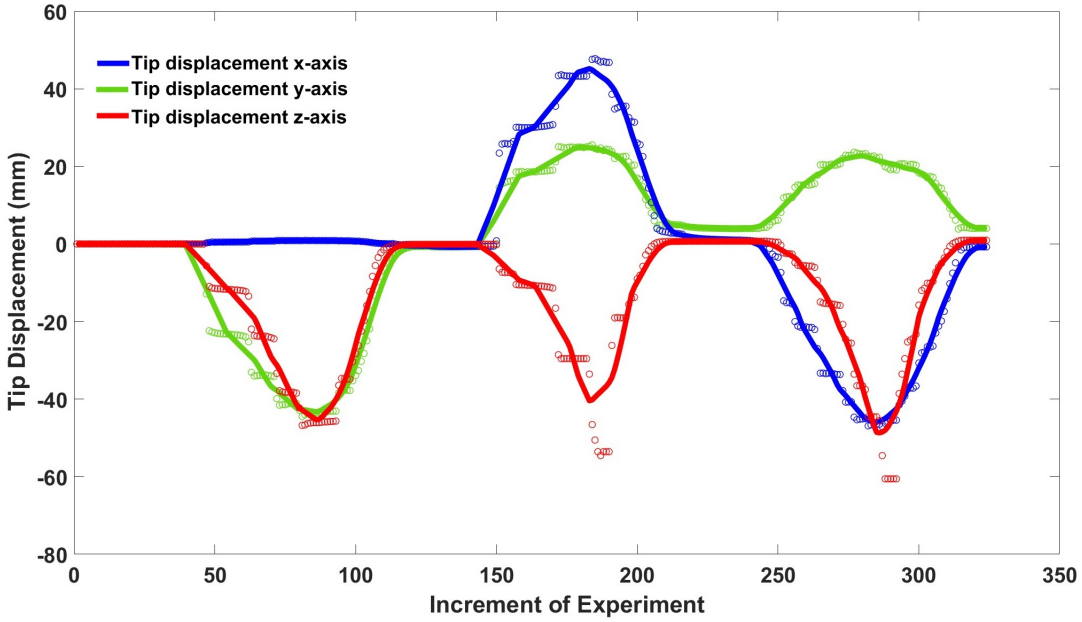

Figure 5.11: Tip trajectory of the hybrid-actuated soft robot as three tendons were successively pulled at 3 N each, maintaining a constant chamber pressure of 10 kPa in the x, y, and z-axes. The white dots represent the precise measured values for the tip of the soft robot in the x, y, and z components, obtained using the magnetic tracker probe.

tendon, which was tied at a 120° with respect to the first tendon, was pulled. The same procedure was repeated for the third tendon. Figure 5.13 shows the total working space of the tip of a soft robot that can be achieved through the simultaneous pulling of the three tendons. The comparison between the theoretical predictions from the Cosserat model and experimental measurements demonstrated a low relative Mean-Absolute-Error (MAE) in relation to the length of the robot, indicating the model's ability to accurately predict the behavior of the hybrid-actuated soft robot.

This suggests that the model is a reliable tool for analyzing and predicting the deformations of the entirely soft robot. However, it is essential to acknowledge that the results may not fully encompass all the phenomena observed in the experimental measurements. This limitation stems from the exclusion of the viscoelastic behavior of the soft material, which was not considered in the material model. The neglected viscoelastic properties could potentially introduce additional complexities and affect the accuracy of the predictions.

The findings further demonstrated the validity and applicability of the Cosserat model in describing the dynamic movements of soft robots. Figure 5.14 illustrates the 3D deformation of the

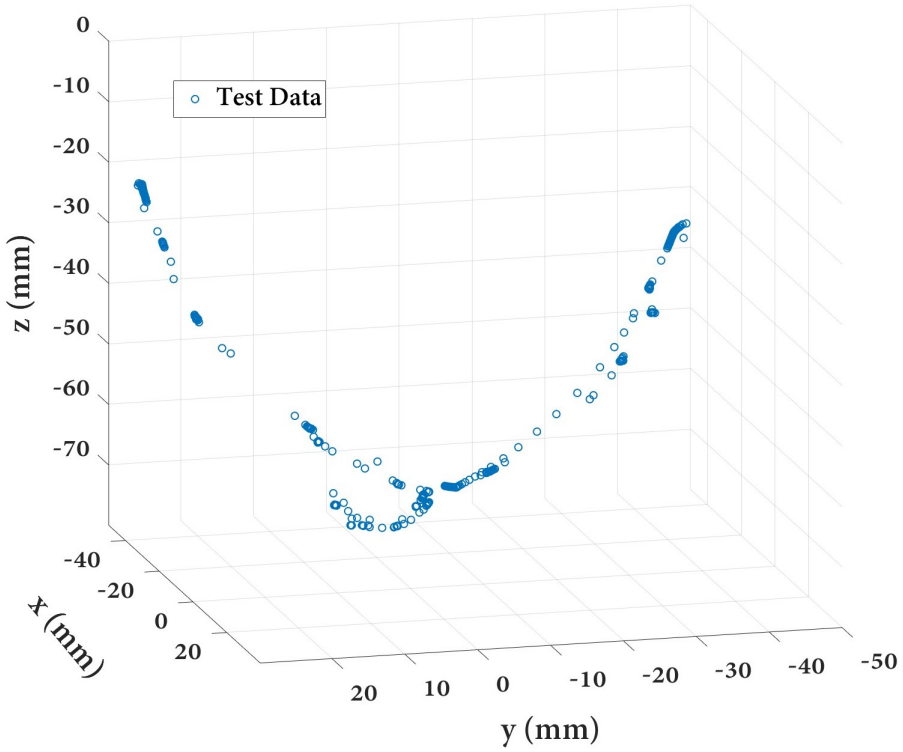

Figure 5.12: Test data from the experiments: Tip position of the soft robot

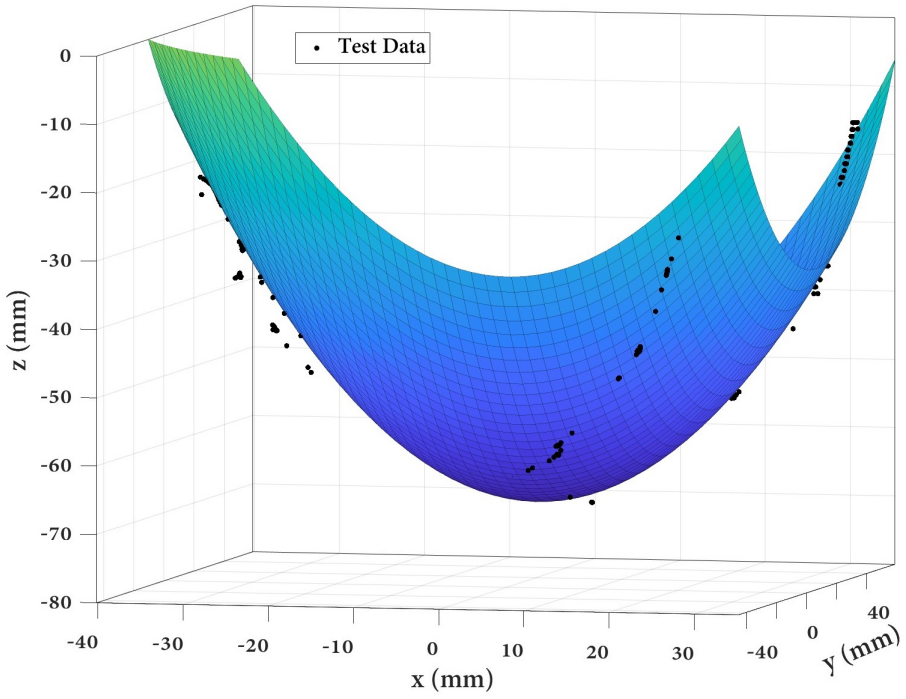

Figure 5.13: Test data from the experiments: Working space of the hybrid-actuated soft robot in the x, y, and z-axes.

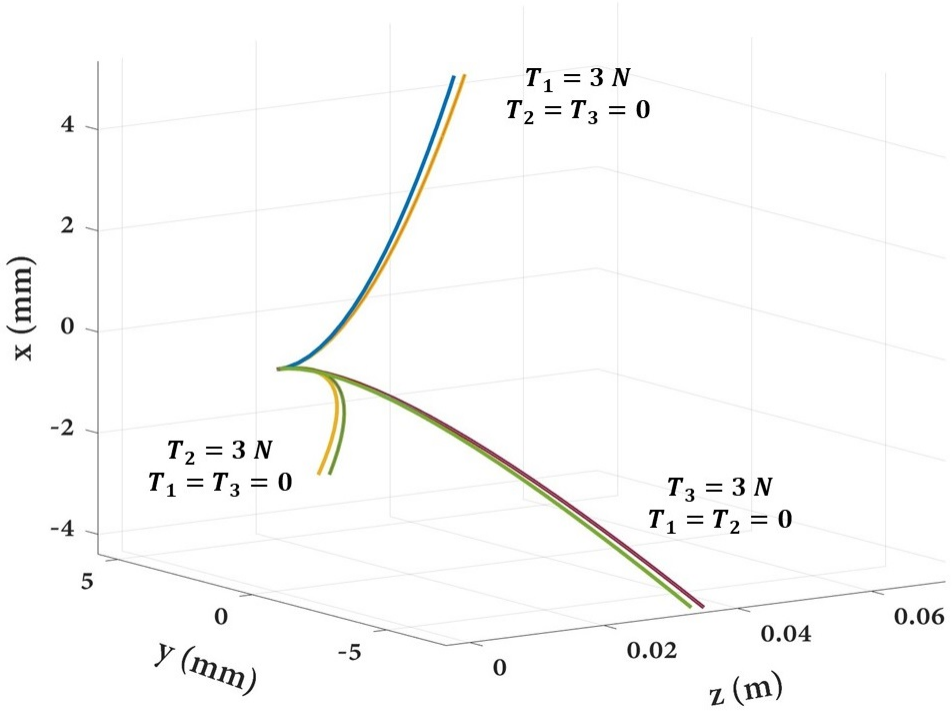

Figure 5.14: 3D Deformation of the soft robot.

soft robot, as simulated through the implementation of the Cosserat rod model. The individual X and Y components corresponding to each case are presented in Figures 5.15- 5.17. It is evident that upon exerting tension along the x-axis, the Y displacement component approaches insignificance. Conversely, in scenarios where the remaining two tendons were pulled, each separated by an angular span of 120°, the Y displacement components exhibit a symmetrical opposition to one another.

The findings outlined in this research enhanced the understanding of integrating air pressure into the Cosserat rod model simultaneously by the presence of the tendon tensions. This integration is achieved firstly by encompassing this pressure within the framework of internal forces and moments, and secondly, by accounting for the force generated at the cap of the soft robot, resulting from its internal pressure. By incorporating pressure into the internal forces and moments of the Cosserat rod model, this study not only addresses an important aspect of soft robot mechanics but also enriches the model's accuracy and predictive capabilities.

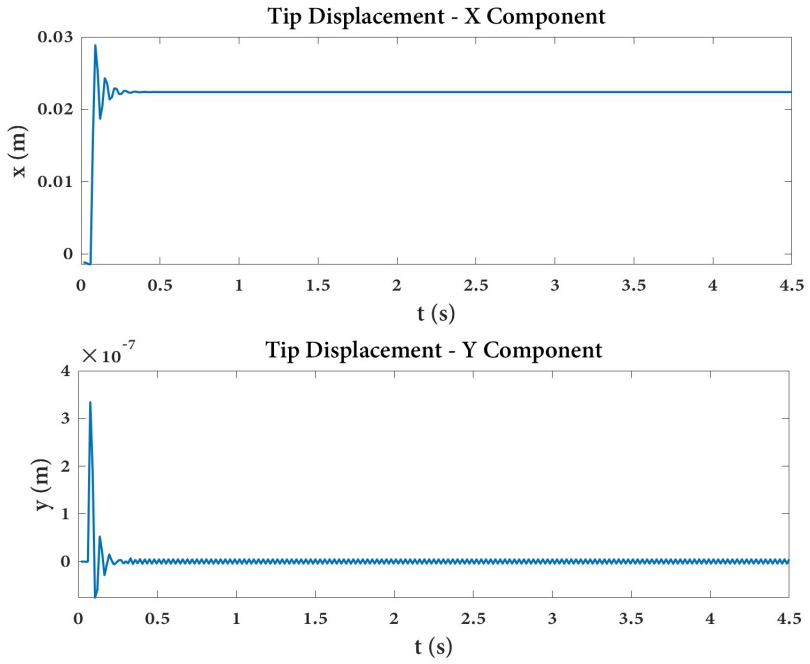

Figure 5.15: X and Y components of the tip displacement when the tension in a single tendon (T_1) is set to 3 N, while the tension in the other tendon is set to zero.

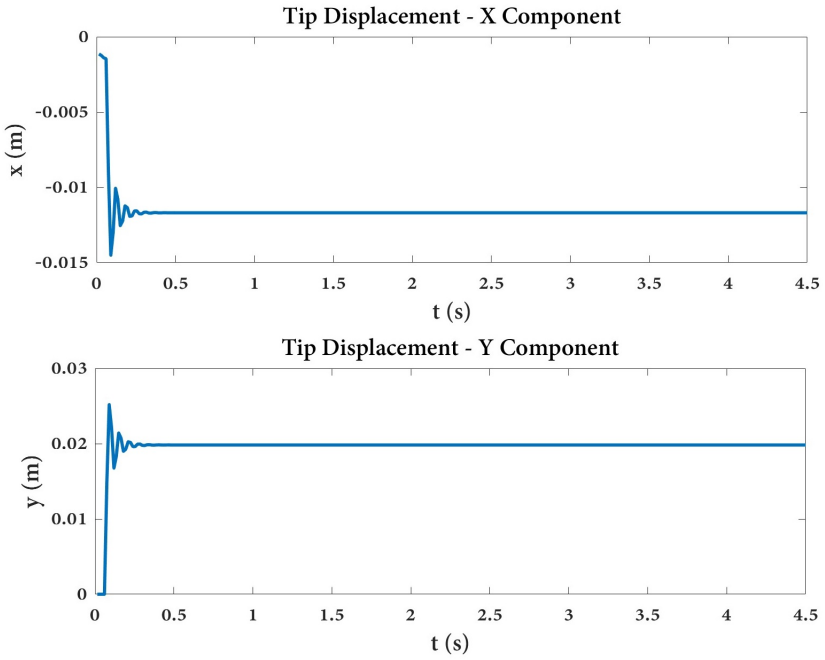

Figure 5.16: X and Y components of the tip displacement when the tension in a single tendon (T_2) is set to 3 N, while the tension in the other tendon is set to zero.

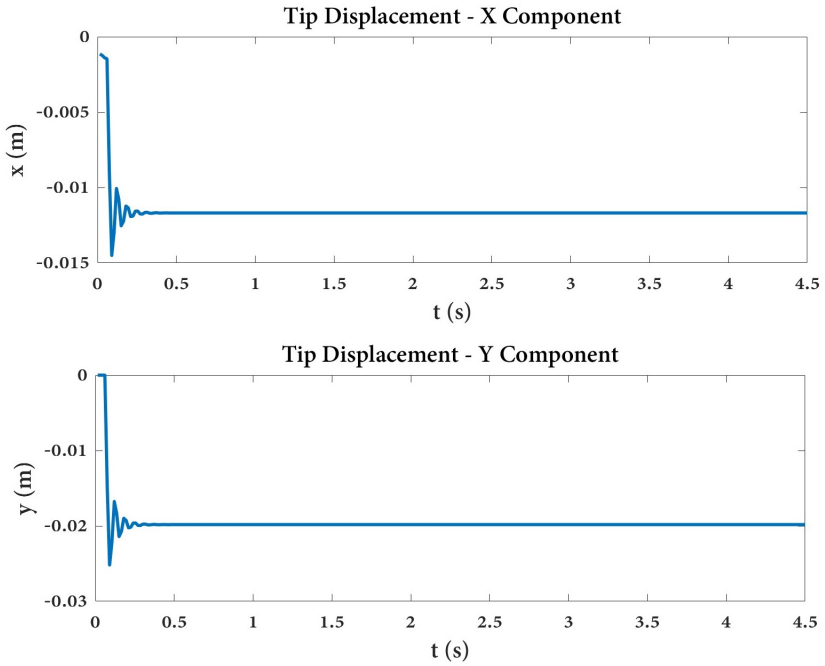

Figure 5.17: X and Y components of the tip displacement when the tension in a single tendon (T_3) is set to 3 N, while the tension in the other tendon is set to zero.

5.4 Summary

This study presented a dynamic formulation of the Cosserat rod in the context of a hybrid-actuated soft robot, with a focus on predicting its deformation under varying pressures and tendon tensions to be used in robot-assisted cardiac ablation. By incorporating the effects of internal pressure into the dynamic formulation, this approach extends the existing literature in this field. The accuracy of the proposed model was confirmed through experimental validation across multiple scenarios. The model formulated in this study can be subsequently applied for implementing model-based control of the soft robot. In the subsequent step, the geometry of the soft robot's root was optimized to mitigate unnecessary side deformation and increase the axial exertion load. This optimization process entailed seeking a compromise between the offset of the tendon and the aspect ratio of the soft robot. Advanced computational techniques, such as FEA and optimization algorithms, were utilized to progressively refine the geometry of the soft robot's root. The ultimate objective of this optimization endeavor was to develop a soft robot with enhanced structural integrity, augmented load-bearing capacity, and superior controllability.

Author Contributions

Conceptualization, M.R. and A.H.; methodology, M.R. and A.H.; software, M.R. and A.H..; validation, M.R.; formal analysis, M.R.; investigation, M.R.; resources, J.D. and A.H.; data curation, M.R.; writing—original draft preparation, M.R.; writing—review and editing, M.R., J.D., and A.H.; visualization, M.R.; supervision J.D.; project administration, A.H.; funding acquisition, J.D..

Chapter 6

Design Optimization of a Hybrid-Driven Soft Surgical Robot with Biomimetic Constraints

The current study investigated the geometry optimization of a hybrid-driven (i.e. a combination of air pressure and tendon tension) soft robot for use in RMIS. Soft robots, made of compliant materials, have gained popularity in surgical interventions due to their dexterity and safety. The study aimed to design a catheter-like soft robot to improve its performance by minimizing radial expansion during inflation and increasing the force exerted on targeted tissue. To do so, FEA was employed to optimize the soft robot's geometry, considering a multi-objective goal function that incorporated factors such as chamber pressures, tendon tensions, and cross-sectional area. To accomplish this, a cylindrical soft robot with three air chambers, three tendons, and a central working channel was considered. The air chambers and tendon routes were separated angularly by 120° in the cross-section of the soft robot. Then, the dimensions of the soft robot, including the length of the air chambers, the diameter of the air chambers, and the offsets of the air chambers and tendons, were optimized to minimize the goal function in an in-plane bending scenario. To accurately simulate the behavior of the soft robot, Ecoflex 00-50 samples were tested based on ISO 7743, and a hyperplastic model was fitted on the compression test data. The FEA simulations were performed

using the Response Surface Optimization (RSO) module in ANSYS® software, which iteratively explored the design space based on defined objectives and constraints. Using RSO, 45 points of experiments were generated based on the geometrical and loading constraints. During the simulations, tendon force was applied to the tip of the soft robot, while simultaneously, air pressure was applied inside the chamber. Following the optimization of the geometry, a prototype of the soft robot with the optimized values was fabricated and tested in a phantom model, mimicking real surgical conditions. The results showcased an enhancement in the performance of the soft robot, as indicated by decreased actuation effort and radial expansion. This advancement led to improved control over the soft robot while additionally minimizing unnecessary cross-sectional expansion. The study demonstrated the effectiveness of the optimization methodology in refining the soft robot's design and highlighted its potential for enhancing surgical applications.

6.1 Introduction

The applications of soft robots in the context of MIS have experienced considerable growth owing to their distinct capabilities, which arise from their compliant materials [132] typically exhibiting Young's modulus within the megapascal range [133, 134]. The mechanical properties of the soft robots were found to bear a close resemblance to human skin [39, 134], thereby introducing a heightened level of safety to surgical procedures. Considerable attention has been given to this domain due to the extensive array of soft materials that have become accessible in recent times [3], enabling the creation of highly agile robots equipped with capabilities surpassing those of rigid counterparts [135]. In addition, soft robots have demonstrated promise across a wide range of applications [40, 23], such as RMIS [9, 136], cardiac mapping catheters [137], soft sensors [138, 77, 75, 79], cardiac ablation [139] and rehabilitation [140], because they are inherently safe [141] and act better at absorbing dynamical loads and shock [142].

The medical field recognized the need for the creation of instruments that could operate with efficiency in environments characterized by lack of structure and constant change, while also being able to navigate obstacles [143]. It became highly desirable for a robotic structure to possess the

capability of transitioning easily from a soft state, allowing for easy insertion, to a stiff state, facilitating the transmission of force upon reaching the intended target tissue. As a response to this demand, a hybrid-driven soft robot emerged as a promising and effective solution [144].

Extensive research has been conducted in the field of soft robotics to explore various types of actuation mechanisms. Among these mechanisms, fluid actuation, specifically pneumatic actuation [145], has received considerable attention due to its various advantages, including lightweight construction, rapid response time, and high output torque. However, one limitation associated with fluid-driven mechanisms is the complexity of the pneumatic or hydraulic control system. These systems are characterized by a substantial volume and weight, posing significant challenges in the quest to miniaturize the entire soft manipulator system [40]. The use of cable-driven mechanisms [13] has been investigated as an alternative actuation mode. It allows for the transmission of driving force over long distances, which in turn ensures a low moment of inertia for the manipulator. However, the implementation of cable-driven actuation presents challenges in achieving miniaturization, primarily due to the necessity of motors and cable retracting and releasing devices. On the other hand, EAP-driven actuation has gained attention due to its various characteristics, including lightweight construction [146], high energy density, and ease of miniaturization. Nonetheless, this mode also encounters specific challenges, such as the risk of material damage from high-level voltage, limited load capacity, and low control accuracy. Another potential actuation mode is based on shape memory materials, which offer a miniaturized structure with a relatively sufficient torque [147]. However, this mode relies on phase changes caused by heating, resulting in slower response speeds and restricted control patterns. These limitations hinder its control accuracy and restrict its potential application areas. Within the medical field, electromagnetic-driven actuation has demonstrated promise. Recently, millimeter-scale miniaturization of electromagnetic-driven soft robots has been achieved [148]. However, this mode of actuation necessitates complex external equipment to generate a stable magnetic field for motion control.

To overcome the limitations associated with individual actuation modes, researchers have conducted investigations into a hybrid-driven mode. This mode involves combining two or more distinct drive modes to enhance the load capacity and control accuracy of the soft manipulators. One example of such a hybrid-driven mode is the combination of the fluid-driven mode and the cable-driven

mode. The fluid-driven mode demonstrated a favorable characteristic in terms of pressure bearing but exhibited relatively weak performance in tensile bearing. Conversely, the cable-driven mode offered robust tensile resistance but lacked the ability to withstand pressure. By integrating these two distinct drive modes, soft manipulators can benefit from both pressure-bearing and tensile-bearing properties, resulting in increased load capacity and improved position control accuracy. Overall, hybrid modes combine the complementary strengths of different actuation mechanisms. For instance, Kang et al. [149] conducted a study on a pneumatic soft robot with embedded tendons, illustrating the application of hybrid actuation. Also, the research aimed to achieve variable stiffness through hybrid actuation, drawing inspiration from the approaches explored by Yin et al. [150] in their design of a soft gripper with a wide range of tunable stiffness. They achieved this objective by employing a hybrid actuation system that integrated tendon-spring and air pressure mechanisms. Similarly, Shahid et al. [151] developed a soft composite finger with adjustable joint stiffness using a hybrid actuation approach combining cable tension and air pressure. Furthermore, Roshanfar et al. [70, 69, 68] developed a continuum model and prototype of a tendon-air hybrid actuated soft robot based on the Cosserat rod model, specifically designed for applications in the field of RAMIS.

Inspired by nature [152], soft robots have provided innovative solutions for medical interventions [123]. Within the medical field, soft robots have found wide applications as flexible tubes, commonly referred to as catheters, for MIS. Currently, rigid materials are utilized for the end effectors of catheters [153], which can potentially harm patients during the insertion process. As an alternative, soft robots have been proposed to replace or enhance the existing catheters in MIS such as cardiothoracic endoscopic surgery [43], abdominal surgery [154], and bronchoscopy [155]. Figure 6.1 provided an illustration of a hybrid-driven soft surgical robot used for intra-bronchial intervention, serving as a representative use case.

In terms of definition, a soft robot can be described as a continuum robot capable of bending continuously, providing virtually infinite DOF [2]. Several studies have been carried out to investigate the kinematics and dynamics of soft robots [53, 87]. Subsequently, control analyses were performed using mechanistic-based models [80] as well as learning-based models [13, 156, 157]. However, designing an optimal soft robot remains a challenging task in the field. This study focused on optimizing the geometry of catheter-like pneumatically actuated tendon-driven soft robots

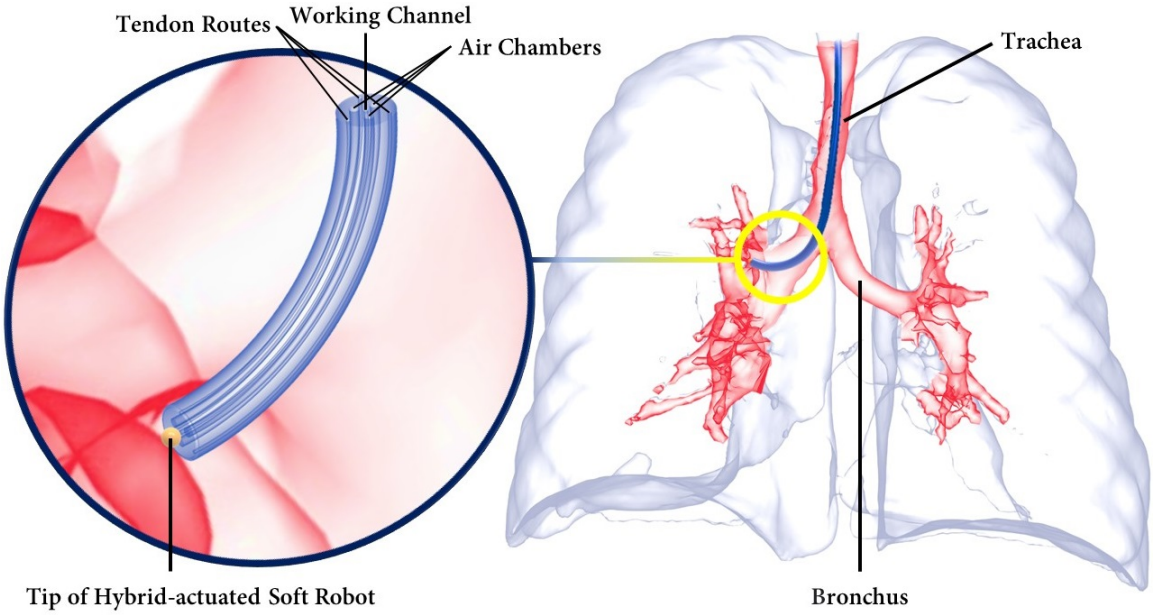

Figure 6.1: The use of a hybrid-driven soft surgical robot inside the lungs during intra-bronchial intervention.

for use in RAMIS. To achieve this, a cylindrical soft robot with three air chambers, three tendons, and a central working channel is considered. The cylindrical shape has been proven to be the most effective geometry for intra-vessel insertion applications. The dimensions of the soft robot, including the air chambers' length, the diameter of the air chambers, and the offsets of the air chambers and tendons, were optimized to minimize the goal function. Developing an optimized model for soft robots is an iterative process that begins with defining objectives, variables, and constraints [158]. Section 6.2 provided the necessary requirements for the design optimization of a hybrid-driven soft robot, taking into account the constraints associated with each specific surgical task. Additionally, the material modeling of silicon for FEA simulations is discussed. Following the presentation of results and discussion in Section 6.3, an example of a robot-assisted intervention using the optimized geometry of the hybrid-driven soft robot was demonstrated as a representative case.

Moreover, to ensure clarity of the hybrid-driven system, the architectural design of the hybrid air-tendon-driven soft robot was depicted in Figure 6.2. This design consisted of two distinct modules: the pneumatic module and the tendon module, both of which were interconnected with the software control module. Each tendon was independently actuated by its own Direct Current (DC)

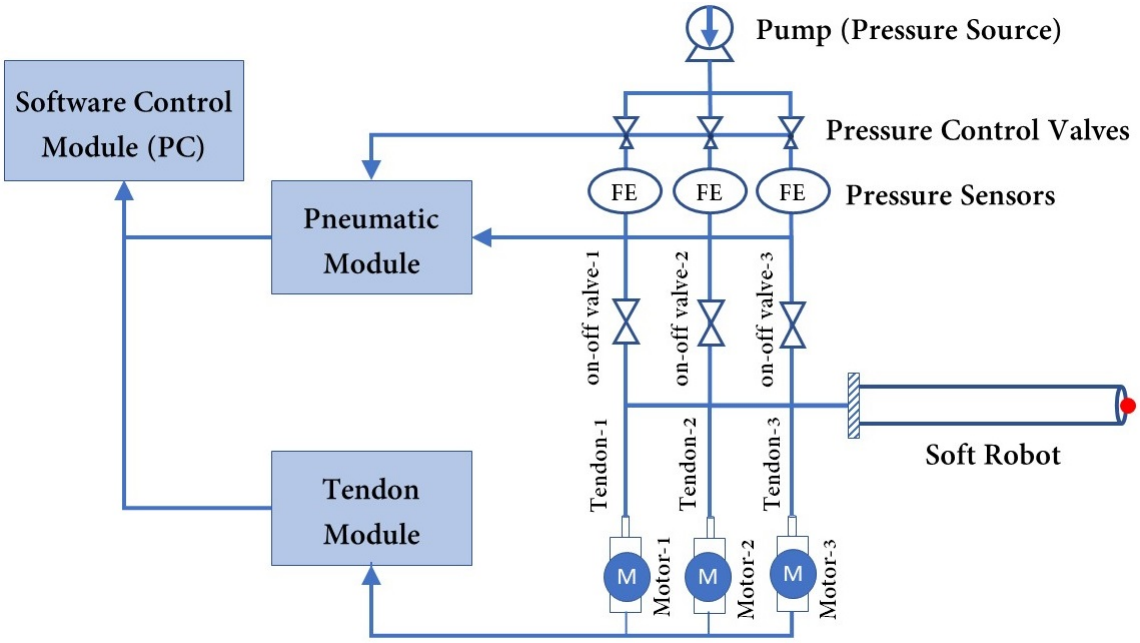

Figure 6.2: Setup architecture of hybrid air-tendon driven soft robot.

brushless motor, and each air chamber was activated separately and controlled using a pressure controller. The tension in the tendons was measured by evaluating the torque exerted on the pulley attached to the motor shaft, while the pressure levels were directly monitored through pressure sensors.

6.2 Materials and Methods

6.2.1 Optimization Model

Design Objectives

The design objective of this study was to achieve the desired mechanical behavior of a hybrid-driven soft robot. Specifically, the investigation focused on the one-degree bending deformation of the soft robot, taking into account the effects of a single air chamber actuation and corresponding tendon tension. The primary aim was to minimize the required actuation effort, taking into account the input pressure and tendon tension, while simultaneously reducing the radial expansion of the soft robot. By achieving 90° bending, the objective was to facilitate greater control over the robot's

deformation while reducing the cross-sectional expansion.

To accomplish this objective, a specific setup was employed. The soft robot's deformation was controlled by inflating a single air chamber while simultaneously pulling a single tendon, thereby causing bending in a 2D plane. It is important to note that this particular objective can be described as a form of "multi-objective optimization," given the simultaneous consideration of multiple variables. In order to mathematically formulate this objective, various parameters were taken into account. These included the input air pressure, tendon tension, and the radial expansion of the soft robot. By formulating the objective in this manner, the study aimed to establish an optimal configuration for achieving the desired mechanical behavior while minimizing the goal function. The goal function was formulated as:

$$G = w\left[\left(\frac{P_{ch}}{P_{max}}\right)^2 + \left(\frac{T_t}{T_{max}}\right)^2\right] + (1-w)\left(\frac{A}{A_0} - 1\right)^2 \tag{81}$$

where G represents the goal function to be minimized by optimal geometry. Additionally, the variable w was used to denote the weight factor ($0 \leqslant w \leqslant 1$), which determined the relative significance of the actuation effort (the first term in (81)) or radial expansion (the second term in (81)) based on the specific surgical application.

The air pressure within the chamber of the soft robot was denoted by P_{ch}, while the tension in each tendon was represented by T_t, which was connected to the tip of the soft robot. The maximum values that could be obtained from the hardware, namely the air pump and motors, were defined as P_{max} and T_{max}, respectively. Also, A_0 and A are the cross-sectional areas of the soft robot before and after the deformation, respectively. The inclusion of the $(A/A_0 - 1)^2$ term in (81) was necessary for two reasons. Firstly, a previous study [68] demonstrated that the Cosserat rod model employed to describe the deformation of the soft robot did not account for the radial expansion of the soft robot during inflation. As the pressure inside the air chambers increased, the disparity between the model and experimental results also increased. Therefore, the $(A/A_0 - 1)^2$ term was introduced to capture this radial expansion effect. Secondly, the absence of this term would have made the solution to the optimization problem obvious. Without considering the impact of the radial expansion, increasing the offset of air chambers and tendons near the wall edge would have led to minimal actuation effort.

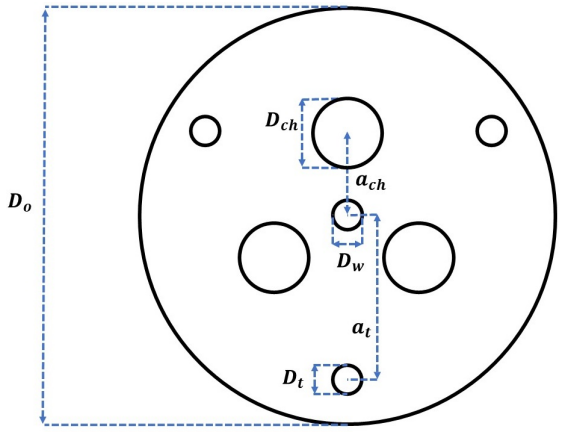

Figure 6.3: Cross-section of the soft robot: D_w represents the diameter of the working channel, D_{ch} is the diameter of the air chambers, D_t is the diameter of the tendon passes, D_o is the outside diameter of the soft robot, and a_{ch} and a_t represent the offset of the air chambers and tendon passes from the center of the cross-section, respectively.

By including the $(A/A_0 - 1)^2$ term, the optimization problem becomes meaningful and realistic, accounting for the trade-off between actuation effort and radial expansion during the soft robot's deformation.

Design Variables

Generally, design variables refer to the geometry, material, and type of actuation employed in the development of a hybrid-driven soft robot [158]. In this study, the material and type of actuation remained constant throughout the optimization process. Consequently, it becomes imperative to optimize the soft robot's geometry, including parameters such as the length and diameter of the air chambers, and chamber and tendon's passes offsets from the center, to fulfill the desired design objective. To comprehensively explore the design space including all variables, it is necessary to consider all feasible design candidates for each particular task. For the sake of clarity, Figure 6.3 illustrated the cross-section variables of the hybrid-driven soft robot for this study. Within the soft robot's cross-section, D_w denotes the diameter of the working channel, D_{ch} represents the diameter of the air chambers, D_t corresponds to the diameter of the tendon passes, and D_o is the outside diameter of the soft robot. The outer diameter of the soft robot will be assigned a specific value, dictated by the requirements of each clinical intervention. Due to this, its value remained the same

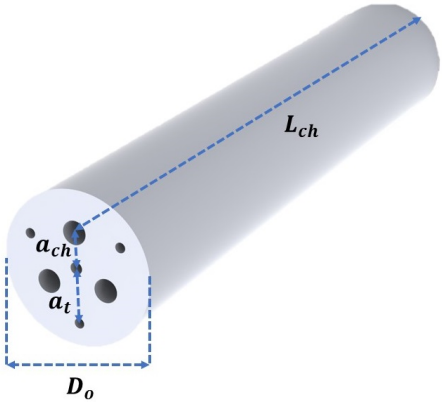

Figure 6.4: 3D shape of the soft robot: L_{ch} represents the length of air chambers.

throughout the iterations to find the optimum geometry. Furthermore, a_{ch} and a_t denote the offset of the air chambers and tendon passes, respectively, from the center of the cross-section. Additionally, L_o and L_{ch} represent the outside length of the soft robot and the length of the air chambers, respectively. Throughout the optimization process, the lengths of all three air chambers remained equal to each other, implying that $L_{ch}^{(1)} = L_{ch}^{(2)} = L_{ch}^{(3)}$. Additionally, the diameter of all three air chambers and the diameter of all three tendon passes remained equal to each other, namely, $D_{ch}^{(1)} = D_{ch}^{(2)} = D_{ch}^{(3)}$ and $D_t^{(1)} = D_t^{(2)} = D_t^{(3)}$, respectively. Moreover, the length of the tendon passes is equal to L_o, ensuring that the tendons are consistently affixed at the tip of the soft robot. The number of air chambers and tendons is also fixed at three, evenly distributed within the cross-section, as a minimum of three inputs is required to maneuver the soft robot's tip within 3D space.

Design Constraints

In order to ensure the effective utilization of soft robots in interventional medical applications, the consideration and resolution of two distinct categories of requirements were found to be essential: technical requirements and clinical requirements. Furthermore, it was observed that soft robots employed in interventional medical applications must conform to the unique demands and specifications associated with diverse clinical procedures. This involves the careful examination of factors such as the dimensions and shapes of anatomical structures, the nature of the interventions being conducted, and the expected outcomes. Accommodating various clinical scenarios necessitates the

incorporation of modularity and customization options, thereby enabling the customization of soft robots to suit specific medical interventions and patient requisites.

Technical Requirements Technical requirements cover a broad range of factors related to the design, functionality, and operation of soft robots. These soft robots must possess specific mechanical properties enabling them to perform delicate and precise movements within the human body. Key attributes such as flexibility, compliance, and adaptability are essential for soft robots to navigate complex anatomical structures without causing damage or discomfort. In particular, the technical requirements encompass engineering constraints and manufacturing limitations. For instance, it has been observed that when using a normal 3D-printed mold approach to prototype the soft robot, the minimum diameter of a cavity should be at least 1 mm [70]. Therefore, the following condition holds:

$$D_{ch} \geqslant 1 \text{ mm} \tag{82}$$

$$D_t \geqslant 1 \text{ mm} \tag{83}$$

$$D_w \geqslant 1 \text{ mm} \tag{84}$$

Additionally, to ensure proper inflation and prevent the "ballooning effect", soft robots should have a minimum wall thickness of 1 mm [159]. This can be expressed as:

$$t_w = R_o - R_t - a_t \geqslant 1 \text{ mm} \tag{85}$$

where t_w represented the wall thickness, and R_o and R_t denoted the outside and tendon pass radius, respectively. Similarly, there should be at least a 1 mm space between the working channel and the air pressure and tendon passes. By adhering to these technical requirements, the design and fabrication of soft robots could be optimized, ensuring their feasibility for prototyping.

Clinical Requirements Clinical requirements refer to the operational capabilities of a soft robot within a specific surgical procedure. Surgical instruments are typically subject to constraints in their physical dimensions due to the nature of their operating environment. For example, MIS involving

the oral cavity and esophagus necessitate a surgical robot with a feature size of less than 30 mm in diameter [160]. Similarly, intra-vascular procedures require a diameter of less than 6 mm [9], while endoscopic applications mandate an instrument diameter of less than 15 mm [161]. Achieving further miniaturization often entails enabling the soft robot to penetrate vessels more deeply and extensively. Throughout this study, the outer diameter of the soft robot was assumed constant:

$$D_o = 15 \text{ mm} \tag{86}$$

While it is essential for a soft robot to be of adequate length for intraluminal procedures, e.g., typically ranging from 1.5 to 2 m [3], only the active tip of the robot (actuated part) was studied:

$$L_o = 84 \text{ mm} \tag{87}$$

which consisted of 80 mm for the body and 4 mm for the cap. To adapt to the majority of the commercially available endoscopic micro-cameras, (e.g., OdySight.AI, Israel), the internal diameter of the working channel was also fixed at 1.2 mm. For different applications, the endoscope's field of view (FOV) may vary. Currently, in the upper and lower gastrointestinal endoscopy, the standard FOV is 170°. However, in applications where the endoscope was constrained to a narrow lumen with no possibility of moving away from the longitudinal axis, cameras with an FOV of 120° or less are commonly used and provided adequate vision [133]. In the current study, the required bending angle θ of the soft robot under maximum actuation was selected to be 90° that combined with a 120° FOV would adequately cover a total FOV of 360°.

$$\theta \geqslant 90^\circ \tag{88}$$

6.2.2 Material Modeling

Silicone rubber is the most commonly used material for soft pneumatic actuators as it is highly flexible and can undergo large strains. To adequately characterize their mechanical behavior, hyperelastic models are employed. In this study, silicone rubber is considered to be isotropic and incompressible, while inelastic phenomena such as viscoelasticity and stress-softening are neglected

[162]. The 3rd-order Yeho model was selected because it is applicable to a much wider range of deformation and can predict the stress-strain behavior in different modes based on data collected from one simple uniaxial test. According to the Yeoh model, the strain energy density function is [163, 90]:

$$W = \sum_{i=1}^{3} C_{i0}(I_1 - 3)^i \tag{89}$$

where the energy function W is defined as the amount of elastic energy stored in a unit volume of material, C_{i0} are the material constants, and I_1 is the principal invariant defined as follows:

$$I_1 = \lambda^2 + \frac{2}{\lambda} \tag{90}$$

where the λ is the principal stretches that represent the deformation of a differential cubic volume element in relation to the principal axes of a Cartesian coordinate system [164]. The corresponding stress-stretch function (principal Cauchy stresses) of (89) is:

$$\sigma = 2\left(\lambda - \frac{1}{\lambda^2}\right)\frac{\partial W}{\partial I_1} \tag{91}$$

The determination of the material properties, specifically C_{10}, C_{20}, and C_{30} as indicated in (89), requires the employment of uniaxial testing. In this study, the soft robot was subjected to simulation and prototyping, employing Ecoflex 00-50 (Smooth-On Inc., PA, USA). To obtain the material constants, a uniaxial compression test was conducted on three samples, according to the guidelines outlined in ISO 7743 [165]. After the curing of the samples, their final dimensions fell within the tolerances specified in ISO 7743, with a diameter of 29 mm $\pm$ 0.5 mm and a height of 12.5 mm $\pm$ 0.5 mm. The compression test, depicted in Figure 6.5, was carried out using the Bose electroforce universal testing machine (UTM), following the protocols defined in ISO 7743. Each sample was subjected to a cyclic load, and the fourth cycle was utilized for extracting the stress-strain curve. Figure 6.6 presents the stress-strain curves obtained from each sample utilized in this study. To establish a comprehensive compression-tension model for Ecoflex 00-50, the compression test results were combined with tension test data from L. Marechal et al. [90]. Figure 6.7 demonstrated

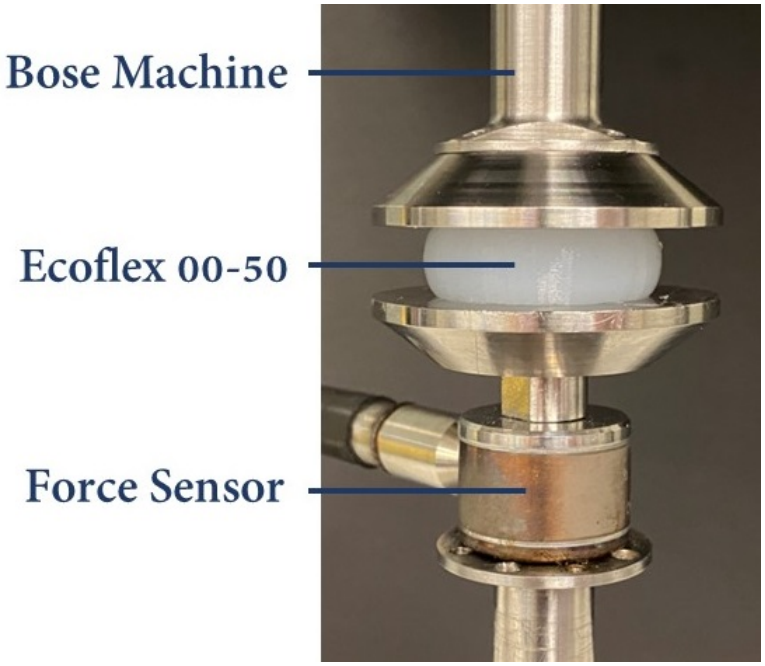

Figure 6.5: Compression test conducted with Bose UTM on the Ecoflex 00-50 samples based on ISO 7743.

Table 6.1: Material constants of the Yeoh model for Ecoflex 00-50.

Model Parameters	C_{10} (MPa)	C_{20} (MPa)	C_{30} (MPa)
With Compression	0.01516	0.00010	-7.39×10^{-8}
Without Compression [90]	0.01385	0.00011	-8.76×10^{-8}

the comprehensive compression-tension engineering stress-strain curve for Ecoflex 00-50. Finally, the material constants required for the Yeoh model in (89) were fitted using the combined dataset, and the resulting constants are presented in Table 6.1.

6.2.3 Design Optimization

There are several analytical approaches to model the deformation of soft robots, like the PCC [53] or the Cosserat rod model [87]. However, due to the nonlinearity of the model, a finite element (FE) model was used to determine the deformation of soft robots under both actuation modalities. Then, the goal function at various design points was measured to find the optimum geometry based on the design constraints. To do so, the FE model of the soft robot with initial dimensions was

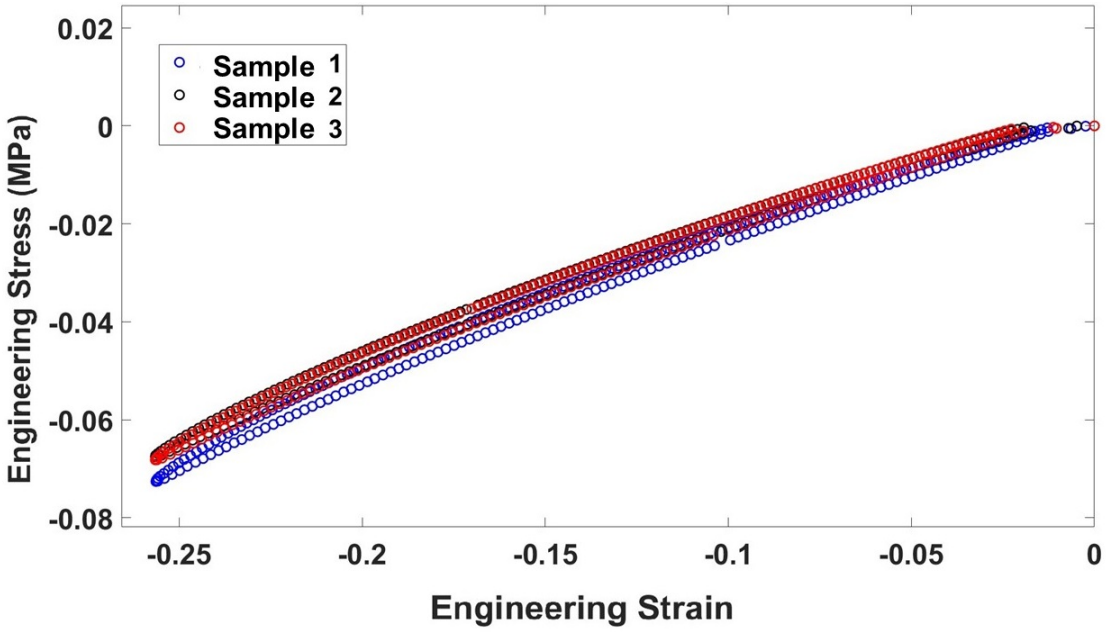

Figure 6.6: Stress-strain curves of compression test obtained from each sample.

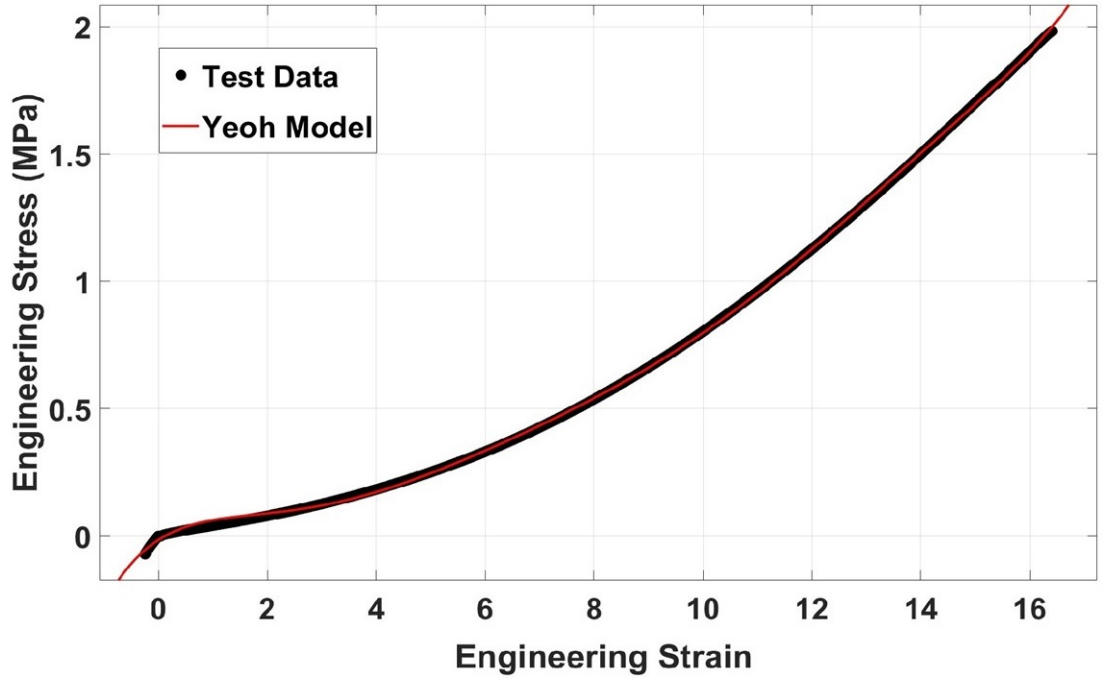

Figure 6.7: Fitted the Yeoh model to comprehensive compression-tension stress-strain dataset. The tension data extracted from [90].

imported in the ANSYS® software. The dimensions that were described in Section 6.2.1 are defined as a parameter, so the geometry of the soft robot will be updated automatically during each iteration. Next, the upper and lower limit for each individual input parameter was defined, and numerical parametric optimization was performed using the RSO module in ANSYS® software similar to the previous studies [72, 74].

During the FE simulations, the hyperelastic material of silicone, based on Table 6.1, was assigned to the soft robot by considering the large deformation of the material. The soft robot was considered as a cantilever beam using Dirichlet and Neumann conditions for establishing the BCs, where the displacements and rotations at the base of the soft robot were fixed. To simulate the robot's deformation, internal air pressure was applied to the inner surface of one air chamber, as well as the cap of the air chamber. Simultaneously, a tendon force was exerted on the tip of the soft robot in the opposite direction. This loading configuration made the soft robot bend in a 2D plane. In this study, all simulations were performed using an Intel Core (TM) i7-10700K central processing Unit (CPU) at 3.80 GHz with 16.0 GB random-access memory (RAM). The deformation of the soft robot was illustrated in Figure 6.8 until it reached 90°. Once it reached 90°, the cross-section deformation was shown in Figure 6.9.

6.3 Results and Discussion

The RSO technique was employed to generate a total of 45 design experiments, which were based on the geometrical constraints and variations of applied loadings. Throughout the simulations, the air pressure was incrementally increased from 12 kPa to 16 kPa, while simultaneously applying a tendon force ranging from 40 mN to 60 mN to the tip of the soft robot. A comprehensive overview of all the 45 design experiment points, along with their respective geometry, pressure, tendon force, and corresponding values for the goal function, can be found in Table 6.2. Subsequently, in adherence to the clinical requirements discussed in Section 6.2.1, design points with bending angles less than 90° were excluded from further consideration. This step ensured that only feasible design point options were pursued. The next objective was to minimize the goal function presented in (81) by utilizing the genetic algorithm (GA) method. The aim was to identify the optimum design point for the soft

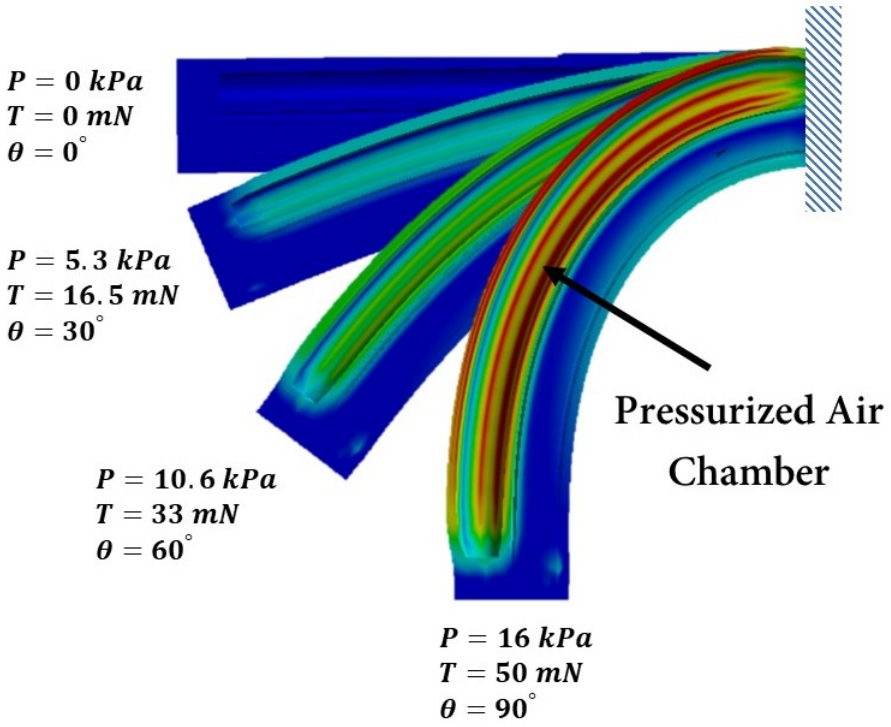

Figure 6.8: 90° bending of the soft robot under the air pressure and tension of its tendon.

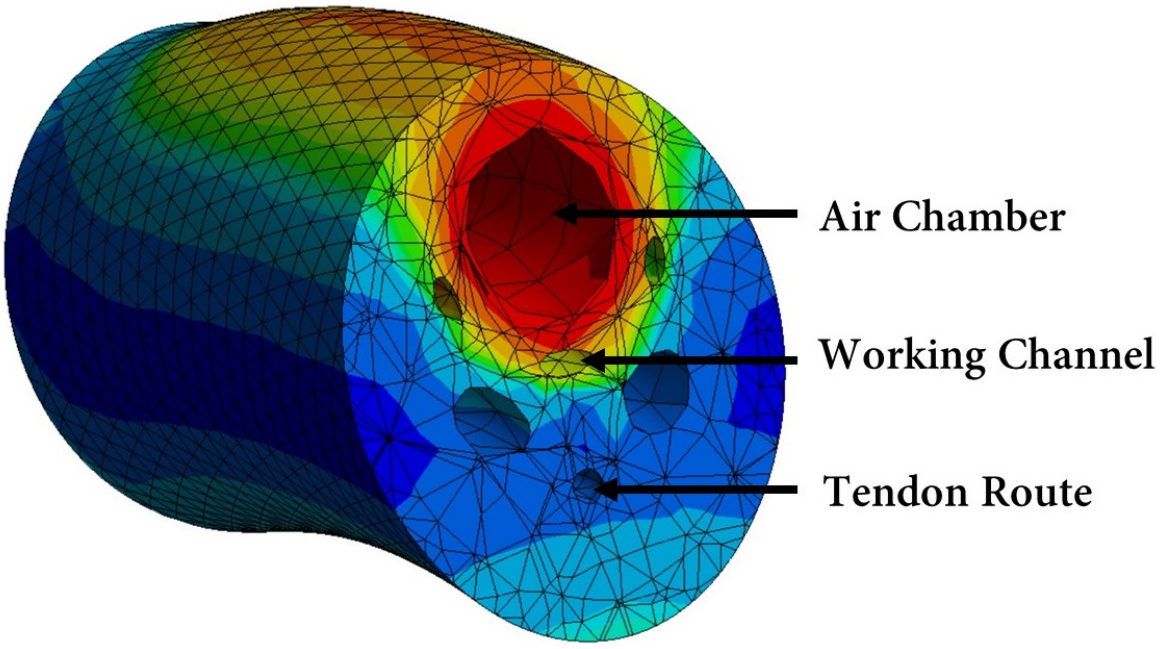

Figure 6.9: The cross-section of the soft robot after deformation.

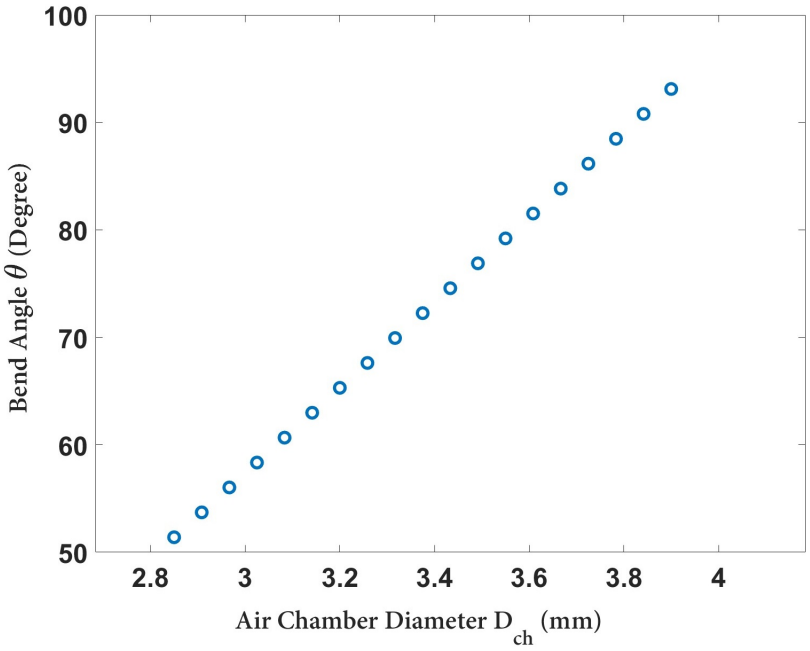

Figure 6.10: Effect of air chamber diameter (D_{Ch}) on bending angle.

robot's tip to achieve a bending angle of 90°. The optimized values derived from this process were subsequently utilized for prototyping the hybrid-driven soft robot. These optimized values can be found in summarized form in Table 6.3.

Figure 6.10 illustrated the variation of the bending angle (θ) with respect to the diameter of the air chamber. As observed, in accordance with expectations, the increase in the diameter of the air chamber leads to a proportional increase in the area term (A) in the equation for PA. Consequently, this results in a larger moment around the central axis of the soft robot, causing it to bend further. Similarly, 6.11 demonstrated that increasing the offset of tendon passages from the center also increased the bending angle. Due to the minimum requirement of a 1 mm wall thickness, the maximum value of a_t was limited to 6 mm. Next, 6.12 illustrated the variation of bending angle with respect to the length of the air chamber (L_{Ch}). Additionally, 6.13 indicated that the effect of the air chamber offset on the bending angle was minimal. Nevertheless, it should be noted that increasing a_{Ch} negatively impacted the "ballooning effect" of the soft robot. It is crucial to consider the placement of the air chamber not close to the edge of the cross-section to avoid unnecessary radial expansion.

Table 6.2: Design points of experiments.

Number	D_{Ch} (mm)	a_{Ch} (mm)	a_t (mm)	L_{Ch} (mm)	F_t (mN)	P_{Ch} (kPa)	θ (Degree)	Goal Function $w = 0.05$	$w = 0.5$	$w = 0.95$
1	3.605	4.273	4.816	68.165	55.780	15.156	114.742	0.274	0.331	0.387
2	3.900	4.100	5.250	72.500	50.000	14.000	108.421	0.211	0.267	0.323
3	3.605	3.927	5.684	68.165	55.780	15.156	107.886	0.183	0.283	0.382
4	3.605	4.273	4.816	76.835	44.220	15.156	105.432	0.223	0.279	0.336
5	3.605	4.273	5.684	76.835	55.780	15.156	104.453	0.151	0.266	0.381
6	3.605	3.927	4.816	76.835	55.780	15.156	99.472	0.102	0.240	0.378
7	3.605	3.927	5.684	76.835	44.220	15.156	98.431	0.157	0.245	0.332
8	3.200	4.100	5.250	72.500	50.000	16.000	89.935	0.103	0.242	0.380
9	3.605	4.273	5.684	68.165	44.220	15.156	85.283	0.132	0.231	0.331
10	3.200	4.100	5.250	72.500	60.000	14.000	81.807	0.045	0.203	0.360
11	3.605	4.273	4.816	76.835	55.780	12.844	81.316	0.095	0.203	0.310
12	3.605	3.927	5.684	76.835	55.780	12.844	80.006	0.054	0.181	0.307
13	3.605	3.927	4.816	68.165	44.220	15.156	79.828	0.092	0.211	0.329
14	3.605	4.273	5.684	68.165	55.780	12.844	74.464	0.047	0.177	0.307
15	3.200	4.400	5.250	72.500	50.000	14.000	73.255	0.064	0.189	0.315
16	3.605	3.927	4.816	68.165	55.780	12.844	71.309	0.036	0.171	0.307
17	2.795	4.273	4.816	76.835	55.780	15.156	70.477	0.073	0.225	0.377
18	2.795	4.273	5.684	68.165	55.780	15.156	69.322	0.043	0.209	0.375
19	3.200	4.100	6.000	72.500	50.000	14.000	67.575	0.047	0.180	0.314
20	3.200	4.100	5.250	72.500	50.000	14.000	66.894	0.044	0.179	0.314
21	3.200	4.100	5.250	80.000	50.000	14.000	66.670	0.054	0.184	0.314
22	2.795	3.927	5.684	76.835	55.780	15.156	66.501	0.029	0.202	0.374
23	3.200	4.100	4.500	72.500	50.000	14.000	65.859	0.044	0.179	0.314
24	3.200	4.100	5.250	65.000	50.000	14.000	64.635	0.043	0.178	0.314
25	2.795	3.927	4.816	68.165	55.780	15.156	61.770	0.027	0.201	0.374
26	3.605	4.273	4.816	68.165	44.220	12.844	60.188	0.060	0.160	0.259
27	2.795	4.273	5.684	76.835	55.780	12.844	60.007	0.030	0.168	0.306
28	3.200	3.800	5.250	72.500	50.000	14.000	59.712	0.033	0.173	0.313
29	3.605	3.927	5.684	68.165	44.220	12.844	59.630	0.047	0.152	0.258
30	3.605	4.273	5.684	76.835	44.220	12.844	58.944	0.046	0.152	0.258
31	2.795	4.273	4.816	68.165	55.780	12.844	57.122	0.029	0.168	0.306
32	2.795	3.927	5.684	68.165	55.780	12.844	55.601	0.021	0.163	0.306
33	3.605	3.927	4.816	76.835	44.220	12.844	54.974	0.035	0.146	0.258
34	2.795	3.927	4.816	76.835	55.780	12.844	53.474	0.020	0.163	0.306
35	2.795	4.273	5.684	76.835	44.220	15.156	53.446	0.045	0.186	0.326
36	3.200	4.100	5.250	72.500	50.000	12.000	53.213	0.028	0.143	0.258
37	3.200	4.100	5.250	72.500	40.000	14.000	51.423	0.042	0.159	0.276
38	2.795	4.273	4.816	68.165	44.220	15.156	50.070	0.048	0.187	0.327
39	2.795	3.927	5.684	68.165	44.220	15.156	46.476	0.029	0.178	0.326
40	2.795	3.927	4.816	76.835	44.220	15.156	45.246	0.027	0.176	0.326
41	2.500	4.100	5.250	72.500	50.000	14.000	44.326	0.021	0.167	0.313
42	2.795	4.273	5.684	68.165	44.220	12.844	39.325	0.026	0.142	0.257
43	2.795	4.273	4.816	76.835	44.220	12.844	38.646	0.035	0.146	0.258
44	2.795	3.927	5.684	76.835	44.220	12.844	37.541	0.020	0.139	0.257
45	2.795	3.927	4.816	68.165	44.220	12.844	33.435	0.019	0.138	0.257

Table 6.3: Optimized dimensions for the hybrid-driven soft robot.

Parameters	Optimized values (mm) $w = 0.05$	$w = 0.5$	$w = 0.95$
D_{ch}	3.49	3.82	3.89
L_{ch}	72.96	74.45	77.33
a_{ch}	3.80	4.37	4.36
a_t	4.57	5.85	5.72

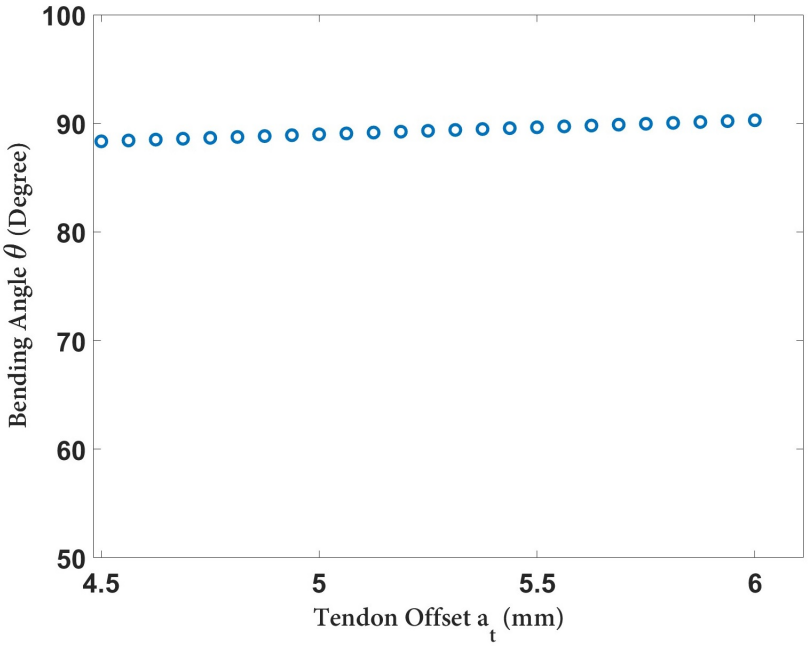

Figure 6.11: Effect of air tendon offset (a_t) on bending angle.

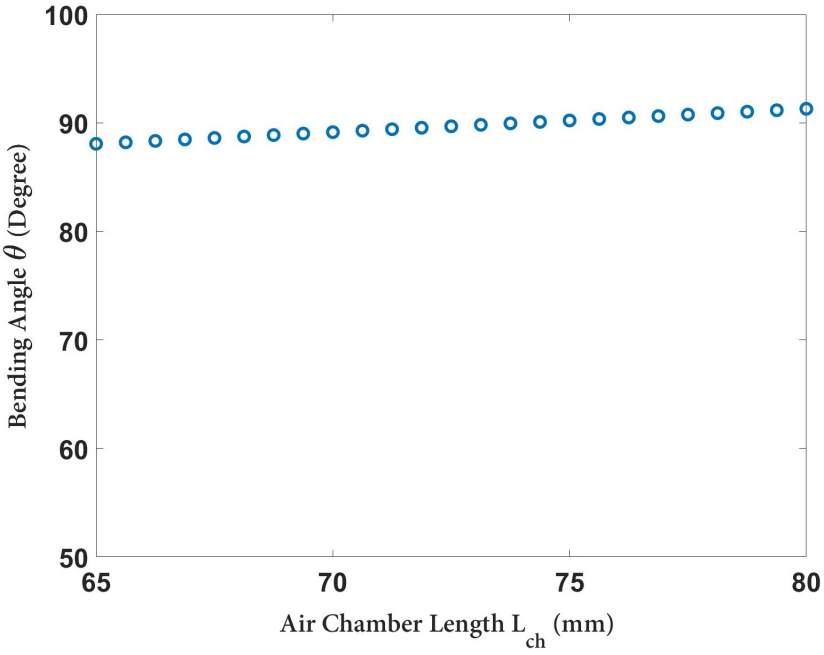

Figure 6.12: Effect of air chamber length (L_{Ch}) on bending angle.

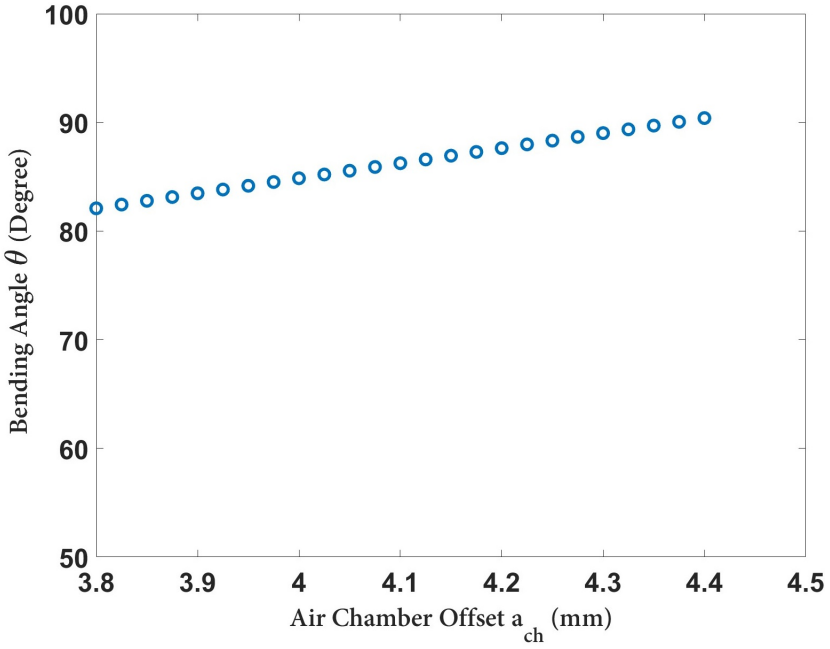

Figure 6.13: Effect of air chamber offset (a_{Ch}) on bending angle.

Figure 6.14 displayed the variation of bending angle (θ) as the air chamber diameter and offset was changed. As could be observed, the air chamber diameter played a significant role in increasing the bending angle. Although increasing the air chamber diameter reduced the required pressure for a certain amount of bending, it also resulted in an increased radial expansion. This antagonistic feature in (81) between the first and second term could be utilized to identify the optimum geometry for minimizing the goal function. Furthermore, Figure 6.15 demonstrated the variation of bending angle when the loading inputs (i.e. tendon force and air chamber pressure) were changed, while other input parameters were set to the optimized values based on Table 6.3. Finally, Figure 6.16 illustrated the outer radial expansion of the soft robot when the air chamber pressure and diameter were varied. It was evident that even with the use of the optimized value, the radius of the cross-section will be increased by approximately 25%.

To demonstrate the performance of a soft robot with optimized values in accordance with the proposed study for robot-assisted intervention purposes, a prototype of a hybrid-driven soft robot was created. This involved the utilization of a cylindrical mold with internal air chambers, tendon

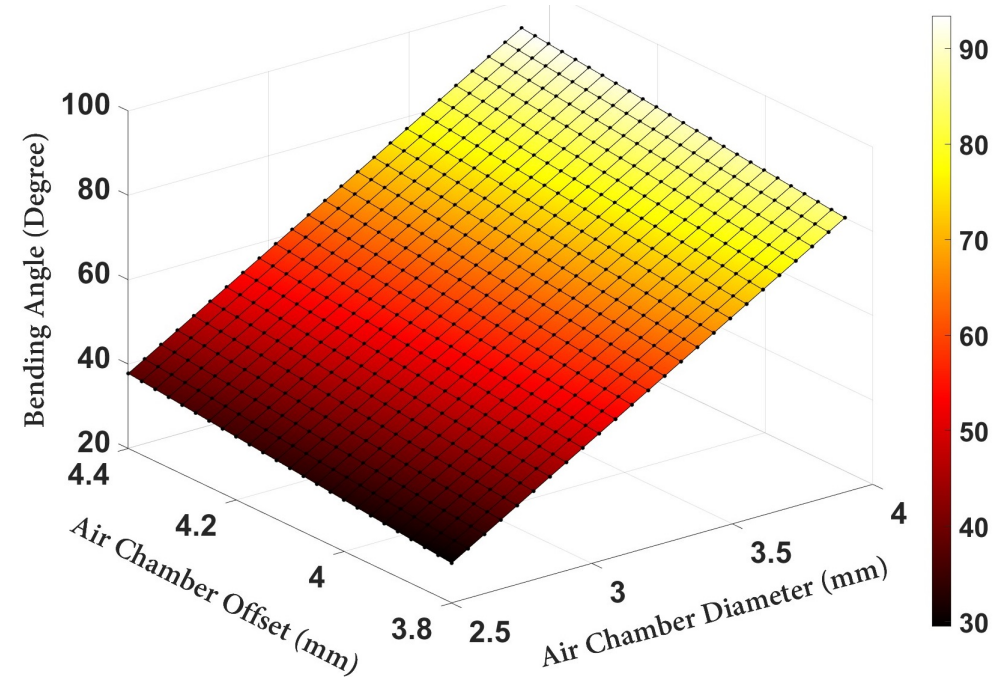

Figure 6.14: Deformation of the soft robot at the optimized parameters: variation of bending angle vs. air chamber diameter and offset.

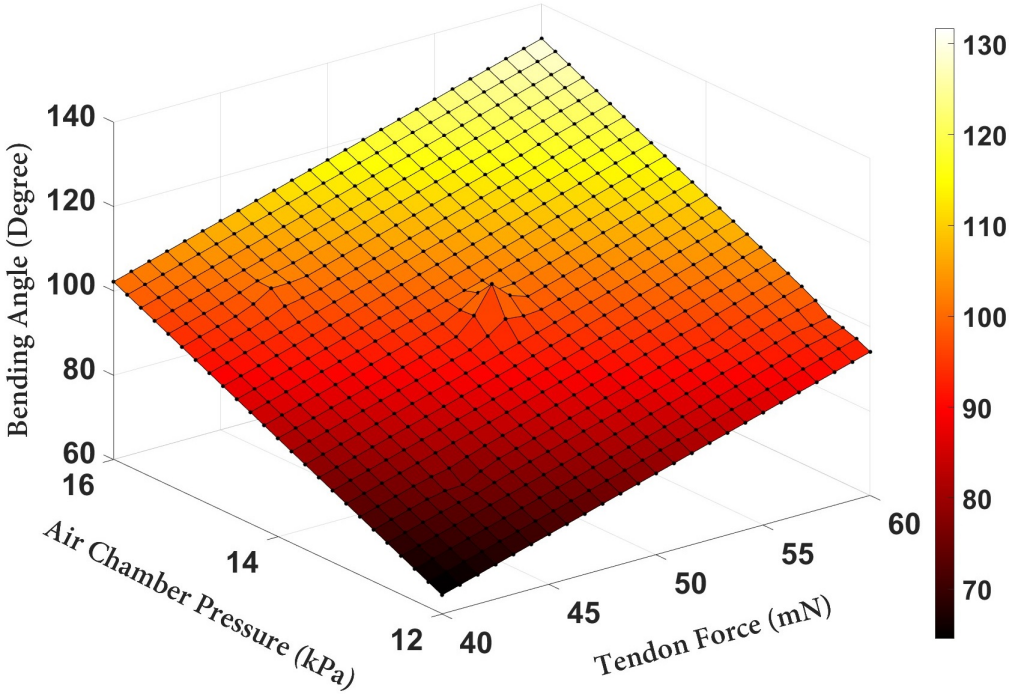

Figure 6.15: Deformation of the soft robot at the optimized parameters: variation of bending angle vs. tendon force and air chamber pressure.

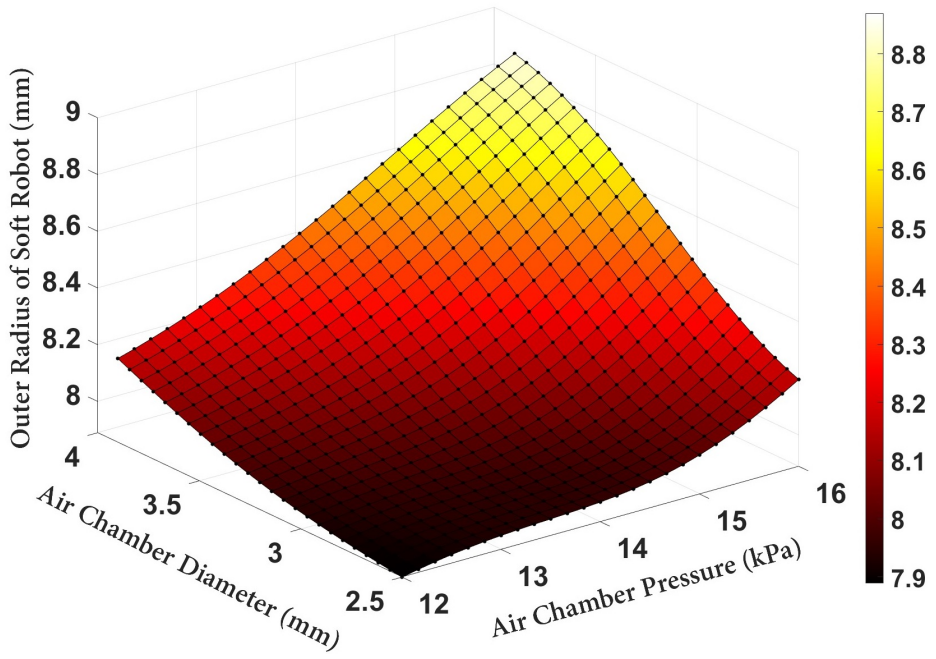

Figure 6.16: Deformation of the soft robot at the optimized parameters: Variation of the outer radius of soft robot vs. air chamber pressure and diameter.

passes, and a central working channel, which was rapidly fabricated using a 3D printer (Replicator+, MakerBot, NY, USA). Figure 6.17 provided an illustration of the mold design employed for prototyping the hybrid-driven soft robot. The mold was designed in three separate parts to facilitate the easy removal of the soft robot body. Upon the successful completion of the mold printing process, two parts of Ecoflex 00-50 silicone were mixed in a 1:1 ratio and subsequently placed in a vacuum chamber for degassing. After eliminating any excess bubbles from the silicon mixture, it was poured into the mold and allowed to cure at room temperature for a period of 12 hours. Once the silicone had fully dried, the soft robot was detached from the mold. Subsequently, a silicone tube was affixed to the base of the soft robot, as depicted in Figure 6.18-(4), to attach it to the tendon module. The material of the tube is stiffer than the distal tip of the soft robot, so by increasing the air pressure inside the chambers, only the soft robot at the tip will be inflated.

In addition, the linear actuator utilized for inserting the soft robot was illustrated in Figure 6.18. This accomplishment was achieved through the installation of a stepper motor (Nema 17) that was affixed to the linear actuator's rail. Moreover, the setup incorporated three brushless DC motors

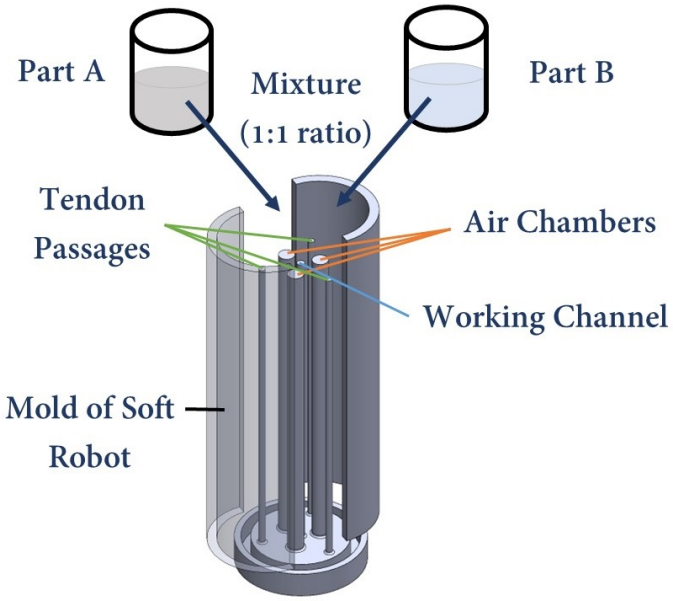

Figure 6.17: Mold design of hybrid air-tendon driven soft robot with central working channel.

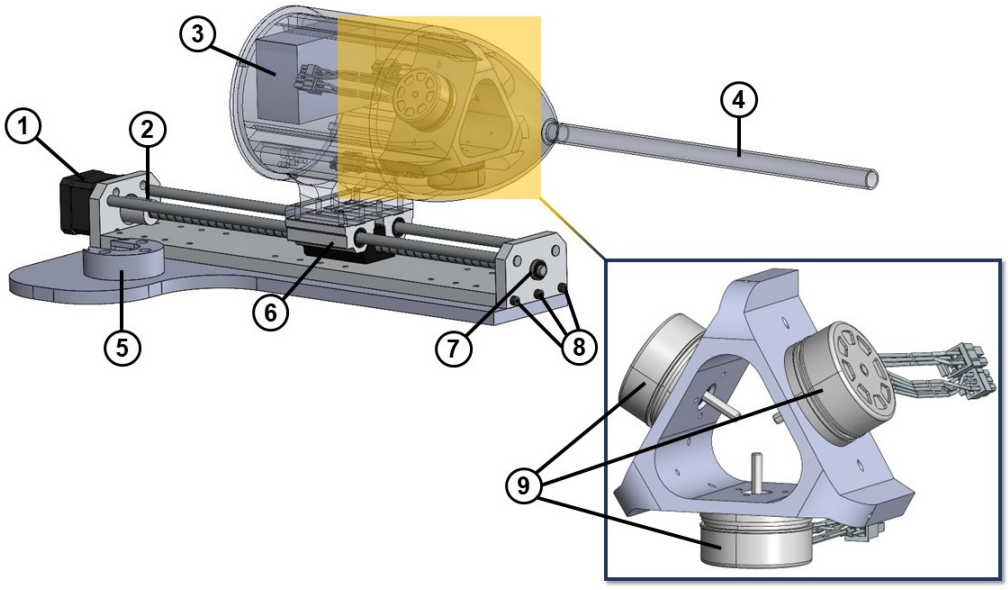

Figure 6.18: Linear actuator of the soft robot: (1) NEMA 17 stepper motor (2) shaft coupler (3) EPOS4 3-axes digital positioning controller of the motors (4) silicone tube (5) holder of the robotic arm (6) double bearing and lead screw (7) bearing (8) screws (9) brushless DC motor with Hall sensors.

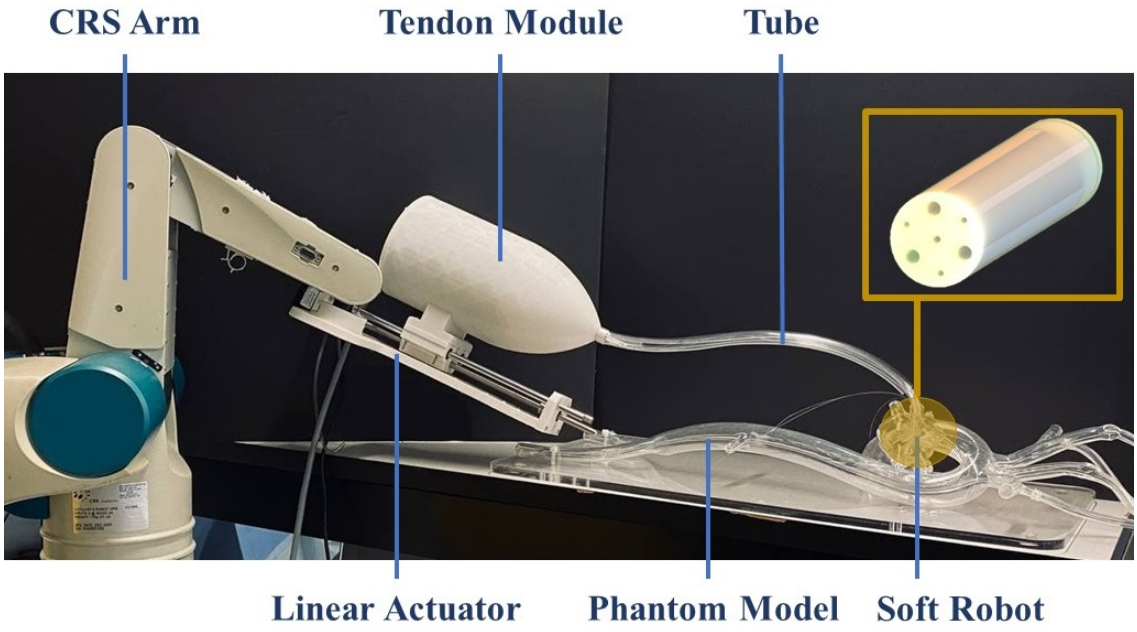

Figure 6.19: An integrated hybrid-driven soft robot prototype utilizing the CRS robotic arm and the phantom model.

(Maxon, EC 45 flat ϕ 42.8 mm, brushless, 60 W, with Hall sensors) along with a digital positioning controller (Maxon, EPOS4 Compact 24/5 Ether CAT 3-axes) to provide the necessary tendon force at the soft robot's tip. To enable the soft robot's rotation, a specially designed holder was employed to attach the linear actuator to the CRS robotic arm. The integration of the soft robot prototype with the CRS robotic arm, as depicted in Figure 6.19, facilitated the insertion of the soft robot into the phantom model. The combination of these components resulted in a versatile and effective system for facilitating robot-assisted intervention in a controlled manner.

6.4 Summary

This paper presented a comprehensive study on the design optimization of a hybrid-driven soft robot for use in RAMIS. The proposed FEA-based method enabled the optimization of the soft robot's geometry, considering various design constraints specific to different clinical tasks. The optimized geometry aimed to reduce actuation effort, improve control, and minimize unnecessary radial expansion. To this end, the study employed a cylindrical soft robot with three air chambers,

three tendons, and a central working channel. The dimensions of the soft robot were iteratively optimized using FEA simulations using the RSO module in ANSYS software. The material properties of the silicon used in the soft robot were determined through experimental testing and hyperelastic modeling. The optimized geometry led to enhanced performance, including improved air pressure control, optimized tendon tension, and reduced cross-sectional expansion. These improvements resulted in decreased actuation efforts and improved the robot's ability to perform delicate and precise interventions. Additionally, the study validated the optimization methodology by fabricating a prototype of the optimized soft robot and deploying it in a phantom model that closely mimicked the anatomical environment encountered during minimally invasive interventions. The practical evidence obtained from this realistic setting further confirmed the effectiveness of the optimization approach. The incorporation of FEA simulations, design constraints, and a multi-objective goal function allowed for the systematic refinement of the soft robot's design. Future work in this area will focus on additional optimizations, considering factors and constraints to enhance the soft robot's versatility and expand its applications in RAMIS. Specifically, the study suggests conducting position control experiments to achieve the desired trajectories of the soft robot's tip and adjusting the stiffness of the soft robot based on clinical needs.

Author Contributions

M.R and A.H contributed to the conceptualization and design of the study. J.D is the academic supervisor. M.R performed the methodology, formal analysis, investigation, data curation, design modeling, FEA simulations, and prototyping. M.R wrote the first draft of the manuscript and conducted the literature review.

Chapter 7

Conclusions and Future Works

7.1 Conclusions

This research aimed to address the clinical need for a soft instrument with adjustable stiffness during robot-assisted intervention procedures. The clinical requirements were extracted from the literature in Chapter 1 to guide the objectives of this thesis, which were to develop, verify, and validate mechanical technology for real-time, accurate, and robust stiffness adaptation in robot-assisted intervention systems. Also, comprehensive review of the literature in Chapter 1 was conducted to identify different types of actuation mechanisms, materials, and working conditions of soft robots, with the goal of selecting the most suitable approach for stiffness adaptation in the context of robot-assisted surgical interventions. Subsequently, a feasibility study was performed to model a soft robot based on the Cosserat theory with quasi-static assumptions and IVP conditions. In this design, a central channel was considered for air pressure, and the relationship between internal pressure and soft robot stiffness was calculated in Chapter 2. This study confirmed the hypothesis of stiffness adaptation through hybrid actuation. The Cosserat rod model was then updated in Chapter 3 to account for the nonlinearity of the silicon material using the 2MR model, and it was combined with the Cosserat model. Additionally, an identifier was introduced to measure the stiffness of the soft robot based on tip force and tip displacement, as a function of the internal pressure. To further validate the Cosserat rod model for applications requiring stiffness adaptation, Chapter 4 introduced three passages for tendons to validate the Cosserat model in 3D space. The effect of tendon tension on

the local strains of the soft robot was also captured, and the variation of flexural rigidity in response to chamber pressure was successfully validated against experimental results.

In the final improvement of the Cosserat rod model in Chapter 5, a set of dynamic PDEs for the soft robot was derived by considering the 2MR model and BVP conditions. This allowed for a more comprehensive understanding of the dynamic behavior of the soft robot. Finally, in Chapter 6, the focus shifted to the geometry optimization of the soft robot to reduce radial deformation and minimize actuation efforts, making it more suitable for position-stiffness control. In conclusion, this research successfully addressed the clinical need for a soft instrument with adjustable stiffness in robot-assisted intervention procedures. By extracting clinical requirements from the literature, conducting a comprehensive literature review, and performing feasibility studies, this thesis developed, verified, and validated mechanical technology for real-time, accurate, and robust stiffness adaptation in robot-assisted intervention systems. The Cosserat rod model, combined with the 2MR model, proved to be an effective approach for modeling the soft robot, capturing the nonlinearity of the silicon material, and validating the stiffness adaptation through experimental results. The addition of tendons and consideration of dynamic PDEs further expanded the validity and applicability of the Cosserat rod model. Finally, the geometry optimization efforts resulted in a soft robot design that exhibited reduced radial deformation and required less actuation effort, making it well suited for position-stiffness control. Overall, this research has made significant contributions to the field of robot-assisted surgical interventions and opens up new possibilities for improving patient outcomes in clinical settings.

7.2 Future Works

The following features were anticipated to enhance the state-of-the-art of soft surgical robots by introducing a new capability for adaptability during interventions:

(1) Clinical studies have indicated that one of the primary technical limitations that hindered the global adoption of robot-assisted technology was the loss of intraoperative haptic perception for surgeons. The primary mechanism involved in perceiving the insertion force of devices was through exteroception. Previous studies, such as the one conducted by Rafii-Tari et al.

[166], demonstrated that the most significant haptic cue during interventional procedures was the sensation of insertion force experienced by the surgeon during the operation. Consequently, there was a clinical need for a method to measure or estimate the insertion force and provide haptic feedback to the surgeons. This need could be addressed by utilizing an inverse Cosserat rod-based model [105, 58].

(2) Further *in-vivo* testing should be conducted to validate the feasibility of the model in real operation room (OR) environments. This step would provide essential insights into the robot's performance under realistic conditions, enabling a better assessment of its practicality and reliability.

(3) The feasibility of achieving position-stiffness hybrid control by integrating tendon-pneumatic actuation mechanisms needs to be explored. By adopting this approach, the stiffness of specific segments of the robot could be dynamically adjusted based on their position. This adaptability would enable the robot to respond effectively to varying surgical scenarios.

(4) To evaluate the accuracy of the leader-follower performance of the soft robot, a model-based position controller will be developed. This controller will allow for precise control over the robot's movements, enabling investigations into the accuracy of tip-tracking for both simple and tortuous trajectories. Such assessments are crucial for understanding and improving the robot's overall performance.

(5) An extension of this work would involve considering the effect of the ratio of the robot's cross-sectional area to length on the model's accuracy. The flexure slenderness may impact the boundaries, such as pressure and tendon tension, within which the proposed model remains valid. Investigating this aspect would provide valuable insights into the limitations and applicability of the model in different scenarios.

(6) Replacement of FE simulation with a less computationally costly method could facilitate real-time tip positioning. Exploring alternative simulation techniques that are more time-efficient but still provide accurate results would enable faster and more practical implementation of the robot's functionalities.

(7) The effects of incorporating multiple chambers for directional stiffening should be explored. Assessing the benefits and implications of such design modifications would enhance our understanding of the robot's performance and its potential for further optimization.

By addressing these research directions, the field of soft surgical robots can make significant advancements in adaptability, control precision, and overall performance, thereby contributing to improved surgical interventions and patient outcomes.

Bibliography

[1] S Atallah, B Martin-Perez, D Keller, J Burke, and L Hunter. Natural-orifice transluminal endoscopic surgery. *Journal of British Surgery*, 102(2):e73–e92, 2015.

[2] Jessica Burgner-Kahrs, D Caleb Rucker, and Howie Choset. Continuum robots for medical applications: A survey. *IEEE Transactions on Robotics*, 31(6):1261–1280, 2015.

[3] Mark Runciman, Ara Darzi, and George P Mylonas. Soft robotics in minimally invasive surgery. *Soft robotics*, 6(4):423–443, 2019.

[4] Jorge E Quintero, Rui Zhang, Qi Pang, Yi Xing, Peter Hardy, Xiaotong Fan, Yi Ai, Don M Gash, Greg A Gerhardt, Richard Grondin, et al. Surgical methodology and protocols for preventing implanted cerebral catheters from becoming obstructed during and after neurosurgery. *Journal of Neuroscience Methods*, 349:109020, 2021.

[5] Gabriel Liberale, Michel El Houkayem, Claire Viste, Fikri Bouazza, Michel Moreau, Issam El Nakadi, and Isabelle Veys. Evaluation of the perceptions and cosmetic satisfaction of breast cancer patients undergoing totally implantable vascular access device (tivad) placement. *Supportive care in cancer*, 24:5035–5040, 2016.

[6] Yasuhiko Igawa, Jean-Jacques Wyndaele, and Osamu Nishizawa. Catheterization: possible complications and their prevention and treatment. *International journal of urology*, 15(6): 481–485, 2008.

[7] Christine Shan-Chi Chiu, Yuh-Ming Hwu, Robert Kuo-Kuang Lee, and Ming-Huei Lin. Intrauterine adhesion prevention with malecot catheter after hysteroscopic myomectomy: A novel approach. *Taiwanese Journal of Obstetrics and Gynecology*, 59(1):56–60, 2020.

[8] Jonas Lussi, Michael Mattmann, Semih Sevim, Fabian Grigis, Carmela De Marco, Christophe Chautems, Salvador Pané, Josep Puigmartí-Luis, Quentin Boehler, and Bradley J Nelson. A submillimeter continuous variable stiffness catheter for compliance control. *Advanced Science*, 8(18):2101290, 2021.

[9] Amir Hooshiar, Siamak Najarian, and Javad Dargahi. Haptic telerobotic cardiovascular intervention: a review of approaches, methods, and future perspectives. *IEEE reviews in biomedical engineering*, 13:32–50, 2019.

[10] Yong-jie Zhao, Xin-chong Du, Xiao-qiang Deng, Hao Zhang, Hao-ran Zhang, Rui-qi Qiao, Jing-yu Zhang, and Yong-cheng Hu. Resuscitative endovascular balloon occlusion of the aorta for blood control in lumbar spine tumor resection surgery: A technical note. *Orthopaedic Surgery*, 13(5):1540–1545, 2021.

[11] Ru Zhang, Zhenglei Xu, Jun Yao, Ruiyue Shi, Dingguo Zhang, Yi Mei, Yunlian Zhong, Mingguang Lai, and Lisheng Wang. Tuberculous peritonitis diagnosed using laparoscopy with assistance of a central venous catheter. *Experimental and Therapeutic Medicine*, 16(6): 5265–5271, 2018.

[12] Yili Fu, Hao Liu, Wentai Huang, Shuguo Wang, and Zhaoguang Liang. Steerable catheters in minimally invasive vascular surgery. *The International Journal of Medical Robotics and Computer Assisted Surgery*, 5(4):381–391, 2009.

[13] Mohammad Jolaei, Amir Hooshiar, Javad Dargahi, and Muthukumaran Packirisamy. Toward task autonomy in robotic cardiac ablation: Learning-based kinematic control of soft tendon-driven catheters. *Soft Robotics*, 8(3):340–351, 2021.

[14] Amir Hooshiar, Alireza Payami, Javad Dargahi, and Siamak Najarian. Magnetostriction-based force feedback for robot-assisted cardiovascular surgery using smart magnetorheological elastomers. *Mechanical Systems and Signal Processing*, 161:107918, 2021.

[15] Yueh-Hsun Lu, Karthick Mani, Bivas Panigrahi, Saurabh Hajari, and Chia-Yuan Chen. A shape memory alloy-based miniaturized actuator for catheter interventions. *Cardiovascular Engineering and Technology*, 9:405–413, 2018.

[16] David B Camarillo, Christopher F Milne, Christopher R Carlson, Michael R Zinn, and J Kenneth Salisbury. Mechanics modeling of tendon-driven continuum manipulators. *IEEE transactions on robotics*, 24(6):1262–1273, 2008.

[17] Rafael Beyar, Luis Gruberg, Dan Deleanu, Ariel Roguin, Yaron Almagor, Silviu Cohen, Ganesh Kumar, and Tal Wenderow. Remote-control percutaneous coronary interventions: concept, validation, and first-in-humans pilot clinical trial. *Journal of the American College of Cardiology*, 47(2):296–300, 2006.

[18] Monarch platform for endoscopy. URL https://www.jnjmedtech.com/en-US/product-family/monarch.

[19] Medrobotics flex robotic system navigates through complex anatomy. URL https://medrobotics.com/.

[20] Giora Weisz, D Christopher Metzger, Ronald P Caputo, Juan A Delgado, J Jeffrey Marshall, George W Vetrovec, Mark Reisman, Ron Waksman, Juan F Granada, Victor Novack, et al. Safety and feasibility of robotic percutaneous coronary intervention: Precise (percutaneous robotically-enhanced coronary intervention) study. *Journal of the American College of Cardiology*, 61(15):1596–1600, 2013.

[21] Loïc Blanc, Alain Delchambre, and Pierre Lambert. Flexible medical devices: Review of controllable stiffness solutions. In *Actuators*, volume 6, page 23. MDPI, 2017.

[22] Hedyeh Rafii-Tari, Christopher J Payne, and Guang-Zhong Yang. Current and emerging robot-assisted endovascular catheterization technologies: a review. *Annals of biomedical engineering*, 42:697–715, 2014.

[23] Matteo Cianchetti, Cecilia Laschi, Arianna Menciassi, and Paolo Dario. Biomedical applications of soft robotics. *Nature Reviews Materials*, 3(6):143–153, 2018.

[24] Guanjun Bao, Hui Fang, Lingfeng Chen, Yuehua Wan, Fang Xu, Qinghua Yang, and Libin Zhang. Soft robotics: Academic insights and perspectives through bibliometric analysis. *Soft robotics*, 5(3):229–241, 2018.

[25] Matteo Cianchetti, Tommaso Ranzani, Giada Gerboni, Iris De Falco, Cecilia Laschi, and Arianna Menciassi. Stiff-flop surgical manipulator: Mechanical design and experimental characterization of the single module. In *2013 IEEE/RSJ international conference on intelligent robots and systems*, pages 3576–3581. IEEE, 2013.

[26] Cecilia Laschi and Matteo Cianchetti. Soft robotics: new perspectives for robot bodyware and control. *Frontiers in bioengineering and biotechnology*, 2:3, 2014.

[27] Huu Minh Le, Thanh Nho Do, and Soo Jay Phee. A survey on actuators-driven surgical robots. *Sensors and Actuators A: Physical*, 247:323–354, 2016.

[28] M Lazeroms, A La Haye, W Sjoerdsma, W Schreurs, W Jongkind, G Honderd, and C Grimbergen. A hydraulic forceps with force-feedback for use in minimally invasive surgery. *Mechatronics*, 6(4):437–446, 1996.

[29] Satoshi Konishi, Taizou Kobayashi, Hidehiro Maeda, Shuzo Asajima, and Masaaki Makikawa. Cuff actuator for adaptive holding condition around nerves. *Sensors and Actuators B: Chemical*, 83(1-3):60–66, 2002.

[30] Koji Ikuta, Hironobu Ichikawa, and Katsuya Suzuki. Safety-active catheter with multiple-segments driven by micro-hydraulic actuators. In *Medical Image Computing and Computer-Assisted Intervention—MICCAI 2002: 5th International Conference Tokyo, Japan, September 25–28, 2002 Proceedings, Part I 5*, pages 182–191. Springer, 2002.

[31] Koji Ikuta, Hironobu Ichikawa, Katsuya Suzuki, and Daisuke Yajima. Multi-degree of freedom hydraulic pressure driven safety active catheter. In *Proceedings 2006 IEEE International Conference on Robotics and Automation, 2006. ICRA 2006.*, pages 4161–4166. IEEE, 2006.

[32] Koji Ikuta, Hironobu Ichikawa, Katuya Suzuki, and Takahiro Yamamoto. Safety active catheter with multi-segments driven by innovative hydro-pressure micro actuators. In *The Sixteenth Annual International Conference on Micro Electro Mechanical Systems, 2003. MEMS-03 Kyoto. IEEE*, pages 130–135. IEEE, 2003.

[33] Masashi Ikeuchi and Koji Ikuta. Membrane micro emboss following excimer laser ablation (meme-x) process for pressure-driven micro active catheter. In *2008 IEEE 21st International Conference on Micro Electro Mechanical Systems*, pages 62–65. IEEE, 2008.

[34] Marcello Calisti, Giacomo Picardi, and Cecilia Laschi. Fundamentals of soft robot locomotion. *Journal of The Royal Society Interface*, 14(130):20170101, 2017.

[35] Julius E Bernth, Alberto Arezzo, and Hongbin Liu. A novel robotic meshworm with segment-bending anchoring for colonoscopy. *IEEE Robotics and Automation Letters*, 2(3):1718–1724, 2017.

[36] Hye-Jong Kim, Akihiro Kawamura, Yasutaka Nishioka, and Sadao Kawamura. Mechanical design and control of inflatable robotic arms for high positioning accuracy. *Advanced Robotics*, 32(2):89–104, 2018.

[37] Claudio Pacchierotti, Federico Ongaro, Frank Van den Brink, ChangKyu Yoon, Domenico Prattichizzo, David H Gracias, and Sarthak Misra. Steering and control of miniaturized untethered soft magnetic grippers with haptic assistance. *IEEE transactions on automation science and engineering*, 15(1):290–306, 2017.

[38] Sheila Russo, Tommaso Ranzani, J Gafford, Conor J Walsh, and Robert J Wood. Soft pop-up mechanisms for micro surgical tools: Design and characterization of compliant millimeter-scale articulated structures. In *2016 IEEE International Conference on Robotics and Automation (ICRA)*, pages 750–757. IEEE, 2016.

[39] Carmel Majidi. Soft robotics: a perspective—current trends and prospects for the future. *Soft robotics*, 1(1):5–11, 2014.

[40] Panagiotis Polygerinos, Nikolaus Correll, Stephen A Morin, Bobak Mosadegh, Cagdas D Onal, Kirstin Petersen, Matteo Cianchetti, Michael T Tolley, and Robert F Shepherd. Soft robotics: Review of fluid-driven intrinsically soft devices; manufacturing, sensing, control, and applications in human-robot interaction. *Advanced Engineering Materials*, 19(12): 1700016, 2017.

[41] Xu Dong Wang, Heng Wei Chen, Liao Wang, Wen Zhou, and Yi Qing Li. Design and analysis of pneumatic bending actuator used in soft robotics. In *Advances in Science and Technology*, volume 105, pages 194–201. Trans Tech Publ, 2021.

[42] Lukas Lindenroth, Christian Duriez, Junghwan Back, Kawal Rhode, and Hongbin Liu. Intrinsic force sensing capabilities in compliant robots comprising hydraulic actuation. In *2017 IEEE/RSJ International Conference on Intelligent Robots and Systems (IROS)*, pages 2923–2928. IEEE, 2017.

[43] Hesheng Wang, Runxi Zhang, Weidong Chen, Xiaozhou Wang, and Rolf Pfeifer. A cable-driven soft robot surgical system for cardiothoracic endoscopic surgery: preclinical tests in animals. *Surgical endoscopy*, 31:3152–3158, 2017.

[44] Yoseph Bar-Cohen. Eap as artificial muscles: progress and challenges. *Smart Structures and Materials 2004: Electroactive Polymer Actuators and Devices (EAPAD)*, 5385:10–16, 2004.

[45] Junsun Hwang, Jin-young Kim, and Hongsoo Choi. A review of magnetic actuation systems and magnetically actuated guidewire-and catheter-based microrobots for vascular interventions. *Intelligent Service Robotics*, 13:1–14, 2020.

[46] Benjamin Gorissen, Wannes Vincentie, Farid Al-Bender, Dominiek Reynaerts, and Michaël De Volder. Modeling and bonding-free fabrication of flexible fluidic microactuators with a bending motion. *Journal of Micromechanics and Microengineering*, 23(4):045012, 2013.

[47] Yahya Elsayed, Augusto Vincensi, Constantina Lekakou, Tao Geng, CM Saaj, Tommaso Ranzani, Matteo Cianchetti, and Arianna Menciassi. Finite element analysis and design optimization of a pneumatically actuating silicone module for robotic surgery applications. *Soft Robotics*, 1(4):255–262, 2014.

[48] Minou Kouh Soltani, Sohrab Khanmohammadi, Farzan Ghalichi, and Farrokh Janabi-Sharifi. A soft robotics nonlinear hybrid position/force control for tendon driven catheters. *International Journal of Control, Automation and Systems*, 15:54–63, 2017.

[49] Jae-Eul Shim, Ying-Jun Quan, Wei Wang, Hugo Rodrigue, Sung-Hyuk Song, and Sung-Hoon Ahn. A smart soft actuator using a single shape memory alloy for twisting actuation. *Smart Materials and Structures*, 24(12):125033, 2015.

[50] Agostino Stilli, Helge A Wurdemann, and Kaspar Althoefer. Shrinkable, stiffness-controllable soft manipulator based on a bio-inspired antagonistic actuation principle. In *2014 IEEE/RSJ International Conference on Intelligent Robots and Systems*, pages 2476–2481. IEEE, 2014.

[51] Yoel Shapiro, Alon Wolf, and Kosa Gabor. Bi-bellows: Pneumatic bending actuator. *Sensors and Actuators A: Physical*, 167(2):484–494, 2011.

[52] Kristin M de Payrebrune and Oliver M O'Reilly. On constitutive relations for a rod-based model of a pneu-net bending actuator. *Extreme Mechanics Letters*, 8:38–46, 2016.

[53] Robert J Webster III and Bryan A Jones. Design and kinematic modeling of constant curvature continuum robots: A review. *The International Journal of Robotics Research*, 29(13): 1661–1683, 2010.

[54] Maria Neumann and Jessica Burgner-Kahrs. Considerations for follow-the-leader motion of extensible tendon-driven continuum robots. In *2016 IEEE international conference on robotics and automation (ICRA)*, pages 917–923. IEEE, 2016.

[55] Srinivas Neppalli and Bryan A Jones. Design, construction, and analysis of a continuum robot. In *2007 IEEE/RSJ International Conference on Intelligent Robots and Systems*, pages 1503–1507. IEEE, 2007.

[56] Stuart S Antman. Problems in nonlinear elasticity. *Nonlinear Problems of Elasticity*, pages 513–584, 2005.

[57] Bryan A Jones, Ricky L Gray, and Krishna Turlapati. Three dimensional statics for continuum robotics. In *2009 IEEE/RSJ International Conference on Intelligent Robots and Systems*, pages 2659–2664. IEEE, 2009.

[58] Amir Hooshiar, Amir Sayadi, Mohammad Jolaei, and Javad Dargahi. Accurate estimation of tip force on tendon-driven catheters using inverse cosserat rod model. In *2020 International Conference on Biomedical Innovations and Applications (BIA)*, pages 37–40. IEEE, 2020.

[59] Deepak Trivedi, Amir Lotfi, and Christopher D Rahn. Geometrically exact models for soft robotic manipulators. *IEEE Transactions on Robotics*, 24(4):773–780, 2008.

[60] Yi Sun, Shuang Song, Xinquan Liang, and Hongliang Ren. A miniature soft robotic manipulator based on novel fabrication methods. *IEEE Robotics and Automation Letters*, 1(2): 617–623, 2016.

[61] Hirozumi Takeshima and Toshio Takayama. Geometric estimation of the deformation and the design method for developing helical bundled-tube locomotive devices. *IEEE/ASME Transactions on Mechatronics*, 23(1):223–232, 2017.

[62] Ning Tan, Xiaoyi Gu, and Hongliang Ren. Design, characterization and applications of a novel soft actuator driven by flexible shafts. *Mechanism and Machine Theory*, 122:197–218, 2018.

[63] Sean A Bailey, Jorge G Cham, Mark R Cutkosky, and Robert J Full. Biomimetic robotic mechanisms via shape deposition manufacturing. In *Robotics Research: the Ninth International Symposium*, pages 403–410. Springer, 2000.

[64] Yoko Muramatsu, Taizo Kobayashi, and Satoshi Konishi. Flexible end-effector integrated with scanning actuator and optical waveguide for endoscopic fluorescence imaging diagnosis. In *2015 28th IEEE International Conference on Micro Electro Mechanical Systems (MEMS)*, pages 166–167. IEEE, 2015.

[65] Koji Ikuta, Yoshikatsu Matsuda, Daisuke Yajima, and Yusuke Ota. Pressure pulse drive: A control method for the precise bending of hydraulic active catheters. *IEEE/ASME Transactions on Mechatronics*, 17(5):876–883, 2011.

[66] Xinquan Liang, Yi Sun, and Hongliang Ren. A flexible fabrication approach toward the shape

engineering of microscale soft pneumatic actuators. *IEEE Robotics and Automation Letters*, 2(1):165–170, 2016.

[67] Matteo Cianchetti, Tommaso Ranzani, Giada Gerboni, Thrishantha Nanayakkara, Kaspar Althoefer, Prokar Dasgupta, and Arianna Menciassi. Soft robotics technologies to address shortcomings in today's minimally invasive surgery: the stiff-flop approach. *Soft robotics*, 1 (2):122–131, 2014.

[68] Majid Roshanfar, Salar Taki, Amir Sayadi, Renzo Cecere, Javad Dargahi, and Amir Hooshiar. Hyperelastic modeling and validation of hybrid-actuated soft robot with pressure-stiffening. *Micromachines*, 14(5):900, 2023.

[69] Majid Roshanfar, Amir Sayadi, Javad Dargahi, and Amir Hooshiar. Stiffness adaptation of a hybrid soft surgical robot for improved safety in interventional surgery. In *2022 44th Annual International Conference of the IEEE Engineering in Medicine & Biology Society (EMBC)*, pages 4853–4859. IEEE, 2022.

[70] Majid Roshanfar, Javad Dargahi, and Amir Hooshiar. Toward semi-autonomous stiffness adaptation of pneumatic soft robots: Modeling and validation. In *2021 IEEE International Conference on Autonomous Systems (ICAS)*, pages 1–5. IEEE, 2021.

[71] Majid Roshanfar, Naghmeh Bandari, Amir Hooshiar, and Javad Dargahi. Addressing the covid-19 healthcare needs by teleoperated robot-assisted intervention. In *ICRA 2021 Workshop, Impact of COVID-19 on Medical Robotics and Wearables Research: Learning from the Past and Strategizing for the Future*, 2021.

[72] Majid Roshanfar, Pedram Fekri, and Javad Dargahi. A deep learning model for tip force estimation on steerable catheters via learning-from-simulation. Technical report, Hamlyn Symposium on Medical Robotics, 2023.

[73] Seyedfarzad Famouri, Pedram Fekri, Majid Roshanfar, and Javad Dargahi. Towards surgical skill modeling in cardiac ablation using deep learning. In *2023 27th International Conference on Methods and Models in Automation and Robotics (MMAR)*, pages 216–221. IEEE, 2023.

[74] Majid Roshanfar, Pedram Fekri, and Javad Dargahi. Toward autonomous cardiac catheterization through a parametric finite element simulation with experimental validation. *ICAS 2023*, page 23, 2023.

[75] Tannaz Torkaman, Majid Roshanfar, Javad Dargahi, and Amir Hooshiar. Embedded six-dof force-torque sensor for soft robots with learning-based calibration. *IEEE Sensors Journal*, 2023.

[76] Mohammad Haghayeghjahromi, Majid Roshanfar, and Javad Dargahi. Analysis of self-expanded and balloon-expanded coronary stents using finite element method. *International Journal of Mechanical and Production Engineering (IJMPE)*, 10(8):8–11, August 2022.

[77] Tannaz Torkaman, Majid Roshanfar, Javad Dargahi, and Amir Hooshiar. Accurate embedded force sensor for soft robots with rate-dependent deep neural calibration. In *2022 IEEE International Symposium on Robotic and Sensors Environments (ROSE)*, pages 1–7. IEEE, 2022.

[78] Mehrshad Alizadeh, Mohammad Choulaei, Majid Roshanfar, and Javad Dargahi. Vibrational characteristic of heart stent using finite element model. *International journal of health sciences*, 6(S4):4095–4106, Jun. 2022.

[79] Tannaz Torkaman, Majid Roshanfar, Javad Dargahi, and Amir Hooshiar. Analytical modeling and experimental validation of a gelatin-based shape sensor for soft robots. In *2022 International Symposium on Medical Robotics (ISMR)*, pages 1–7. IEEE, 2022.

[80] Mohammad Jolaei, Amir Hooshiar, Amir Sayadi, Javad Dargahi, and Muthukumaran Packirisamy. Sensor-free force control of tendon-driven ablation catheters through position control and contact modeling. In *2020 42nd Annual International Conference of the IEEE Engineering in Medicine & Biology Society (EMBC)*, pages 5248–5251. IEEE, 2020.

[81] Erina Baynojir Joyee and Yayue Pan. Additive manufacturing of multi-material soft robot for on-demand drug delivery applications. *Journal of Manufacturing Processes*, 56:1178–1184, 2020.

[82] Olatunji Mumini Omisore, Shipeng Han, Jing Xiong, Hui Li, Zheng Li, and Lei Wang. A review on flexible robotic systems for minimally invasive surgery. *IEEE Transactions on Systems, Man, and Cybernetics: Systems*, 52(1):631–644, 2020.

[83] Mahta Khoshnam, Allan C Skanes, and Rajni V Patel. Modeling and estimation of tip contact force for steerable ablation catheters. *IEEE Transactions on Biomedical Engineering*, 62(5): 1404–1415, 2015.

[84] Vincent A Aloi and D Caleb Rucker. Estimating loads along elastic rods. In *2019 International Conference on Robotics and Automation (ICRA)*, pages 2867–2873. IEEE, 2019.

[85] Shahir Hasanzadeh and Farrokh Janabi-Sharifi. Model-based force estimation for intracardiac catheters. *IEEE/ASME Transactions on Mechatronics*, 21(1):154–162, 2015.

[86] Robert K Katzschmann, Cosimo Della Santina, Yasunori Toshimitsu, Antonio Bicchi, and Daniela Rus. Dynamic motion control of multi-segment soft robots using piecewise constant curvature matched with an augmented rigid body model. In *2019 2nd IEEE International Conference on Soft Robotics (RoboSoft)*, pages 454–461. IEEE, 2019.

[87] John Till, Vincent Aloi, and Caleb Rucker. Real-time dynamics of soft and continuum robots based on cosserat rod models. *The International Journal of Robotics Research*, 38(6):723–746, 2019.

[88] Richard M Murray, Zexiang Li, S Shankar Sastry, and S Shankara Sastry. *A mathematical introduction to robotic manipulation*. CRC press, 1994.

[89] Gina Olson, Ross L Hatton, Julie A Adams, and Yiğit Mengüç. An euler–bernoulli beam model for soft robot arms bent through self-stress and external loads. *International Journal of Solids and Structures*, 207:113–131, 2020.

[90] Luc Marechal, Pascale Balland, Lukas Lindenroth, Fotis Petrou, Christos Kontovounisios, and Fernando Bello. Toward a common framework and database of materials for soft robotics. *Soft robotics*, 8(3):284–297, 2021.

[91] ASTM Standard. D412, standard test methods for vulcanized rubber and thermoplastic elastomers–tension. *ASTM International, West Conshohoken, PA, USA*, 2006.

[92] HD Hoeg, A Brett Slatkin, Joel W Burdick, and Warren S Grundfest. Biomechanical modeling of the small intestine as required for the design and operation of a robotic endoscope. In *Proceedings 2000 ICRA. Millennium Conference. IEEE International Conference on Robotics and Automation. Symposia Proceedings (Cat. No. 00CH37065)*, volume 2, pages 1599–1606. IEEE, 2000.

[93] Wen Tang, Pierre Lagadec, Derek Gould, Tao Ruan Wan, Jianhua Zhai, and Thien How. A realistic elastic rod model for real-time simulation of minimally invasive vascular interventions. *The Visual Computer*, 26:1157–1165, 2010.

[94] Farrokh Janabi-Sharifi, Amir Jalali, and Ian D Walker. Cosserat rod-based dynamic modeling of tendon-driven continuum robots: A tutorial. *IEEE Access*, 9:68703–68719, 2021.

[95] Matheus S Xavier, Charbel D Tawk, Ali Zolfagharian, Joshua Pinskier, David Howard, Taylor Young, Jiewen Lai, Simon M Harrison, Yuen K Yong, Mahdi Bodaghi, et al. Soft pneumatic actuators: A review of design, fabrication, modeling, sensing, control and applications. *IEEE Access*, 2022.

[96] Pierre E Dupont, Nabil Simaan, Howie Choset, and Caleb Rucker. Continuum robots for medical interventions. *Proceedings of the IEEE*, 110(7):847–870, 2022.

[97] Amie J Kent, Kim A Byrnes, and Stephanie H Chang. State of the art: robotic bronchoscopy. In *Seminars in Thoracic and Cardiovascular Surgery*, volume 32, pages 1030–1035. Elsevier, 2020.

[98] Jongwoo Kim, Thomas Looi, Allen Newman, and James Drake. Development of deployable bending wrist for minimally invasive laparoscopic endoscope. In *2020 IEEE/RSJ International Conference on Intelligent Robots and Systems (IROS)*, pages 3048–3054. IEEE, 2020.

[99] Meng Li, Aniket Pal, Amirreza Aghakhani, Abdon Pena-Francesch, and Metin Sitti. Soft actuators for real-world applications. *Nature Reviews Materials*, 7(3):235–249, 2022.

[100] Kaspar Althoefer. Antagonistic actuation and stiffness control in soft inflatable robots. *Nature Reviews Materials*, 3(6):76–77, 2018.

[101] Ahmad Ataka, Taqi Abrar, Fabrizio Putzu, Hareesh Godaba, and Kaspar Althoefer. Model-based pose control of inflatable eversion robot with variable stiffness. *IEEE Robotics and Automation Letters*, 5(2):3398–3405, 2020.

[102] Ali Zolfagharian, MA Parvez Mahmud, Saleh Gharaie, Mahdi Bodaghi, Abbas Z Kouzani, and Akif Kaynak. 3d/4d-printed bending-type soft pneumatic actuators: Fabrication, modelling, and control. *Virtual and Physical Prototyping*, 15(4):373–402, 2020.

[103] Priyanka Rao, Quentin Peyron, Sven Lilge, and Jessica Burgner-Kahrs. How to model tendon-driven continuum robots and benchmark modelling performance. *Frontiers in Robotics and AI*, 7:630245, 2021.

[104] G Runge, M Wiese, L Günther, and A Raatz. A framework for the kinematic modeling of soft material robots combining finite element analysis and piecewise constant curvature kinematics. In *2017 3rd International Conference on Control, Automation and Robotics (ICCAR)*, pages 7–14. IEEE, 2017.

[105] Amir Hooshiar, Amir Sayadi, Mohammad Jolaei, and Javad Dargahi. Analytical tip force estimation on tendon-driven catheters through inverse solution of cosserat rod model. In *2021 IEEE/RSJ International Conference on Intelligent Robots and Systems (IROS)*, pages 1829–1834. IEEE, 2021.

[106] Matteo Russo, Seyed Mohammad Hadi Sadati, Xin Dong, Abdelkhalick Mohammad, Ian D Walker, Christos Bergeles, Kai Xu, and Dragos A Axinte. Continuum robots: An overview. *Advanced Intelligent Systems*, 5(5):2200367, 2023.

[107] Hunter B Gilbert. On the mathematical modeling of slender biomedical continuum robots. *Frontiers in Robotics and AI*, 8:732643, 2021.

[108] Xiaocheng Wang, Changliang Wang, Xueqian Wang, Deshan Meng, Bin Liang, and Hejie Xu. Dynamics modeling and verification of parallel extensible soft robot based on cosserat

rod theory. In *2022 IEEE 18th International Conference on Automation Science and Engineering (CASE)*, pages 1933–1939. IEEE, 2022.

[109] Weiqiang Dou, Guoliang Zhong, Jie Yang, and Jiawei Shen. Design and modeling of a hybrid soft robotic manipulator with compliant mechanism. *IEEE Robotics and Automation Letters*, 8(4):2301–2308, 2023.

[110] Xinjia Huang, Jiang Zou, and Guoying Gu. Kinematic modeling and control of variable curvature soft continuum robots. *IEEE/ASME Transactions on Mechatronics*, 26(6):3175–3185, 2021.

[111] Lizhou Niu, Liang Ding, Haibo Gao, Yang Su, Zongquan Deng, and Zhen Liu. Closed-form equations and experimental verification for soft robot arm based on cosserat theory. In *2019 IEEE/RSJ International Conference on Intelligent Robots and Systems (IROS)*, pages 6630–6635. IEEE, 2019.

[112] Seyede Fatemeh Ghoreishi, Ryan D Sochol, Dheeraj Gandhi, Axel Krieger, and Mark Fuge. Physics-informed modeling and control of multi-actuator soft catheter robots. *Frontiers in Robotics and AI*, 8:772628, 2022.

[113] Haihong Li, Lingxiao Xun, and Gang Zheng. Piecewise linear strain cosserat model for soft slender manipulator. *IEEE Transactions on Robotics*, 2023.

[114] Brandon J Caasenbrood, Alexander Y Pogromsky, and Henk Nijmeijer. Dynamic modeling of hyper-elastic soft robots using spatial curves. *IFAC-PapersOnLine*, 53(2):9238–9243, 2020.

[115] D Caleb Rucker and Robert J Webster III. Statics and dynamics of continuum robots with general tendon routing and external loading. *IEEE Transactions on Robotics*, 27(6):1033–1044, 2011.

[116] Phuc DH Bui and Joshua A Schultz. States and contact forces estimation for a fabric-reinforced inflatable soft robot. In *2021 IEEE International Conference on Robotics and Automation (ICRA)*, pages 11820–11826. IEEE, 2021.

[117] Philip J Podrid and Robert J Myerburg. Epidemiology and stratification of risk for sudden cardiac death. *Clinical Cardiology: An International Indexed and Peer-Reviewed Journal for Advances in the Treatment of Cardiovascular Disease*, 28(S1):3–11, 2005.

[118] Carla Cofiño-Fabres, Robert Passier, and Verena Schwach. Towards improved human in vitro models for cardiac arrhythmia: Disease mechanisms, treatment, and models of atrial fibrillation. *Biomedicines*, 11(9):2355, 2023.

[119] Prakash C Deedwania and Joel A Lardizabal. Atrial fibrillation in heart failure: a comprehensive review. *The American journal of medicine*, 123(3):198–204, 2010.

[120] Aakriti Gupta, Tharani Perera, Anand Ganesan, Thomas Sullivan, Dennis H Lau, Kurt C Roberts-Thomson, Anthony G Brooks, and Prashanthan Sanders. Complications of catheter ablation of atrial fibrillation: a systematic review. *Circulation: Arrhythmia and Electrophysiology*, 6(6):1082–1088, 2013.

[121] ROY Beinart, Suhny Abbara, Andrew Blum, Maros Ferencik, Kevin Heist, Jeremy Ruskin, and Moussa Mansour. Left atrial wall thickness variability measured by ct scans in patients undergoing pulmonary vein isolation. *Journal of cardiovascular electrophysiology*, 22(11): 1232–1236, 2011.

[122] Wenke Duan, Toluwanimi Akinyemi, Wenjing Du, Jun Ma, Xingyu Chen, Fuhao Wang, Olatunji Omisore, Jingjing Luo, Hongbo Wang, and Lei Wang. Technical and clinical progress on robot-assisted endovascular interventions: A review. *Micromachines*, 14(1):197, 2023.

[123] Chi Cong Nguyen, Mai Thanh Thai, Trung Thien Hoang, James Davies, Phuoc Thien Phan, Kefan Zhu, Liao Wu, Matthew A Brodie, David Tsai, Quang Phuc Ha, et al. Development of a soft robotic catheter for vascular intervention surgery. *Sensors and Actuators A: Physical*, 357:114380, 2023.

[124] Mai Thanh Thai, Phuoc Thien Phan, Trung Thien Hoang, Shing Wong, Nigel H Lovell, and Thanh Nho Do. Advanced intelligent systems for surgical robotics. *Advanced Intelligent Systems*, 2(8):1900138, 2020.

[125] Yasuo Okumura, Susan B Johnson, T Jared Bunch, Benhur D Henz, CHRISTINE J O'BRIEN, and Douglas L Packer. A systematical analysis of in vivo contact forces on virtual catheter tip/tissue surface contact during cardiac mapping and intervention. *Journal of cardiovascular electrophysiology*, 19(6):632–640, 2008.

[126] Bobak Mosadegh, Panagiotis Polygerinos, Christoph Keplinger, Sophia Wennstedt, Robert F Shepherd, Unmukt Gupta, Jongmin Shim, Katia Bertoldi, Conor J Walsh, and George M Whitesides. Pneumatic networks for soft robotics that actuate rapidly. *Advanced functional materials*, 24(15):2163–2170, 2014.

[127] Yang Yu and Tao Fu. Design and experimental study of cavity structure of pneumatic soft actuator. In *Actuators*, volume 12, page 314. MDPI, 2023.

[128] John Till and D Caleb Rucker. Elastic stability of cosserat rods and parallel continuum robots. *IEEE Transactions on Robotics*, 33(3):718–733, 2017.

[129] Richard M Murray, Zexiang Li, and S Shankar Sastry. *A mathematical introduction to robotic manipulation*. CRC press, 2017.

[130] Joachim Linn, Holger Lang, and Andrey Tuganov. Geometrically exact cosserat rods with kelvin–voigt type viscous damping. *Mechanical Sciences*, 4(1):79–96, 2013.

[131] Elisabete Alberdi Celaya and Juan José Anza. Bdf-α: A multistep method with numerical damping control. *System*, 500:9, 2013.

[132] Carmel Majidi. Soft-matter engineering for soft robotics. *Advanced Materials Technologies*, 4(2):1800477, 2019.

[133] Ka-Wai Kwok, Helge Wurdemann, Alberto Arezzo, Arianna Menciassi, and Kaspar Althoefer. Soft robot-assisted minimally invasive surgery and interventions: Advances and outlook. *Proceedings of the IEEE*, 2022.

[134] Daniela Rus and Michael T Tolley. Design, fabrication and control of soft robots. *Nature*, 521(7553):467–475, 2015.

[135] Changyan He, Robert H Nguyen, Cameron Forbrigger, James Drake, Thomas Looi, and Eric Diller. A hybrid steerable robot with magnetic wrist for minimally invasive epilepsy surgery. In *2023 IEEE International Conference on Robotics and Automation (ICRA)*, pages 6830–6836. IEEE, 2023.

[136] Allison M Okamura. Haptics in robot-assisted minimally invasive surgery. *The Encyclopedia of MEDICAL ROBOTICS: Volume 1 Minimally Invasive Surgical Robotics*, pages 317–339, 2019.

[137] Abdellatif Ait Lahcen, Alexandre Caprio, Weihow Hsue, Cory Tschabrunn, Christopher Liu, Bobak Mosadegh, and Simon Dunham. Creating stretchable electronics from dual layer flex-pcb for soft robotic cardiac mapping catheters. *Micromachines*, 14(4):884, 2023.

[138] Varun Kashyap, Alexandre Caprio, Tejas Doshi, Sun-Joo Jang, Christopher F Liu, Bobak Mosadegh, and Simon Dunham. Multilayer fabrication of durable catheter-deployable soft robotic sensor arrays for efficient left atrial mapping. *Science advances*, 6(46):eabc6800, 2020.

[139] Nitish Kumar, Jackson Wirekoh, Samir Saba, Cameron N Riviere, and Yong-Lae Park. Soft miniaturized actuation and sensing units for dynamic force control of cardiac ablation catheters. *Soft robotics*, 8(1):59–70, 2021.

[140] Panagiotis Polygerinos, Stacey Lyne, Zheng Wang, Luis Fernando Nicolini, Bobak Mosadegh, George M Whitesides, and Conor J Walsh. Towards a soft pneumatic glove for hand rehabilitation. In *2013 IEEE/RSJ International Conference on Intelligent Robots and Systems*, pages 1512–1517. IEEE, 2013.

[141] Oncay Yasa, Yasunori Toshimitsu, Mike Y Michelis, Lewis S Jones, Miriam Filippi, Thomas Buchner, and Robert K Katzschmann. An overview of soft robotics. *Annual Review of Control, Robotics, and Autonomous Systems*, 6, 2022.

[142] Nicholas W Bartlett, Michael T Tolley, Johannes TB Overvelde, James C Weaver, Bobak Mosadegh, Katia Bertoldi, George M Whitesides, and Robert J Wood. A 3d-printed, functionally graded soft robot powered by combustion. *Science*, 349(6244):161–165, 2015.

[143] Anoop Rajappan, Barclay Jumet, and Daniel J Preston. Pneumatic soft robots take a step toward autonomy. *Science Robotics*, 6(51):eabg6994, 2021.

[144] Xiaoqian Chen, Xiang Zhang, Yiyong Huang, Lu Cao, and Jinguo Liu. A review of soft manipulator research, applications, and opportunities. *Journal of Field Robotics*, 39(3):281–311, 2022.

[145] Wenkai Huang, Junlong Xiao, and Zhipeng Xu. A variable structure pneumatic soft robot. *Scientific Reports*, 10(1):18778, 2020.

[146] Zhiguang Xing, Junming Zhang, David McCoul, Yanzhen Cui, Lining Sun, and Jianwen Zhao. A super-lightweight and soft manipulator driven by dielectric elastomers. *Soft robotics*, 7(4):512–520, 2020.

[147] Wei Wang, Chak Yuk Yu, Pablo Antonio Abrego Serrano, and Sung-Hoon Ahn. Shape memory alloy-based soft finger with changeable bending length using targeted variable stiffness. *Soft robotics*, 7(3):283–291, 2020.

[148] Tianqi Xu, Jiachen Zhang, Mohammad Salehizadeh, Onaizah Onaizah, and Eric Diller. Millimeter-scale flexible robots with programmable three-dimensional magnetization and motions. *Science Robotics*, 4(29):eaav4494, 2019.

[149] Rongjie Kang, Yong Guo, Lisha Chen, David T Branson, and Jian S Dai. Design of a pneumatic muscle based continuum robot with embedded tendons. *IEEE/ASME Transactions on Mechatronics*, 22(2):751–761, 2016.

[150] Yichao Tang, Yinding Chi, Jiefeng Sun, Tzu-Hao Huang, Omid H Maghsoudi, Andrew Spence, Jianguo Zhao, Hao Su, and Jie Yin. Leveraging elastic instabilities for amplified performance: Spine-inspired high-speed and high-force soft robots. *Science advances*, 6 (19):eaaz6912, 2020.

[151] Zaryab Shahid, Abigail Leah Glatman, and Seok Chang Ryu. Design of a soft composite finger with adjustable joint stiffness. *Soft Robotics*, 6(6):722–732, 2019.

[152] Francesco Stella and Josie Hughes. The science of soft robot design: A review of motivations, methods and enabling technologies. *Frontiers in Robotics and AI*, 9:1059026, 2023.

[153] Xiaohua Hu, Ang Chen, Yigang Luo, Chris Zhang, and Edwin Zhang. Steerable catheters for minimally invasive surgery: a review and future directions. *Computer Assisted Surgery*, 23(1):21–41, 2018.

[154] Yahya Elsayed, Constantina Lekakou, Tommaso Ranzani, Matteo Cianchetti, Mario Morino, Alberto Arezzo, Arianna Menciassi, Tao Geng, and Chakravarthini M Saaj. Crimped braided sleeves for soft, actuating arm in robotic abdominal surgery. *Minimally Invasive Therapy & Allied Technologies*, 24(4):204–210, 2015.

[155] Max McCandless, Alexander Perry, Nicholas DiFilippo, Ashlyn Carroll, Ehab Billatos, and Sheila Russo. A soft robot for peripheral lung cancer diagnosis and therapy. *Soft Robotics*, 2021.

[156] Jue Wang and Alex Chortos. Control strategies for soft robot systems. *Advanced Intelligent Systems*, page 2100165, 2022.

[157] Amir Sayadi. *Modeling and Force Estimation of Cardiac Catheters for Haptics-enabled Tele-intervention*. PhD thesis, Concordia University, 2021.

[158] Feifei Chen and Michael Yu Wang. Design optimization of soft robots: A review of the state of the art. *IEEE Robotics & Automation Magazine*, 27(4):27–43, 2020.

[159] Jelizaveta Konstantinova, Helge Wurdemann, and Ali Shafti. *Soft and Stiffness-controllable Robotics Solutions for Minimally Invasive Surgery: The STIFF-FLOP Approach*. CRC Press, 2022.

[160] Quanquan Liu, Yo Kobayashi, Bo Zhang, Takehiko Noguchi, Yu Takahashi, Yuya Nishio, Yang Cao, Satoshi Ieiri, Kazutaka Toyoda, Munenori Uemura, et al. Development of a smart surgical robot with bended forceps for infant congenital esophageal atresia surgery. In *2014 IEEE International Conference on Robotics and Automation (ICRA)*, pages 2430–2435. IEEE, 2014.

[161] Jiaqi Zhu, Liangxiong Lyu, Yi Xu, Huageng Liang, Xiaoping Zhang, Han Ding, and Zhigang Wu. Intelligent soft surgical robots for next-generation minimally invasive surgery. *Advanced Intelligent Systems*, 3(5):2100011, 2021.

[162] Matheus S Xavier, Andrew J Fleming, and Yuen K Yong. Design and control of pneumatic systems for soft robotics: a simulation approach. *IEEE Robotics and Automation Letters*, 6 (3):5800–5807, 2021.

[163] F Peeters and M Küssner. Materials and its practical application in the industrial design process. *Constitutive models for rubber*, 1:29, 1999.

[164] W Michael Lai, David H Rubin, David Rubin, and Erhard Krempl. *Introduction to continuum mechanics*. Butterworth-Heinemann, 2009.

[165] International Organization for Standardization. *ISO 7743: 2011: Rubber, Vulcanized Or Thermoplastic. Determination of Compression Stress-strain Properties*. ISO, 2011.

[166] Hedyeh Rafii-Tari, Christopher J Payne, Colin Bicknell, Ka-Wai Kwok, Nicholas JW Cheshire, Celia Riga, and Guang-Zhong Yang. Objective assessment of endovascular navigation skills with force sensing. *Annals of biomedical engineering*, 45:1315–1327, 2017.